

ELECTRODE STRUCTURES OF POLYMER-ELECTROLYTE FUEL CELLS (PEFC)

*An electron microscopy approach to the characterization of the
electrode structure of polymer electrolyte fuel cells*

Vom Fachbereich für Material- & Geowissenschaften
der Technischen Universität Darmstadt genehmigte

DISSERTATION

Zur Erlangung des akademischen Grades
Doktor der Ingenieurwissenschaften

von

Dipl. Ing. Frieder Scheiba
aus Mainz

Darmstadt 2009

D 17

Berichterstatter	Prof. Dr. Hartmut Fueß
Mitberichterstatter	Prof. Dr. Wolfram Jaegermann
Tag der Einreichung	24.11.2008
Tag der mündlichen Prüfung	28.01.2009

*Auf keine Weise also können diese irgend etwas anderes
für das Wahre halten als die Schatten jener Kunstwerke?*

- Ganz unmöglich. -

Platon, POLITEIA

ACKNOWLEDGEMENTS

The present thesis has been prepared under the direction of Prof. Dr.-Ing. Dr. h.c. Hartmut Fueß in the Department of Structural Research at the Institute of Materials Science of the Technical University of Darmstadt. I would like to take this opportunity to thank him for providing me the possibility to carry out this thesis in his group and all the support I received during this time.

I would also like to express my thanks to Dr. Christina Roth for her support of this work as well as the pleasant and collegial working atmosphere during all the years. I highly appreciate the interest you took in my work, the time you spent for discussing and finally proofreading it.

In recognition of all her help and support concerning the preparation and characterization of the ultra-microtomed specimens I would like to thank Ulrike Kunz. Further thanks should also go to Dr. Nathalie Benker and Dr. Ralf Theissmann for their kind introduction into the field of transmission electron microscopy and their assistance at the microscope. I also want to express my thanks to Dr. Lars Giebler and Hanna Hahn for the BET measurement.

I wish to thank Dr. Carsten Cremers, Franz Schweiger, Werner Seliger and Martin Scholz from the ZAE Bayern for the trustful cooperation within the Sino-German project 'Characterization of the three-phase boundary in differently synthesized membrane-electrode assemblies' and to acknowledge their contribution of MEA samples to this work.

Special thanks also go to my colleague and flat mate Robert Schafranek for the great time we spent together as well as for his contribution of XPS measurements for the ruthenium oxide supported platinum catalysts.

Further, I would like to thank Rongrong Chen from the Department of Mechanical Engineering at the Indiana University-Purdue University Indianapolis for her kind contribution of AFM images from electrode thin-sections.

I am grateful to all the staff from the workshop of the institute for their professional craftsmanship and technical assistance. Further I would like to thank Michael Weber, Heinz Mohren and Jean Christophe Jeaud for their aid in solving

technical problems with the instruments and their continuous work to keep everything going.

For both kindness and for the clear professionalism with which she proffered assistance in administration I would like to thank Maria Holzmann.

I would also like to thank all my other colleagues from the group of structural research and renewable energies that contributed directly or indirectly to this work by providing an interesting and pleasant working atmosphere throughout the past years.

I cannot thank enough Prof. Xingping Qiu for his welcoming kindness, his support and all he made possible for me during my stay in China. Thanks to his kindness and those of his students my stay in China became one of my most valuable experiences, I will always memorize with joy.

My very special thanks go to Sunjie, Caolin and Yuli for all the help, assistance and friendship they gave me and without which I would have been lost more than once in that country.

I would also like to thank all the other students from Tsinghua University that I had the pleasure to meet and that made my stay an unforgettable memory.

Finally, financial support of the work by the Deutsche Forschungsgemeinschaft in the context of the of the Sino-German project 'Characterization of the three-phase boundary in differently synthesized membrane-electrode assemblies' is also greatly acknowledged at this point.

KURZBESCHREIBUNG

Polymer-Elektrolyt-Brennstoffzellen (PEFC) besitzen eine komplexe Elektrodenstruktur, die in der Regel aus einem Katalysator, einem Katalysatorträger, einem Polymerelektrolyten und Poren besteht. Die eingesetzten Materialien sind weitgehend amorph, besitzen eine stark defektbehaftete Struktur oder liegen als nur wenige Nanometer große Partikel vor. In der Elektrode aggregieren die Materialien, was zu stark ungeordneten Strukturen führt. Beide Aspekte erschweren eine systematische Strukturanalyse erheblich.

Eingehende Kenntnisse der Elektrodenstruktur sind jedoch notwendig, um eine systematische Weiterentwicklung voranzutreiben und um ein besseres Verständnis von Stoff- und Ladungsträgertransportprozessen in der Elektrode zu erlangen. Aufgrund der komplexen Struktur der Elektrode wurde in dieser Arbeit ein Ansatz basierend auf der elektronenmikroskopischen Untersuchung von Elektrodendünnschnitten gewählt, um die Elektrodenstruktur experimentell abzubilden.

Die vorliegende Arbeit stellt diese mittels Elektronenmikroskopie durchgeführte Untersuchungen der Elektrodenstruktur dar. Untersucht wurden grundlegende Fragestellungen wie der Einfluss der Polymerelektrolytkonzentration sowie der Polarität des während der Herstellung verwendeten Lösungsmittels. Besonderes Augenmerk wurde dabei auf die Verteilung und die Struktur des Polymerelektrolyten gerichtet. Ein wesentliches Problem der Untersuchungen stellte der geringe Kontrast zwischen dem Polymerelektrolyten, dem Katalysatorträgermaterial und dem Einbettmittel dar. Daher wurden verschiedene Techniken hinsichtlich ihrer Eignung zur Kontrastverbesserung untersucht. In diesem Zusammenhang wurde auch ein Computer unterstütztes Aufnahmeverfahren für energiegefilterte Transmissionselektronenmikroskopie (EF-TEM) entwickelt. Das Aufnahmeverfahren ermöglicht eine erhebliche Erweiterung des abbildbaren Probenbereiches. Gleichzeitig war es möglich, eine deutliche Reduzierung der Strahlenschädigung und des Probendrifts zu erzielen. Dadurch war es möglich, den Polymerelektrolyten in der Elektrode eindeutig zu identifizieren. Es konnte weiterhin gezeigt werden, dass der Polymerelektrolyt den Katalysator und den Katalysatorträger nicht nur einhüllt, sondern in den Poren der Elektrode eine komplexe

Struktur bestehend aus faser- und filmartigen Strukturen ausgebildet. Darüber hinaus lieferten die aus EF-TEM Untersuchungen erhaltenen Ergebnisse ein starkes Indiz für das Eindringen des Polymerelektrolyten in Katalysatoragglomerate.

Desweiteren wurde ein neues Konzept für die Untersuchung von Multi-Komponenten-Strukturen, bestehend aus Membran, Elektroden und Gasdiffusionsschicht (GDL) entwickelt. Damit war es möglich das Eindringen einzelner Kohlenfasern aus der Gasdiffusionsschicht in die Elektrode nachzuweisen sowie den Einfluss der GDL-Struktur auf die Delamination der Elektrode aufzuzeigen.

Ein weiterer Teil der Arbeit befasst sich mit der Charakterisierung eines neuartigen auf mit Rutheniumdioxid beschichteten Kohlenstoff-Nanoröhren (CNT) abgeschiedenen Platin-Katalysators, der in enger Zusammenarbeit mit einem chinesischen Partner an der Tsinghua Universität (Peking) entwickelt wurde.

ABSTRACT

Polymer electrolyte fuel cells (PEFC) have a complex electrode structure, which usually consists of a catalyst, a catalyst support, a polymer electrolyte and pores. The materials used are largely amorphous, have a strong defective structure or have particle diameter of only a few nanometers. In the electrode the materials form highly disordered aggregated structures. Both aspects complicate a systematic structural analysis significantly.

However, thorough knowledge of the electrode structure, is needed for systematic advancement of fuel cell technology and to obtain a better understanding of mass and charge carrier transport processes in the electrode. Because of the complex structure of the electrode, an approach based on the examination of electrode thin-sections by electron microscopy was chosen in this work to depicting the electrode structure experimentally.

The present work presents these studies of the electrode structure. Some fundamental issues as the influence of the polymer electrolyte concentration and the polarity of the solvent used in the electrode manufacturing process were addressed. During the analysis particular attention was paid to the distribution and structure of the polymer electrolyte. A major problem to the investigations, were the low contrast between the polymer electrolyte, the catalyst support material and the embedding resin. Therefore, different techniques were investigated in terms of their ability to improve the contrast. In this context, a computer-assisted acquisition procedure for energy filtered transmission electron microscopy (EF-TEM) was developed. The acquisition procedure permits a significant extension of the imageable sample. At the same time, it was possible to substantially reduce beam damage of the specimen and to minimize drift of the sample considerably. This allowed unambiguous identification of the polymer electrolyte in the electrode. It could further be shown, that the polymer electrolyte not only coats the catalyst and catalyst support, but that it forms a complex structure consisting of fiber and film like structures in the pores of the electrode. In addition, the EF-TEM result delivered a strong indication for the infiltration of catalyst agglomerates by the polymer electrolyte.

Furthermore, a new concept for the investigation of multi-component structures, consisting of the membrane, electrodes and gas diffusion layers (GDL) was developed. Thus it was possible to provide evidence for the intrusion of individual carbon fibers from the GDL into the electrode. In addition the influence of GDL structure on delamination of the electrode could be demonstrated.

Another part of the work deals with the characterization of a novel platinum catalyst deposited on hydrous ruthenium oxide coated carbon nanotubes (CNT), which was developed in close cooperation with a Chinese partner at Tsinghua University (Beijing).

TABLE OF CONTENTS

1. <i>Introduction</i>	I
2. <i>Fundamentals</i>	7
2.1. <i>Electrochemical reactions</i>	7
2.2. <i>Standard Fuel Cell Set-Up</i>	8
2.2.1. <i>The gas distribution plates</i>	9
2.2.2. <i>The gas diffusion layer (GDL)</i>	9
2.3. <i>The Membrane Electrode Assembly</i>	11
2.4. <i>Origin of the Cell Potential</i>	14
2.4.1. <i>Electrode kinetics</i>	17
2.4.2. <i>Reactant Transport</i>	20
2.5. <i>Charge Transport</i>	25
2.5.1. <i>Electron Conduction</i>	26
2.5.2. <i>Proton Transport</i>	27
3. <i>Experimental</i>	33
3.1. <i>MEA Preparation</i>	33
3.2. <i>Characterization of Catalyst Samples</i>	33
3.2.1. <i>Gas Adsorption (BET)</i>	34
3.2.2. <i>X-ray Photoelectron Spectroscopy (XPS)</i>	34
3.2.3. <i>X-ray Diffraction (XRD)</i>	34
3.2.4. <i>Transmission Electron Microscopy</i>	35
3.3. <i>Characterization of MEA Samples</i>	36
3.3.1. <i>Ultra-Microtomy</i>	36
3.3.2. <i>Scanning Electron Microscopy</i>	39
3.3.3. <i>Transmission Electron Microscopy</i>	41
4. <i>TEM Image Acquisition</i>	42
4.1. <i>Beam Damage of the Specimen</i>	44
4.2. <i>Specimen Drift</i>	47
4.3. <i>Requirements for the Image Acquisition Procedure</i>	48

4.4.	<i>Image Positioning and Drift Correction</i>	50
4.5.	<i>Measurement of Image Drifts</i>	52
4.6.	<i>Recording Procedure</i>	53
4.7.	<i>Processing of Energy Filtered Images</i>	55
4.7.1.	<i>Averaging of Image Data for Noise Reduction</i>	55
4.7.2.	<i>Background Correction</i>	56
4.7.3.	<i>Automatic Image Reconstruction</i>	59
4.8.	<i>Conclusion</i>	60
5.	<i>Catalyst - Polymer electrolyte Interactions in the Liquid</i>	63
5.1.	<i>State of the Polymer Electrolyte in Solution</i>	65
5.2.	<i>Catalyst - Electrolyte Interaction in Solution</i>	68
5.2.1.	<i>TEM Characterization of Catalyst Dispersions</i>	70
5.3.	<i>Conclusion</i>	75
6.	<i>Pore Structure & Electrolyte Distribution</i>	76
6.1.	<i>Section Morphology</i>	79
6.2.	<i>Analysis of a Standard Electrode</i>	84
6.2.1.	<i>SEM Investigation</i>	85
6.2.2.	<i>TEM Investigation</i>	89
6.2.3.	<i>Statistical Analysis by Auto-Correlation</i>	92
6.3.	<i>Influence of the Polymer Electrolyte Content and Solvent</i>	96
6.3.1.	<i>Polymer electrolyte Content</i>	96
6.3.2.	<i>Influence of the Solvent</i>	102
6.4.	<i>Conclusion</i>	105
7.	<i>Element Mapping & Staining Experiments</i>	106
7.1.	<i>Staining</i>	106
7.1.1.	<i>Experimental</i>	107
7.1.2.	<i>Cesium (Cs⁺) Staining</i>	107
7.1.3.	<i>Barium (Ba²⁺) Staining</i>	109
7.1.4.	<i>Phospho-Tungstic-Acid (PTA) Staining</i>	112
7.2.	<i>Element Mapping</i>	115
7.3.	<i>Conclusion</i> ..	123

8.	<i>Electrode Interfaces</i>	I24
8.1.	<i>Membrane-Electrode Interface</i>	I24
8.1.1.	<i>Experimental</i>	I24
8.1.2.	<i>Results</i>	I27
8.2.	<i>Electrode-GDL Interface</i>	I28
8.2.1.	<i>Experimental</i>	I30
8.2.2.	<i>Results</i>	I30
8.3.	<i>Conclusion</i>	I33
9.	<i>Catalysts for Direct Methanol Fuel Cells</i>	I37
9.1.	<i>Methanol Oxidation</i>	I37
9.2.	<i>Hydrous Ruthenium Oxide Based Catalysts</i>	I39
9.2.1.	<i>Hydrous Ruthenium Oxide as Catalyst Support for DMFC</i>	I41
9.2.2.	<i>Catalyst Preparation</i>	I42
9.2.3.	<i>MEA preparation</i>	I42
9.2.4.	<i>Structural Characterization</i>	I43
9.2.5.	<i>Electrochemical Measurements</i>	I47
9.2.6.	<i>Fuel Cell Tests</i>	I49
9.3.	<i>Conclusion</i>	I54
10.	<i>Catalysts Supported on Hydrous Ruthenium Oxide Coated CNTs</i>	I55
10.1.	<i>Catalyst Synthesis</i>	I57
10.2.	<i>Experimental</i>	I59
10.3.	<i>Structural Characterization</i>	I60
10.4.	<i>Conclusion</i>	I72
11.	<i>MEAs Made of Pt/RuO₂/CNT Catalysts</i>	I74
11.1.	<i>Structure of the catalyst network</i>	I74
11.2.	<i>Polymer Electrolyte Distribution</i>	I76
11.3.	<i>Conclusion</i>	I78
12.	<i>Final Conclusion & Outlook</i>	I81

Part I

Introduction

I. INTRODUCTION

In the context of today's discussion about a more efficient use of the world's energy resources, fuel cells have been identified as a possible key technology in a future energy conversion and management system, as they are highly efficient and easily scalable energy converters, that, if fueled with hydrogen or bio-organic fuels, are even essentially CO₂ emission free or neutral.

Among the various types of fuel cells, the polymer electrolyte fuel cell (PEFC), which is also the subject of this study, possesses a number of highly advantageous features such as low operation temperature, sustained operation at high current density, low weight, compactness, long stack life, fast system start-ups and suitability for discontinuous operation [185], which makes it an attractive candidate for a wide variety of applications ranging from stationary power supplies over portable solutions to transportation.

Although much progress has been made in PEFC technology over the past two decades, some technological problems still remain before PEFC powered products will become commercially available to a larger market. From a commercial point of view two major issues need to be solved. These are a further reduction of cost and an increased long-term stability, i.e. increased stack life time. While production costs may benefit from upscaling effects for most fuel cell components, a contrary effect can be expected for the catalyst, which is responsible for about 40% of the costs in current state-of-the-art PEFC cells [185]. The high catalyst costs are due to the dependence on platinum based catalyst, as no other catalyst material can currently compete with platinum in terms of catalytic activity and chemical stability at PEFC operating conditions. To make things worse, the low abundance of platinum will invariably lead to increasing commodity prices once a higher demand is generated by expanding PEFC production, intensifying even the problem of high catalyst costs.

The challenge of reducing PEFC cost to commercially acceptable prices can therefore only be met, if the catalyst loading can be further decreased while maintaining or even improving the power density of current state-of-the-art PEFC cells.

Currently, state-of-the-art PEFCs have power densities of up to 0.7 W/cm^2 at cell voltages as high as 0.68 V . This is achieved with catalyst loadings being typically in the range of $0.6\text{-}0.8 \text{ mg/cm}^2$ [70]. This corresponds to a platinum-specific power density of about $0.85\text{-}1.1 \text{ g}_{\text{Pt}}/\text{kW}$, which is about $72\text{-}94 \text{ g}$ of platinum for a 85 kW fuel cell stack to power a $75 \text{ kW}_{\text{net}}$ automotive fuel cell system.

In a recent review Gasteiger pointed out that for reasons of cost reduction and Pt supply limitations the platinum-specific power density needs to be reduced to less than $0.2 \text{ g}_{\text{Pt}}/\text{kW}$ for large scale automotive applications [41]. In addition, the cell voltage at which this power density is obtained must exceed 0.65 V to assure a sufficiently high energy efficiency of the fuel cell system (a cell voltage of 0.65 V corresponds to an energy efficiency of about 55% based on the thermodynamic H_2/air potential at $80 \text{ }^\circ\text{C}$ and a near ambient pressure). Gasteiger proposes two strategies by which this goal might be reached:

- An increase of the power density to $0.8\text{-}0.9 \text{ W/cm}^2$ at 0.65 V by reducing the mass-transport induced voltage losses.
- A reduction of the platinum loading to 0.15 mg/cm^2 by implementing Pt-alloy catalysts on the cathode side with an 2-4 fold increased mass activity over state-of-the-art pure platinum on carbon catalysts.

Mass-transport-induced voltage losses are strongly linked to the structure of the electrodes [36,165,193] as well as that of the diffusion media [104,203] and flow fields [198,59]. While the influence of the diffusion media and the flow fields can be considerable, this work focusses almost exclusively on the electrode, since it contains the electrochemically active catalyst and acts both as a source or sink for reactants, water, protons and electrons.

The electrode possesses a highly complex structure, as it must accommodate the different transport processes on extremely small length scales to provide a reactive environment for fuel conversion. To realize the various transport processes, fuel cell electrodes consist of a mixture of different materials, being both organic and inorganic. Most of these materials are either amorphous, possess a poor long range order or have particle dimensions of only a few nanometers. In addition, this highly heterogeneous structure contains features, which span over a wide range of length scales. This makes the structural characterization of the elec-

trode extremely difficult and most of the classical structural analysis techniques fail due to the complexity of the structure or provide only incomplete information. For instance mercury porosimetry, which has been widely used to study the electrode pore structure, may provide statistically averaged pore size distribution data, but fails to provide information how these pores are locally distributed in the electrode layer. Experimental techniques to gain structural information on other electrode components like the agglomerated catalyst support or the polymer electrolyte are even less established or do not even exist at all. Therefore, until today the knowledge of the exact electrode structure is limited.

However, tailoring electrodes with improved mass transport properties requires experimental techniques, which allow a thorough characterization of the electrode structure. Furthermore, experimental techniques are needed to investigate changes of the electrode structure due to catalyst or polymer electrolyte degradation, which can significantly reduce PEFC lifetime. In addition, experimental data of the electrode structure may help to refine theoretical models of fuel cell electrodes used to simulate transport processes in the electrode and to properly predict current distributions and voltage losses at various operating conditions.

For complex multi-component structures like fuel cell electrodes only imaging techniques are capable to explore the full range of structural detail. Since the transport channels in a fuel cell electrode extend in all three spatial dimensions to form an interconnected network, 3D imaging of the electrode structure would be most desirable. However, although much progress has been made in the development of 3D imaging techniques such as X-ray, electron or neutron tomography [129,108,141], these imaging techniques either still fail to provide the necessary resolution (X-ray and neutron tomography) to map the structural details of the electrodes or are limited to rather small sample sizes (electron tomography). Therefore, a 2D approach based on electron microscopy was chosen for the characterization of the electrode structure. The 2D approach may also be justified by geometrical considerations about the electrode structure. PEFC electrodes are generally planar with an extremely large width-to-height aspect ratio and the coating techniques used to prepare the electrodes should result in mostly isotropic structures in the x-y plane of the electrode [113]. A 2D representation of the electrode may therefore be sufficient to reconstruct a 3D model using statistical methods.

During the development of a suitable characterization technique, special attention was paid to the structure and distribution of the polymer electrolyte inside the electrode, since it not only controls proton transport but also influences mass transport in the electrode by changing the structure and hydrophilicity of the pore space.

The developed characterization techniques were applied to standard electrodes based on carbon black supported catalyst and newly carbon nanotube supported catalysts developed in close cooperation with project partners at Tsinghua University (Beijing, China) and the Center for Applied Energy Research (Munich, Germany).

Part 2

Fundamentals

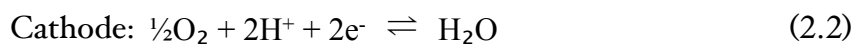
2. FUNDAMENTALS

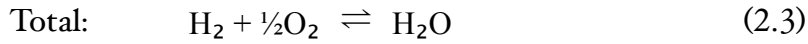
Fuel cells convert chemically stored energy by an electrochemical process into electrical energy. In this respect they are similar to batteries or accumulators. However, in contrast to batteries and accumulators, fuel cells do not store the chemical energy in the cell but use an external reservoir for fuel storage. This property is highly beneficial for a lot of applications, as it decouples the power density of the converter from the capacity of the energy reservoir.

The reactants commonly used in polymer electrolyte fuel cells are hydrogen and oxygen. Other types of polymer electrolyte fuel cells using hydrocarbon fuels instead of hydrogen exist too, but are less frequently used. The most prominent variant of these hydrocarbon fuel cells is the direct methanol fuel cell (DMFC). A major advantage of using methanol is that it is liquid at ambient conditions. This strongly reduces the efforts for fuel storage and handling when compared to hydrogen, which needs either be strongly pressurized or cooled to liquid hydrogen temperature (20 K) to increase its storage capacity. The processes involved in the electrocatalytic oxidation of methanol are much more complex than in the case of hydrogen. However, the basic thermodynamic and electrochemical principles are similar for both hydrogen and methanol oxidation. Therefore, this chapter focuses exclusively on hydrogen fueled polymer electrolyte fuel cells.

2.1. ELECTROCHEMICAL REACTIONS

In the cell the otherwise simultaneous reduction and oxidation of oxygen and hydrogen are confined in two locally separated reaction compartments. The two reaction compartments are separated by a polymer electrolyte membrane, which impedes the permeation of gases. On the anode side, hydrogen diffuses to the anode catalyst where it dissociates into protons and electrons, while on the cathode catalyst, oxygen reacts with electrons and protons to form water.





Since the membrane is electrically insulating, at open circuit, electrons cannot flow from the anode to the cathode and a potential difference, equal to the difference of the chemical potential of the two half cell reactions, establishes. If the circuit is closed, electrons flow from the anode side to the cathode side driven by the potential difference of the electrodes. For charge balance protons migrate through the membrane to the cathode. This results in an electric current which can be used to power an electric load.

2.2. STANDARD FUEL CELL SET-UP

In a standard single-cell setup a PEFC consists of five functional parts (Fig. 2.1). Two gas distribution plates to feed the reactant gases into the anodic and cathodic cell compartments, two gas diffusion layers (GDL) to achieve a more dispersed distribution of the gases on the electrode layers and a membrane electrode assembly (MEA), which is the core part of the fuel cell and contains the

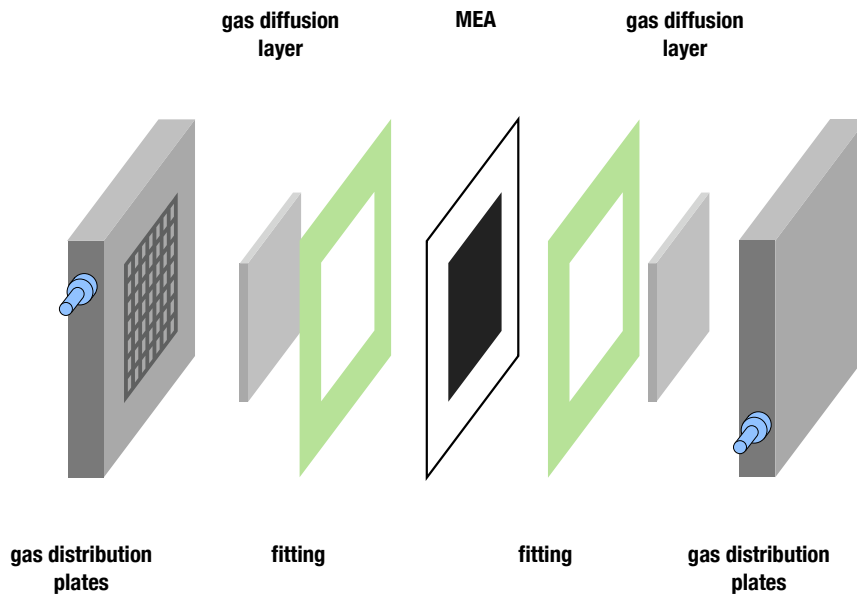


Figure 2.1. Schematic drawing of a standard polymer electrolyte fuel cell setup.

electrodes, where the electrochemical reactions take place, separated by a proton conducting membrane.

2.2.1. THE GAS DISTRIBUTION PLATES

The gas distribution plates have engraved or embossed structures, generally termed flow fields, to coarsely distribute the reactant gases over the active electrode area. Various designs have been developed for the flow fields of PEFCs, which may be grouped in the following categories: i) channels, ii) fingers and iii) feet or mesh like structures. Among the important design parameters for the flow fields is their blocking factor, which is defined as

$$\beta = \frac{\text{blocked area}}{\text{total electrode area}} \quad (2.4)$$

their pressure distribution over the electrode area and their preposition to flooding. The latter is an important aspect as at least at the cathode side product water can condense and block parts of the flow fields. In this respect single channel structures have an advantage compared to multi-channel (finger) or feet-like structures as water will be pressed out of the channel structure if the channel is blocked by water. In multi-channel structures the streaming gas can bypass the blocked channel, making these structures more susceptible to flooding. However, this is payed by higher pressure losses due to the long channel lengths of these flow field types. The geometry of the flow field therefore can have a significant impact on the performance of a PEFC. But in contrast to the structures of the electrode and gas diffusion layers its structure is well defined and standard fluid-dynamic software packages can be used to model the properties of various flow field geometries [32,64].

2.2.2. THE GAS DIFFUSION LAYER (GDL)

The gas diffusion plates are followed by a highly porous GDL. The GDL has to fulfill several tasks. Its main task is the compensation of the rather inhomogeneous distribution of reactants by the flow fields. Ideally it must provide an almost homogeneous distribution of reactants over the whole electrode area, i.e. also to

parts blocked by the flow fields like the channel walls. In addition the GDL must provide an electric contact to parts of the electrode layer not contacted by the flow fields and has to protect the MEA against mechanical mounting forces.

The GDL is commonly made of carbon fiber materials hydrophobized with polytetrafluoroethylene (PTFE). The hydrophobization is used to prevent flooding of the GDL by product water or water condensing from the humidified gas streams. The carbon fibers in the GDL are either randomly arranged (carbon paper or carbon felt) or are woven into textile like sheets (carbon cloth). In its uncompressed state the GDL has a quite high porosity of up to 80 %. However, the forces exerted on it by the flow fields during the mounting of the cell lead to a significant compression of the GDL and therefore a loss of porosity [88]. The pores enclosed by the carbon fibers in the GDL are typically in the micrometer range (5 - 100 μm) [201,165]. In comparison the pores inside the electrode layer are significantly smaller (~ 5–200 nm) [165,168]. To obtain a better transition between the rather coarse pores of the GDL and the finer pores of the electrode the GDL is frequently coated with a layer consisting of carbon black and PTFE powder. This micro-porous layer (MPL) is supposed to provide a better electronic contact between the GDL and the electrode layer and to improve the transport connection between the two largely distinct pore spaces. It has also been reported that the graded porosity of the electrode, micro-porous and gas diffusion layer has a beneficial effect on the removal of liquid water through a differential capillary pressure acting normal to the layer structure [160].

The MPL contains a wide range of different pore sizes. Pore sizes ranging from 0.006 to 300 μm have been reported in literature [82, 89]. The pores in the MPL have been classified into three different pore ranges: macropores in the range of 10–100 μm , mesopores in the range of 0.1–10 μm , and micropores below 0.1 μm [75, 82]. It should be noted that the definition of pore ranges as used for the MPL is not consistent with standard IUPAC definition of micro-, meso- and macropores. By comparing the electrochemical performance of fuel cells equipped with gas diffusion layers of varying micro- to macropore ratios Kong et al. concluded that tailoring their ratio is more important than the total porosity to decrease mass-transport limitations [82]. The role of the micropores was explained by water condensation, which occurs earlier in small pores. According to the Kelvin equation water condensation will occur before the vapor pressure

reaches the saturation pressure at a given temperature in pores smaller than a critical pore-size. The micropores in the MPL may therefore prevent the macropores from flooding with water by absorbing water like a sponge. A similar result was reported for the hydrophobic and hydrophilic pore space. Commonly, PTFE is added to the MPL to increase its hydrophobicity and hence to decrease its flooding probability. However, in a study of Wang et al. composite carbon black layers consisting of a hydrophilic carbon black (Black Pearls 2000) and a more hydrophobic carbon black (Acetylene Black) were investigated [178]. The composite layers showed improved mass-transport properties as compared to layers prepared of only one carbon material. It was concluded by the authors that the hydrophobic pore space of the Acetylene Black provides a pathway suitable for gas transport but that water removal is enhanced by the addition of a more hydrophilic pore space. Hence, the bifunctional task of the MPL to transport at the same time gas and water should be reflected also by a bifunctional pore structure adapted to the two different transport processes.

2.3. THE MEMBRANE ELECTRODE ASSEMBLY

The core part of a polymer electrolyte fuel cell is the membrane electrode assembly (MEA). It consists of a proton conductive polymer electrolyte membrane, which is coated on both sides with a thin electrode layer. The electrode layers contain the catalyst and a polymer electrolyte. Further PTFE [114,186] or other additives [23,38,165] are added to make the electrode more hydrophobic or to influence its pore structure.

State-of-the-art MEAs generally use platinum based catalysts supported on carbon materials. Often carbon blacks are used as catalyst support, which are similar or even identical to those used for the MPL. However, also other support materials like carbon nanotubes [17,176] or mesocarbon microbeads [97] have recently been reported for fuel cell catalysts. When carbon black supported catalysts are used, the electrode layer is structurally similar to the MPL, because, due to its rather low density, the carbon support generally constitutes the main solid phase volume of the electrode layer and hence has a significant influence on its structure.

However, there are some fundamental differences when compared to the MPL. While the bifunctional and bi-directional transport of gas and water in the GDL and MPL is already quite delicate, the situation in the electrode layer becomes even more complex. In addition to the pressure driven fluid-flow of reactants and water another transport process, namely the transport of protons, becomes important [123].

In contrast to the GDL and MPL, the transport processes in the electrode layer cannot be separated geometrically to different structural parts like hydrophilic (micro-) pores for water and hydrophobic (macro-) pores for gas transport, respectively. This is due to the catalyst being homogeneously distributed on the carbon support and therefore being exposed to both the micro- and macro-pore space. Therefore, in the electrode layer maximum catalyst usage can only be achieved if both the micro- and macro-pore space is accessible to the reactants and proton transport is granted to all catalytically active sites. These boundary conditions are hard to comply, since apart from the transport of reactants and water, which share the same pore space, each of the transport processes is realized by a different component in the current PEFC design. The various transport processes and their attribution to the different electrode components is illustrated in Figure 2.2. The structure and therefore the transport properties of these components are strongly interconnected (symbolized by dashed arrows in Figure 2.2). Optimization of the transport properties can therefore not be carried out independently. For instance an increase of the polymer electrolyte content to improve proton conduction leads to a decrease of porosity [48,168] and therefore introduces mass-transport limitations for the supply of reactants.

The electrode layer is reported to contain two distinct pore ranges [183,168]. These two pore ranges are attributed to two different agglomeration or aggregation processes of the carbon black composing the layer. Carbon blacks consist of near-spherical (primary) particles of colloidal sizes ($\sim 8 - 500$ nm) coalesced into aggregates or agglomerates of several hundred to a few micrometers [122]. The pores found inside the agglomerates, i.e. the pores in between the primary particles of the carbon black, account for the first of the two pore ranges. The second pore range is attributed to pores between the agglomerates formed by the primary particles.

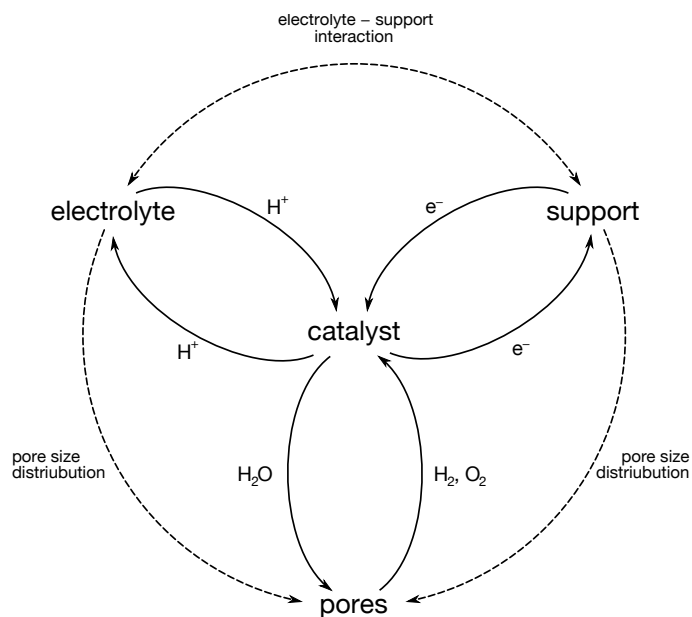


Figure 2.2. *Illustration of the relation between the structural components of the electrode and the transport processes they promote.*

In literature, the pores of the first pore range are commonly referred to as primary pores or micropores, while for the latter the term secondary pores or macropores is used. In this work, the designation primary and secondary pores will be used instead of micro- and macropores as the size range of the primary pores is not consistent with the IUPAC definition of micropores, and therefore the term micropore may be misleading. In fact, no precise boundaries can be specified for the two regions as the definition for the primary and secondary pores is rather phenomenological. In practice, the boundaries of the primary and secondary pore range depend on the type of carbon black material and the manufacturing process of the layer.

Uchida et al. [168] reported a boundary at 40 nm between the primary and secondary pore range, whereas Shin et al. [150] and Xie et al. [194] reported boundaries at 70 and 17 nm, respectively. Chisaka et al. [23] placed the boundary between the primary and secondary pores at 50 nm and fixed the lower

bound of the primary pores at 20 nm, a value even larger than the boundary region specified by Xie et al.

Apart from electrode pore size distributions little experimental data exists on the structure of the electrode. It is commonly assumed that the polymer electrolyte forms a coating layer on the pore walls formed by the catalyst or catalyst support particles and successively fills or floods them if its loading is increased [168,121,194]. However, SEM images of PEFC electrodes presented by Chisaka et al. [23] showed fiber-like polymer structures, indicating that the structure of Nafion which is commonly used as polymer electrolyte inside the electrode might be more complex than a simple coating of the catalyst and catalyst support particles.

2.4. ORIGIN OF THE CELL POTENTIAL

The voltage response of an electrochemical cell to an applied electrical load is called polarization curve and corresponds to the potential difference of the two electrode half cells. For an ideally reversible electrochemical cell the polarization curve is a flat line originating the cells thermodynamic equilibrium potential given by the Nernst equation [6]:

$$U_{rev} = \Delta E_{rev}^0 - \frac{RT}{nF} \ln Q \quad (2.5)$$

where ΔE_{rev}^0 is the difference of the electrode potentials at standard conditions, R the ideal gas constant, F the Faraday constant and Q the reaction quotient. However, at non equilibrium conditions irreversibilities of the electrochemical reactions lead to deviations from the equilibrium potential. Typically, the polarization curve of a PEFC has an s-shaped profile as illustrated in Figure 2.3.

It starts with a rather harsh voltage drop at low current-densities, followed by an almost linear part, which again drops down harshly at the high current end of the curve. Therefore, it is common to divide the polarization curve of a PEFC into three parts:

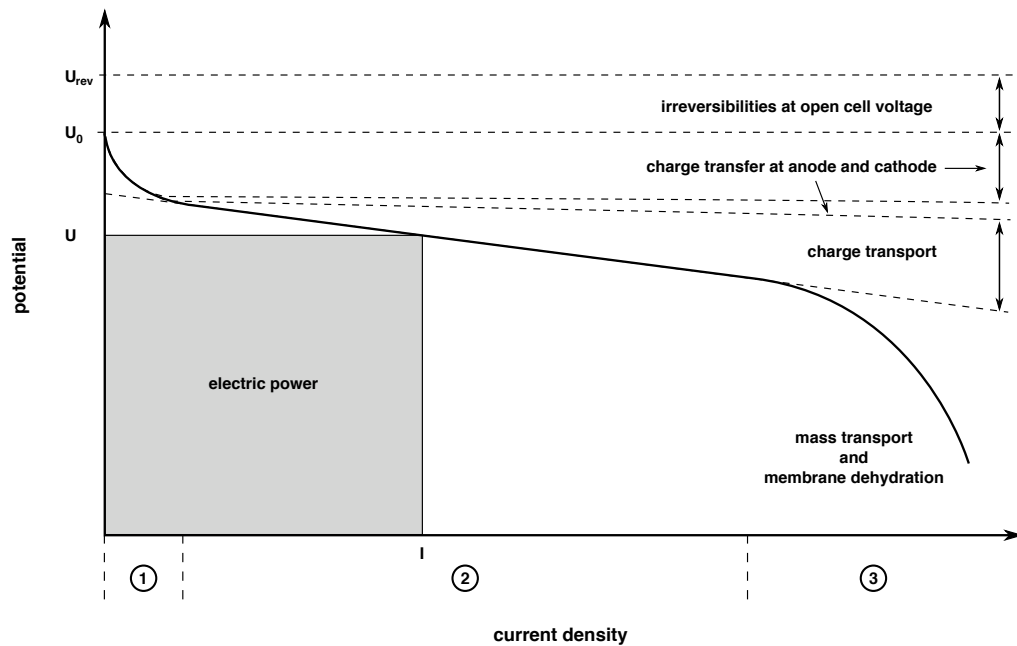


Figure 2.3. Schematic drawing of the characteristic current-voltage dependence of a PEFC.

- 1) A low current part from about 0-100 mA/cm², which is generally referred to as the electrokinetic part. This part is dominated by the kinetically activated charge transfer at the electrodes. The steepness of the potential drop at each electrode depends mainly on the catalyst material, the type of reactants (e.g. H₂, methanol or O₂) and the active surface area of the catalyst. In the PEFC running on hydrogen and oxygen (air) the voltage drop in the electrokinetic part is dominated by the potential drop at the cathode, because the oxygen reduction reaction (ORR) has a significantly higher activation energy than the hydrogen oxidation reaction (HOR). The individual contributions of the cathodic and anodic activation processes to the cell voltage are symbolized in Figure 2.3 by the two dashed lines.
- 2) The part succeeding the electrokinetic region is termed the ohmic part, since it shows an almost linear current-voltage dependence, obeying ohm's law. In this region the electric resistance associated with electron

and proton transport is mainly responsible for the voltage decrease. Due to the much lower proton conductivity, which even in fully wetted MEAs is in general two orders of magnitude lower than that of electrons [139, 48], the electric resistance in the MEA is dominated by proton conduction in the electrode and the membrane. Apart from electric resistance of the MEA, contact resistances between the individual parts of the PEFC (i.e. electrode, GDL and flow fields) also contribute to the overall cell resistance.

- 3) The voltage drop in the high current region is due to a depletion of reactants at the reaction sites, which leads to a concentration overpotential. At high current densities the conversion rate of the reactants reaches the rate at which fuel or oxidant is supplied and the concentration of reactants decreases significantly. Therefore, this part of the polarization curve is referred to as the mass-transport-limited region. The effect of mass transport limitation is usually strongest at the cathode, where especially at high current densities the formation of product water may lead to a blocking of the pore system by water condensation. Furthermore, the use of air as an oxygen source impedes the oxygen supply of the cell, as it contains only about a fifth of the oxygen concentration compared to pure oxygen.

However, the strict separation of the polarization curve into an electrokinetic, ohmic and mass-transport controlled region is only a rather simplified description of the processes controlling the shape of the polarization curve. For instance, mass-transport-limitations may also influence the steepness of the ohmic region [66,71] and changes of the ionic conductivity on the other hand, e.g. by dehumidification of the membrane at high current densities, may lead to a non-linear behavior of the polarization curve, resembling that caused by mass-transport-limitations [124]. Although the polarization curve is an indispensable tool for the characterization of PEFCs, the information it provides about electrochemical parameters is strongly limited and care must be taken in the interpretation of parameters obtained by fitting model equations to the polarization curve, if not confirmed by alternative methods.

Apart from the sources for overpotentials mentioned above, irreversibilities of the equilibrium state lead to a reduction of the open circuit voltage. The main sources for irreversibilities of the equilibrium state are the crossover of reactants from one electrode compartment to the other [85].

Another common source of overpotentials is the adsorption of non-reacting species on the catalyst surface, which impedes the adsorption of the reacting species and hence leads to the development of an adsorption overpotential [15]. Carbon monoxide is the major source of such non-reacting species for technical applications of PEFCs. Since purification of hydrogen is cost intensive, technical hydrogen is generally used for large-scale PEFC applications. Technical hydrogen is usually produced by the water-gas-shift reaction of hydrocarbons or coal and therefore contains carbon monoxide as an impurity. CO-tolerance of the anode catalyst is therefore an important design criteria for PEFCs used for instance in automotive applications. Pure platinum shows a rather bad CO-tolerance and large overpotentials are necessary to oxidize CO on platinum to CO₂. However, much progress has been made on the development of CO-tolerant fuel cell catalysts, which most often use ruthenium as co-catalyst for CO-oxidation [3].

2.4.1. ELECTRODE KINETICS

The electrocatalytic surface of the electrode acts as a source and sink of reaction products and educts. To understand the influences of transport processes on the electrode performance it is therefore necessary to understand the processes taking place at the catalyst surface.

To participate in an oxidation or reduction at an electrode, hydrogen or oxygen must diffuse through an electrolyte, adsorb on the catalyst surface, dissociate and adjust their hydration sphere as they receive or discard electrons. Likewise, species already adsorbed at the surface must be detached to accommodate for new reacting species. Because these processes are activated, the rate at which oxidation or reduction occurs depends on the activation energies of these processes and is determined by the process of the highest activation energy.

For hydrogen oxidation the dissociation of molecular hydrogen into surface adsorbed atomic hydrogen is generally considered the rate determining step. Oxy-

gen reduction is more complex, as the higher bond strength of the oxygen molecule requires a stronger electronic interaction of the catalyst with the oxygen molecule. In this case desorption may become the rate determining process. Further, interaction with co-adsorbed water molecules, which may lead to side products such as H_2O_2 further complicates the electrocatalytic reduction of oxygen [55].

Considering the following electrochemical reaction



where S_{ox} denotes the oxidized and S_{red} the reduced state of the species S , the rate at which the electrochemical reaction proceeds can be described by the Butler-Volmer equation:

$$j = j_0 \left[\exp\left(\frac{(1-\alpha)nF}{RT}\eta\right) - \exp\left(\frac{\alpha nF}{RT}\eta\right) \right] \quad (2.7)$$

Since the reaction shown in equation 2.6 is reversible both anodic and cathodic reactions take place simultaneously at the electrode and equation 2.7 contains two exponential terms describing the anodic and cathodic contribution to the reaction current in dependence of an applied overpotential η . In equation 2.7 j_0 is the so called exchange current density and α the charge transfer coefficient of the reaction, F and R denote the Faraday and the ideal gas constant, respectively, and T is the temperature at which the reaction takes place. The exchange current density is influenced by a number of factors. Most notably, it depends on the activation energy of the rate determining step for the electrochemical reaction, but it also has a dependence on the concentration of the reacting species and the size of the electrochemically active electrode surface. The charge transfer coefficient α in equation 2.7 is mainly a symmetry parameter that describes how strongly the energy transition state (i.e. the rate determining step) is affected by a change $\Delta\phi$ of the electrode potential as shown in Figure 2.4. It can take values between zero and unity and is close to unity if the transition state is located close to the electrode and zero when far apart. In general α takes an intermediate value and is usually close to 0.5.

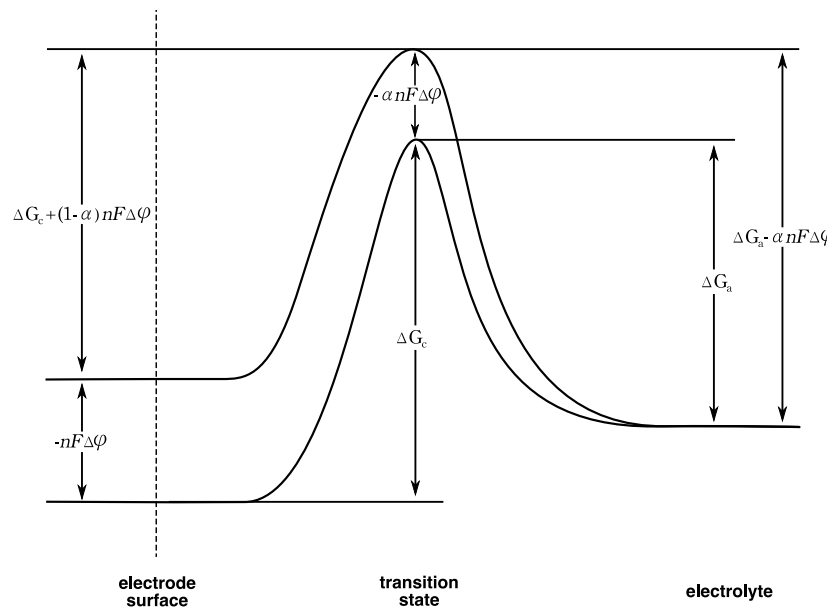


Figure 2.4. Energy diagram for an activated charge transfer process at an electrode surface. In the absence of an external potential the activation energy for a cathodic charge transfer process is ΔG_c and for an anodic charge transfer process ΔG_a . If the electrode potential is changed by an amount of $\Delta\phi$ the energy of the transition state is affected by $\alpha nF\Delta\phi$, which either speeds up or slows down the reaction speed of the anodic or cathodic reaction. The change in the internal energy curve is shown for a negative change of the electrode potential ($\Delta\phi < 0$).

On platinum catalysts, the hydrogen oxidation reaction (HOR) usually is fast and its symmetry factor is typically about 0.5. The oxygen reduction reaction (ORR) instead is much slower and represents the principal inefficiency in many fuel cell systems. Since the reverse reaction of the ORR is the oxidization of water, which has a very high activation energy, the ORR is irreversible and the symmetry parameter is usually close to unity.

Equation 2.7 is only valid, if the distribution of reactants is uniform inside the electrode and does not change with the variation of the overpotential. However, at least at high overpotentials, i.e. high current densities, the supply of reactants is generally not fast enough to maintain a constant reactant concentration throughout the whole electrode. In this case the concentration dependence of the electrode potential must be taken into account and equation 2.7 becomes:

$$j = j_0^{ref} \left(\frac{c}{c^{ref}} \right) \left[\exp \left(\frac{(1 - \alpha)nF}{RT} \eta \right) - \exp \left(\frac{\alpha nF}{RT} \eta \right) \right] \quad (2.8)$$

Although the charge transfer resistance has its origin in the energy states of the electrode and adsorbates as well as their modification by the electric field of the electrode, the electrokinetic overpotential which can be derived from equation 2.7 is also influenced by the electrode structure.

j_0 of equation 2.7 is defined as a current density being referenced to the electrochemically active surface area of the electrode. Ideally the electrochemically active surface area corresponds to the geometric surface of the catalyst particles. However, for PEFC electrodes the electrochemically active surface area is frequently less than its geometric one [21]. The ratio between the geometric and electrochemically active surface is generally referred to as the catalyst utilization and can be obtained from electrochemical measurements [15]. The discrepancy between the electrochemical and geometric surface is generally ascribed to an incomplete contact of the catalyst with the proton conductive electrolyte phase. Since the electrolyte in PEFCs is a polymer which can be considered to be largely immobile at normal PEFC operating conditions, the catalyst utilization and hence j_0 is directly linked to the polymer electrolyte distribution inside the electrode.

2.4.2. REACTANT TRANSPORT

Fast reactant transport to the catalytically active sites inside the electrode is crucial for PEFC cells to be operated at high load conditions required for automotive applications.

Reactant transport in a PEFC may be divided into three different transport processes:

- transport by pressure driven fluid flow.
- transport by gas phase diffusion.
- transport by diffusion through solid or liquid media [184].

Reactant transport in the flow fields occurs by pressure driven flow and is established by a pressure difference of the cell inlet and outlet. In the GDL and the electrode reactant transport is dominated by gas phase diffusion in pores. For large pores on the micrometer scale, present in the GDL or some parts of the electrode, gas phase diffusion can be described by ordinary diffusion following Fick's law or for more concentrated multicomponent systems by the generalized Stefan-Maxwell equations. Since the reactants are not free to move in the electrode and GDL but are confined to the open pore space, the diffusion coefficients of the reactants need to be corrected for the porosity and tortuosity of the structure. Frequently, a Bruggeman correlation of the form

$$D_{i,j}^* = D_{i,j} \cdot \varepsilon^\zeta \quad (2.9)$$

where $D_{i,j}$ is the diffusion coefficient of species i in j , ε the electrode or GDL porosity and ζ a tortuosity parameter describing the elongation of the diffusion path due to the pore structure of the electrode or GDL [184], is used for this purpose. In the electrode, which also contains a large amount of smaller pores of less than 100 nm, collisions of the reactant molecules with the pore walls become more frequent and Knudsen diffusion needs to be taken in to account, too. However, before the reactant can adsorb on the catalyst surface it generally needs to diffuse through a water or electrolyte film, as only those catalyst particles, which are in close contact with or covered by the electrolyte, are electrochemically active, due to the boundary conditions imposed by the electrochemical reaction. Because of the much lower solubility and diffusion speed in the electrolyte or condensed water, this last transport process frequently imposes the largest transport resistance.

In order to describe the diffusion processes taking place at the reactant (gas) - electrolyte - catalyst interface, several models have been developed. The oldest of which dates back to the year 1924 when Schmid introduced his model of the three-phase-boundary [143]. The model was originally developed for gas-diffusion electrodes with liquid electrolytes, but its validity was questioned and replaced by other models considering only two phase contacts [7]. Nevertheless, due to its simplicity this early model has very much influenced the scientific dis-

cussion about transport processes and is still being referenced in current literature.

Other electrode models like the thin-film or agglomerate model were developed later to better reflect the boundary conditions of dispersed catalyst systems. While these models use rather simple geometric boundary conditions, considering transport only in two dimensions, more realistic three-dimensional models were presented recently [179,180,113].

The Three-Phase-Boundary Model

The three-phase-boundary model assumes that the electrochemical reaction takes place only in a narrow region at the interface formed between the electrode, the electrolyte and the reactant gas. The model is based on the consideration, that the solubilities and diffusivities of hydrogen and oxygen in aqueous electrolytes are low. At room temperature and 1 atm. the solubility of both gases is about 10^{-6} mol/cm³ and their diffusion coefficients in the liquid are about 10^{-5} cm/s [54]. Therefore, the reaction zone is confined to a narrow region where the meniscus of the electrolyte formed at the interface is thin enough to allow rapid diffusion of the gases to the electrode surface (Figure 2.5).

Schmid already realized that such boundary conditions would considerably limit the electrode surface available for the electrochemical reaction and could not explain the experimentally obtained current densities for platinum sponge electrodes [143]. Therefore he concluded that reactant gas is also adsorbed at the non-wetted part of the electrode and is transported to the electrode-electrolyte interface by surface diffusion.

That diffusion of atomic hydrogen across the electrode surface has a significant influence on the electrode reaction was later questioned by others [187,16]. Will noted that a thin liquid film covers the electrode even above the electrolyte meniscus and concluded by a set of experiments raising or lowering the electrode above the electrolyte level, that the electrode reaction takes place at the part of the electrode covered by the thin film. However, the thin electrolyte film imposes a rather high ionic resistance for proton transport which limits the active

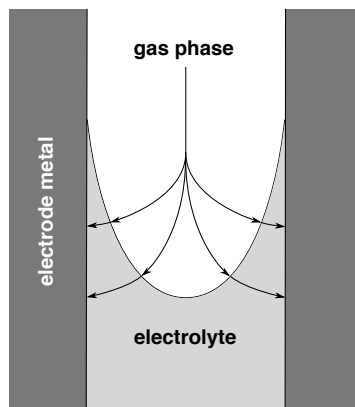


Figure 2.5. Illustration of the boundary conditions proposed for the three-phase-boundary model.

electrode area to a narrow region above the meniscus [187]. The work of Will represented a first evidence against the existence of true „three-phase-boundary“ as proposed by Schmid [143] and served as a basis for a new electrode model proposed by Austin et al. [7].

The Thin Film Model

While the work of Will was conducted at a Pt-wire electrode half immersed in H_2SO_4 , Austin et al. extended the model for porous gas diffusion electrodes and presented a mathematical treatment of their thin film model [7]. Austin et al. postulated that in a porous electrode containing both micro- and macropores only the micropores get filled with electrolyte by capillary forces while the macropores remain open due to a differential gas pressure. The macropores in this model are supposed to be wetted by a thin electrolyte film (Figure 2.6) to provide a suitable environment for the electrode reactions.

In this model mass transport is essentially perpendicular to the electrolyte film assuring short transport paths for reactant transport. However, under these boundary conditions charge carrying ions need to travel along the film giving rise to ohmic voltage gradients. Therefore, unless the film thickness becomes large

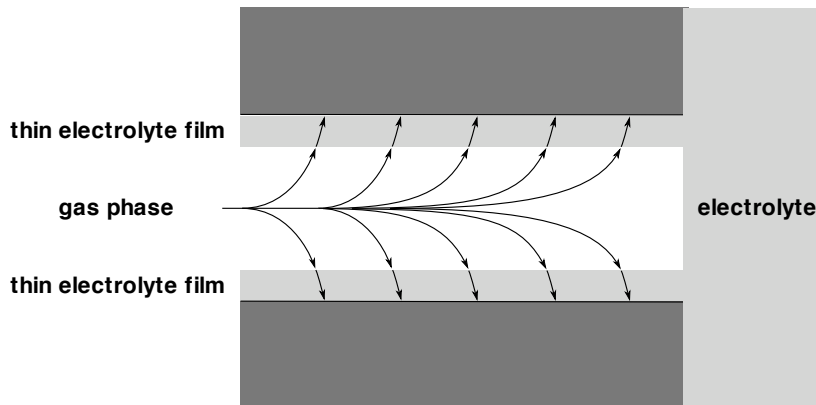


Figure 2.6. *Illustration of the thin film model as proposed by Austin et al. [7].*

compared to the lateral dimension of the film the electrode reaction is controlled by ohmic transport in the film instead of reactant transport. This is a rather untypical situation for fuel cells using liquid as well as polymer electrolytes and might be a reason why the model has not found wide acceptance in the scientific community.

The Flooded Agglomerate Model

Currently the best approximation to a real PEFC system is represented by the flooded agglomerate model. In the flooded agglomerate model [46], it is assumed that in the catalyst layer the dispersed catalyst (Pt/C) forms agglomerates filled with the electrolyte which are also covered with a thin film of pure electrolyte. Depending on the mathematical modeling the agglomerates are either treated as layers, cylinders or spheres. In between the agglomerate zones open hydrophobic channels exist through which the reactant gas can access the electrolyte film, where it dissolves and diffuses into the internal flooded parts of the agglomerate.

Although this model represents a rather approximate approach to the true 3D structure of the electrode, reasonable agreement between experimentally meas-

ured polarization curves and those predicted by the model has been reported [162,66]. Nevertheless, the model is not self-consistent so that several model parameters must be obtained by fitting to experimental values, which bears the risk of compensating deficiencies of the model and as a consequence to obtain model parameters with limited physical meaning.

Concerning mass transport limitations imposed by gas diffusion through the electrolyte layer model calculations of Bernardi et al. using an agglomerate model approach predicted, that electrolyte films up to 1 μm should not impose significant mass transport limitations [10].

3D electrode models

Further insight in the complex transport processes in the electrode layer may be obtained from 3D models. These models do not only reduce the number of free parameters but may also yield locally resolved potential and current distributions inside the electrode layer, which may provide not only valuable information to further improve the electrode structure but also to better understand electrode degradation processes. First 3D models, which applied partially 3D electrode structures, which were reconstructed from experimental data were reported recently from Mukherjee et al. [113]. However, their 3D models must still be considered incomplete, since they do not model the catalyst and polymer electrolyte as separate phases. Instead the authors decided to apply only a two phase approach using a mixed electron and proton conducting phase as well as a gas phase for the pores.

2.5. CHARGE TRANSPORT

In a PEFC system two types of charge transport occur simultaneously: i) electron transport and ii) proton transport. The main direction of charge transport in PEFC electrodes is perpendicular to the electrode layer, with opposing protonic and electronic currents.

For PEFC electrodes the bulk properties of the proton and electron conducting materials, which they are made of, cannot be applied, since only a fraction of the total electrode volume is occupied by the respective materials. To account for the different volume fractions of the electron conducting (catalyst + support), proton conducting (polymer electrolyte) and non-conducting phase (pores) a Bruggeman correction similar to those discussed for reactant transport (eqn. 2.9) is used:

$$\sigma = \sigma_0 \varepsilon^\zeta \quad (2.10)$$

where σ_0 is the bulk conductivity of the material. The tortuosity parameter ζ is often unknown and a value of 1.5 is assumed for numerical simulations of PEFC systems [181,184].

Since the transport processes involved in the conduction of electrons and protons differ considerably, they will be discussed separately in the following sections.

2.5.1. ELECTRON CONDUCTION

Electron transport inside the electrode layer is realized by the network of catalyst and catalyst support particles. For a continuous conduction path through the electrode layer, percolation between the individual particles must exist. Interparticle electron transfer takes place by activated carrier hopping. The activation energy associated with this process is determined by the interparticle interactions, which can be strongly perturbed by local changes in the dielectric function upon sorption of water or solvents and swelling of the electrode, which increases the mean particle to particle distance [139].

Saab et al. [139] showed that the electrode conductivity decreases quite dramatically upon wetting, lowering the electron conductivity from about 130 to 3-6 Sm^{-1} in their study for an electrode containing 33 wt.% Nafion. The effect of residuals from the preparation process of the electrode was examined in the same study. According to their results glycerol, which is frequently used as a dispersing agent in several electrode preparation processes, may remain in the electrode leading to a decrease of electronic conductivity by a factor of 5-10. The

effect of the polymer electrolyte concentration on the electrode conductivity was examined by Gode et al. [48]. Surprisingly the electronic conductivity did not decrease continuously with the polymer electrolyte content but showed a maximum at intermediate concentrations in the range of 30 – 50 wt.%. The lower electron conductivity of samples with low polymer electrolyte concentration was explained by a high porosity of these samples, which resulted in poor percolation of the catalyst particles.

However, despite the drastic reduction of the electronic conductivity by the effects mentioned above, the effective electron conductivity of the electrode is still one to two orders of magnitude higher than its proton conductivity [139,48]. Therefore, ohmic losses in the electrode are mainly due to transport of protons.

2.5.2. PROTON TRANSPORT

In PEFCs conduction by the polymer electrolyte is the dominant proton transport mechanism. However other proton transport mechanisms including surface conductivity effects [106,96], conduction in condensed water due to Nafion fragments [123,29] and proton conduction by conductive support materials [83] have been discussed in literature as well. Depending on the local structure of the electrode and the type of catalyst and catalyst support materials used these other transport processes may attain certain importance at least for short range proton transport.

Proton transport in the polymer electrolyte

In contrast to liquid electrolytes, which are used for instance in phosphoric acid fuel cells (PAFC) and alkaline fuel cells (AFC), the polymer electrolyte used in PEFCs is a complex multi-phase material.

At the time of this writing the most commonly used class of polymer electrolytes are perfluorosulfonated ionomers (PFSI). Nafion, which was developed and produced by the E. I. DuPont Company in the 1960s, is the most prominent electrolyte of that kind and has been widely used in academic research until today.

Nafion is obtained by copolymerization of a perfluorinated vinyl ether comonomer with tetrafluoroethylene [105] and has chemical structure given below:

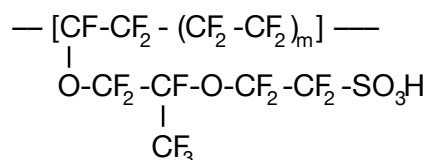


Figure 2.7. Chemical structure of Nafion.

As Nafion is a statistical copolymer the number tetrafluoroethylene units separating the sulfonic acid side chains cannot be specified exactly and m in this formula refers to the mean number of $\text{CF}_2\text{-CF}_2$ units. More common than the specification of the mean number of TFE units is the use of the equivalent weight (EW) to refer to Nafion modifications with different side chain concentrations. The equivalent weight is given by the number of grams of dry Nafion per mole sulfonic acid groups. For fuel cell applications often Nafion with an EW of 1100 is used. The EW and nominal film thickness of Nafion membranes is usually specified by a three digit number. The first two digits give the EW divided by 100 and the last digit specifies the film thickness in milli-inch.

The morphology of Nafion has been a matter of research since the 1970s, but to date there exists no universally accepted morphological model for its solid-state structure. However, it is generally accepted that Nafion consists of at least two phases formed by the ionic side chains and the polymer backbone respectively [105]. The source of the ongoing debate over the morphology of Nafion is its random chemical structure that is capable of organizing in complex crystalline and ionic domains with a significant distribution in dimensions over a wide range of length scales. Furthermore, the microstructure and properties of Nafion are known to be quite sensitive to its processing history [153], which often complicates direct comparison of experimental results. Although a number of microscopy studies has been published about Nafion [90,125,133,138], most morphological information is based on small angle scattering and wide angle diffraction data [105,60]. However, quantitative morphological information is limited by the fact that Nafion yields only a single, broad scattering maximum attributed to

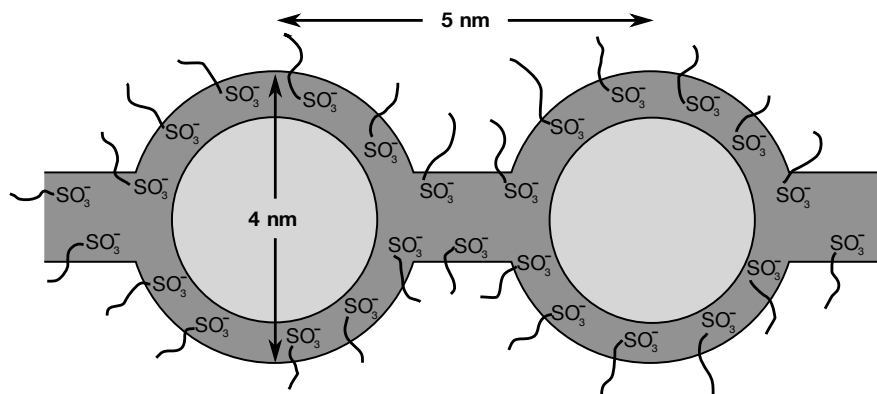


Figure 2.8. Cluster-network model of Nafion according to Gierke et al. [44].

characteristic dimensions within the ionic domains and the diffraction reflections of the PTFE-like crystallites.

In the most simplistic models the polymer electrolyte consists of two phases, a hydrophobic phase comprised of the polymer backbone and a hydrophilic phase containing the ionic side chains and water. Figure 2.8 shows a schematic drawing of the microstructure of Nafion as proposed by the cluster-network model of Gierke et al. [44]. In this model the water-swollen morphology of Nafion is described by ionic clusters that are approximately spherical in shape with an inverted micellar structure. This spherical ionic clusters are supposed to be interconnected by narrow channels of about 10 Å size to provide a percolation pathway for ionic transport.

The strong confinement of the aqueous phase to the ionic clusters leads to specific interactions of the charge carriers with the large internal interface and the ionic groups of the side chains. Therefore, the transport behavior of the proton conducting phase differs from an unconfined aqueous electrolyte and depends strongly on the degree of hydration, i.e. the swelling of the ionic clusters. The current picture of proton conduction in polymer electrolytes such as Nafion is, that the majority of excess protons is located in the central part of the hydrated hydrophilic nanochannels [83,105]. At high degrees of hydration the water in this region is almost bulk-like and proton transport occurs mainly by “structure

diffusion”, i.e. rearrangement of hydrogen bonds. With decreasing water content, the concentration of excess protons in the aqueous phase is increasing. This, in turn, increasingly suppresses intermolecular proton transfer and proton transport becomes essentially vehicular in nature. This means that proton transport at low degrees of hydration is mainly linked to diffusion of water, which serves as a vehicle for the transport of hydrated protons.

Proton transport in the absence of an electrolyte phase

In the absence of a proton conducting phase alternative routes for proton transport may take effect. Several different surface conductance processes have been discussed in literature including surface diffusion of adsorbed hydrogen on platinum [106,164], spillover of hydrogen and oxygenated species onto the support [96] and surface conductivity by functional groups on the support surface [96,106].

On platinum surfaces adsorbed hydrogen is highly mobile and can diffuse rapidly to electrolyte interface providing an alternative nonionic pathway to extend the active electrode area to regions not in contact with the electrolyte [106,164,123]. This process is also present in dispersed Pt-black electrodes which may even function without an additional electrolyte phase inside the electrode layer [164].

For supported catalysts the situation is more complex, since the quantity of hydrogen that can adsorb on carbon is almost negligible and a percolation path between the catalyst particles does not exist unless extremely high platinum loadings are used. However, although hydrogen does adsorb poorly on carbon it may spill over from platinum to the carbon black, then diffuse over the surface of the carbon black and reversely spill over to another platinum particle [96,27]. On the cathode side spillover of oxygenated species is less likely to occur and requires significant oxidation of the carbon black surface [96].

In addition to spillover of hydrogen or oxygen containing species, platinum particles not in direct contact with the polymer electrolyte can be involved in the interfacial electrochemical reaction by the pathway of surface conductivity pro-

vided by condensed water and acidic groups on the carbon surface [106]. Since the surface chemistry of carbon is easily changed by potential cycling, surface conductivity is sensitive to electrochemical pretreatment or the potential range the cell is operated in [96].

The effect of polymer electrolyte fragments on the proton conductivity in PEFCs has also been discussed in literature [123,29]. However, it is questionable whether proton conduction by electrolyte fragments is of any significance to the proton transport in PEFCs, since degradation of the polymer electrolyte is slow and a measurable pH change was neither observed by McBreen et al. [106] as well as by Liu and coworkers [96] even after several hours of cycling.

Another possibility to provide proton conductivity in the absence of an electrolyte is the use of alternative support materials, that are both proton and electron conductive. A couple of oxides and phosphates exhibit modest proton conductivity in their hydrated form [83]. Although those materials are generally electronic insulators some of them can be made electron conductive as well by the use of appropriate dopants [120]. In particular titanium oxide has gained recent interest as a cathode catalyst support due to its high oxidation stability which may lead to improved long-term stability when compared to currently used carbon supports [120,35]. However, also organic materials like polyaniline are discussed in the scientific community as alternative catalyst support materials, because of their ability to conduct protons as well as electrons [128,117].

Part 3

Experimental

3. EXPERIMENTAL

In this chapter a short description of the experimental techniques, which were used throughout this work, is given. Deviations from the characterization or preparation procedures described herein, as they affect only individual samples, are described in the individual chapters.

3.1. MEA PREPARATION

Most MEA samples characterized during this work were obtained from the ZAE Bayern (Munich) as a part of a joint project. Some samples were also prepared at the TU Darmstadt following a similar preparation procedure as those obtained from the ZAE Bayern.

If not specified separately, MEAs characterized in this work were prepared by hot spraying of a catalyst ink onto a heated Nafion membrane. The catalyst ink, consisting of the catalyst dispersed in a mixture of water, isopropanol and Nafion solution (Aldrich), was sprayed on a heated (100°C) Nafion membrane, which had been boiled in 2 % H_2O_2 and 2 N H_2SO_4 for about 1 hour, respectively. After the coating of the membrane with the catalyst layer, the freshly prepared MEAs were exposed to a heat treatment for 45 min in a convection oven heated at 140 °C.

3.2. CHARACTERIZATION OF CATALYST SAMPLES

Catalyst samples characterized in this work were obtained from a project partner at Tsinghua University (Beijing). The catalysts were partially prepared during a 3 month collaboration visit at Tsinghua University. The catalyst synthesis procedures will be described in chapter 10 and 11 dealing with their characterization, while this section focusses on the experimental techniques used for their analysis.

3.2.1. GAS ADSORPTION (BET)

Specific surface areas of catalyst samples were measured by an N₂ absorber (Quantachrome, Autosorb - 3B) and calculated by the Brunauer-Emmet-Teller (BET) equation.

3.2.2. X-RAY PHOTOELECTRON SPECTROSCOPY (XPS)

To determine the oxidation state of platinum catalysts deposited on hydrous ruthenium oxide, X-ray photoelectron measurements were carried out under UHV using a multitechnique surface analysis system (Physical Electronics PHI 5700). Spectra were recorded with monochromatized Al K_α radiation on powder samples pressed onto indium foil. Core-level binding energies were determined using least squares fitting with asymmetrically modified Voigt functions. To limit the number of free parameters during the fit of the Ru 3d spectra, the intensity ratio of the Ru 3d^{5/2} and Ru 3d^{3/2} was set to their theoretical value and their energy separation was fixed at 4.2 eV.

3.2.3. X-RAY DIFFRACTION (XRD)

For the analysis of phase composition and average particle sizes powder diffraction patterns of the catalyst samples were recorded on a STOE STADI P powder diffractometer using either monochromatized Mo or Cu K_{α1} radiation. The measured diffraction patterns were refined by the Rietveld method using the FULLPROF software suite [136] to determine the cell constant and the average size of the deposited platinum particles.

In order to obtain the average particle size the diffraction patterns were fitted with the peak profile function 7 and a silicon standard was used to compensate for instrumental broadening of the reflex profile. The average particle size was then extracted from the fitting parameter according to the following equation:

$$d = \frac{360 \cdot \lambda}{\pi^2 \cdot Y} \quad (3.1)$$

where λ is the wavelength of the X-ray beam and d the particle size in Angstrom.

3.2.4. TRANSMISSION ELECTRON MICROSCOPY

During this work a Philips CM 20 and a Jeol JEM-3010 transmission electron microscope were used. Both microscopes were equipped with an LaB₆ cathode as electron source and were operated at the maximum specified operating voltage of 200 and 300 kV for the Philips and Jeol instrument, respectively. Characterization of catalyst samples was carried out with both instruments.

For the analysis of catalyst powder samples the catalyst was first dispersed in hexane or isopropanol and a small droplet of the dispersion was given on a TEM copper grid coated with a holey carbon film. The samples were subsequently dried in air for several minutes to keep contamination of the microscopes vacuum system low. In case of multi phase catalyst samples phase identification was affirmed by the evaluation of Fourier transformed high-resolution transmission electron micrographs. The Fourier transformation of the image data and the subsequent analysis of transformed images was carried out with the Gatan Software Digital Micrograph [43].

Since TEM has become a widely used method to determine particle sizes and size distributions of supported catalysts, particle size distributions are provided for the analyzed catalysts for convenience. Particle sizes were obtained from TEM bright field images by measuring the particle dimensions in an image analysis software. However, it should be noted that particle sizes determined by TEM may significantly differ from those determined by other methods such as XRD, for which data is also presented. A principal difference for the average particle sizes determined by TEM and XRD consists in the different weighting of the particle diameters. While XRD particle sizes are weighed by volume, TEM generally yields linearly weighed particles sizes, since the particle diameter is directly measured from the TEM images. Further, XRD particle sizes refer only to the crystalline part of the particle, whereas in the TEM particles composed of several crystals may be treated as a single particle and amorphous particle boundaries may be included, too. In addition, measurement errors are introduced by the imaging conditions in the microscope. In an early study of the matter Flynn et al. pointed out that due to an extension of the sample along the optical axis of the microscope catalyst particles may be imaged with various defocus values leading to variations of the apparent particle size of up to 1 nm [39].

A recent review by Pyrz and Buttrey on particle size determination by TEM also addressed the influence of different magnification settings and imaging modes as well as of the influence of the microscopist, who may preferentially select certain particle types over another [127].

3.3. CHARACTERIZATION OF MEA SAMPLES

For the characterization of MEA samples both scanning and transmission electron microscopy were used. SEM was generally used to obtain general surveys at lower magnification and to check for catalyst inhomogeneities.

MEA samples for TEM as well as for SEM were prepared by ultra-microtomy. While in contrast to TEM ultra-microtomed samples are not strictly necessary for SEM analysis, they provide a number of benefits over conventional bulk cross-sections, which are generally used for SEM analysis.

3.3.1. ULTRA-MICROTOMY

Microtomy is frequently used in biology and polymer science to prepare samples for microscopy. However, in materials science this method is less established for which reason a slightly more detailed introduction into this topic is provided.

The use of ultra-microtomy for the preparation of PEFC MEA samples for TEM was first proposed by Blom et al. [12], since other TEM sample preparation techniques like polishing or etching fail for PEFC electrodes due to their high porosity and the largely different hardnesses of the compounds.

In general the preparation of thin-sections by ultra-microtomy consists of three processing steps:

- Embedding of the sample in epoxy resin.
- Trimming of the embedded sample.
- Sectioning of the sample.

Embedding

As a consequence of the highly porous structure of the electrode layer, MEA samples need to be embedded in an epoxy resin to stabilize the electrode against the cutting forces of the sectioning process.

To embed an MEA sample, a thin stripe was removed from the MEA with a razor blade as illustrated in Figure 3.1. This stripe was fixed in a small rubber sink. The samples were then stored overnight in a desiccator to remove moisture, which could cause incomplete polymerization of the epoxy resin. The rubber sink was then filled with embedding resin (Araldite 502, SPI Supplies Inc.). The resin was prepared using the standard formulation of resin, hardener and accelerator supplied by the manufacturer. Finally, the sample was placed into a convection oven at 60 °C for at least 16 hours to cure the resin.

Trimming

To reduce the cutting forces during the sectioning process, the sectioned sample area should be as small as possible. Therefore, the tip of the resin block, in which the sample is embedded, is trimmed down to a trapezoidal shape with lateral dimensions of less than 1 mm, as shown in Figure 3.2. The trapezoidal shape of the tip also aids to further reduce cutting forces when the knife cuts through the sample from the broader to the narrower end of the trapeze.

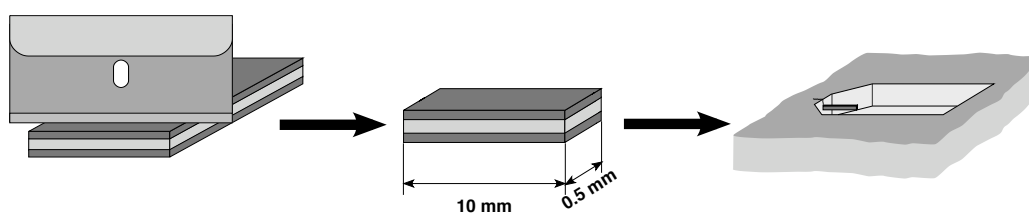


Figure 3.1. *Illustration of the sample embedding process.*

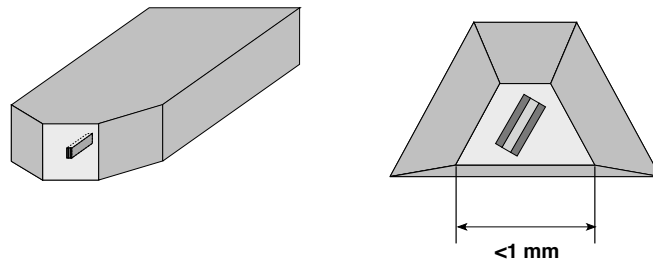


Figure 3.2. Embedded MEA sample before (left) and enlarged view of the tip after the trimming process.

For continuous section bands the lower and upper base of the trapeze should be mostly parallel, as the section bands will otherwise start to bend (Figure 3.3 a & b), which may lead to specimen overlap.

To obtain high quality sections, precise positioning of the MEA sample within the tip is necessary. The MEA should be positioned forming an angle of 30 - 45° with the base of the trapeze to reduce forces perpendicular to the membrane-electrode interfaces. Furthermore, care must be taken not to completely remove the embedding resin at one side of the tip, as this may lead to fracture of the MEA sample or even a complete loss, as shown in Figure 3.3 c).

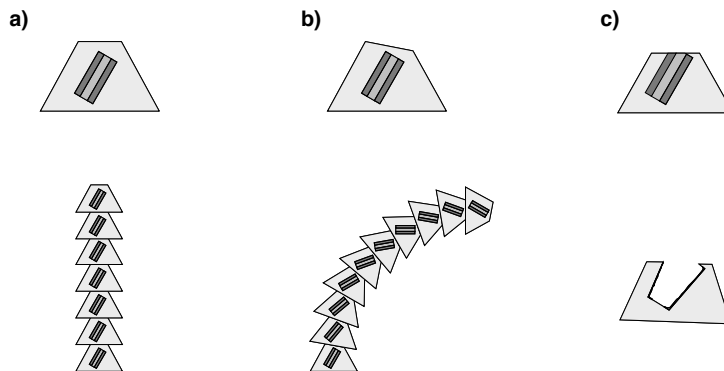


Figure 3.3. Illustration of the effect of different tip shapes on the section quality. The tip shape is shown in the top part of the image and the effect on the microtomed thin-sections is displayed below. (a) Perfectly trimmed sample with parallel edges, (b) sample with anti-parallel top and bottom edges and (c) sample, of which too much of the embedding resin has been removed.

Sectioning

Sectioning of the embedded samples was carried out with a Reichert-Jung ultracut microtome at room temperature using a DiATOME diamond knife equipped with a 4 mm diamond blade polished at an angle of 45°. During the sectioning process the embedded sample is moved relative to the diamond knife and the cut sections float on a water trough as shown in Figure 3.4.

The cut sections were transferred to TEM copper grids and dried at room temperature for at least 48 hours. Sections of 200-500 nm thickness and ultra-thin sections of 70-100 nm were prepared for SEM and TEM microscopy, respectively.

3.3.2. SCANNING ELECTRON MICROSCOPY

SEM can be carried out either on bulk samples or thin-sections. Cross-sections of bulk samples are commonly obtained by freeze-breaking or cutting MEAs [5,94,119,202]. Although these processes are rather convenient and have been used by a number of researchers, bulk cross-sections obtained in this way have a number of limitations. Since the electrode structure is rather fragile, breaking or cutting of the sample will create a fracture surface rather than a smooth cut through the sample. This significantly hampers interpretation of the surface

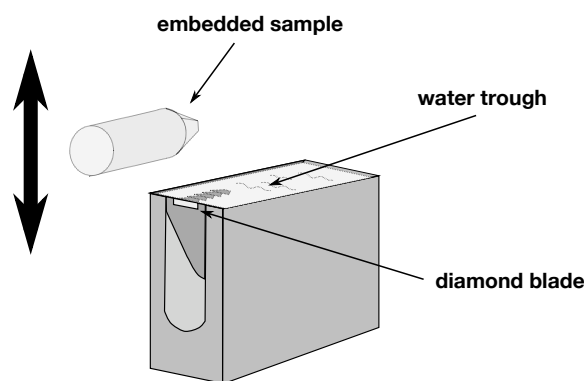


Figure 3.4. Illustration of the sectioning process. The sample is moved relative to the diamond knife. Cut sections float on a water trough behind the blade.

morphology. The mechanical forces applied during breaking or cutting of the sample may even damage the electrode structure. In addition, the electron beam can penetrate deeply into the sample due to the low density of the carbon support material and the high porosity of the electrode [130], limiting the obtainable resolution for Z-contrast (BSE) or element resolved (X-ray) imaging significantly.

Both issues are significantly reduced, if MEA thin-sections are used instead of bulk cross-sections. Due to the low thickness of the thin-sections and their superior surface quality, pores in the catalyst layer can be easily identified, if their diameter exceeds the specimen thickness. Furthermore, the specimen thickness limits the excitation volume for BSE and X-ray detection, which improves lateral resolution.

As a consequence, electrode thin-sections were used instead of bulk cross-sections for characterization in the SEM. Analysis was carried out using a FEI Quanta 200 FEG environmental scanning electron microscope and a ZEISS DSM 962. Both instruments were equipped with an energy dispersive X-ray detector for elemental analysis and mapping. To minimize interaction of the electron beam with the sample holder a special holder was used. The holder was designed to sustain the TEM copper grids, used to carry the sections, only on their outer rim, so that the electron beam can penetrate the sample (Figure 3.5).

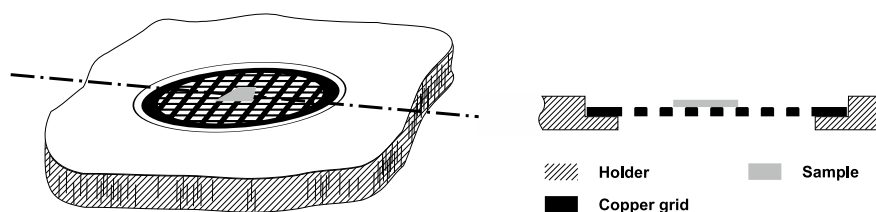


Figure 3.5. Schematic drawing of the sample holder used SEM analysis of MEA thin-sections.

3.3.3. TRANSMISSION ELECTRON MICROSCOPY

This section briefly describes the methods and instruments used for TEM characterization, whereas the image acquisition and processing procedures as well as extensions and modifications made to them are outlined in more detail in the next chapter.

Transmission electron microscopy was used for a more detailed characterization of the specimens, resolving finer details of the electrode structure such as individual catalyst or support particles. In addition to classical bright field TEM energy filtered transmission electron microscopy (EF-TEM) was deployed to obtain element distribution images of the electrodes.

EF-TEM makes use of characteristic energy loss features of the electrons transmitted through the specimen in a transmission electron microscope. The transmitted electrons may suffer elastic as well as inelastic scattering events. Elastically scattered electrons, which do not transfer energy to the sample, constitute the major part of electrons transmitted through the sample. However, some electrons interact inelastically with the sample transferring energy to phonons, plasmons or core-level electrons. These processes lead to characteristic energy loss features in the electron energy loss spectrum and may be used to obtain additional information on the specimen composition and local bond structure of the specimen.

All TEM analyses of fuel cell electrodes were carried out with a Jeol JEM-3010 transmission electron microscope. The microscope was equipped with an LaB₆ cathode as electron source and operated at an operating voltage of 300 kV to reduce beam damage of the sample. For energy filtered imaging the microscope was equipped with a Gatan Imaging Filter (GIF) attached to the microscope column after the imaging system. The energy filter could be operated in imaging mode to obtain energy filtered images (EF-TEM) or in spectroscopy mode to record electron energy loss spectra (EELS).

4. TEM IMAGE ACQUISITION

For the analysis of ultra-thin cross-sections of PEFC electrodes TEM is superior in many aspects to other microscopical techniques such as SEM, AFM or light microscopy. This is not only owed to the high resolutions available by TEM but also to the differences in image formation. Both AFM and SEM derive most of their contrast information from variations in the surface roughness/morphology of the sample. As the thin sections prepared by ultra-microtomy are ideally smooth and of homogeneous thickness, information that can be obtained by AFM or SEM is limited. In contrast, TEM produces a 2D projection of the sample and can therefore also image features of the sample not located directly at the sample surface.

However, while TEM has a clear benefit regarding contrast formation, the rather limited sample areas that can be covered by this technique must be considered as the major drawback of this technique for the characterization of PEFC electrodes.

The poorly defined long range order of standard PEFC electrodes requires large sample areas to be covered to obtain statistically representative information about their structure. Furthermore, PEFC electrodes often contain features like catalyst agglomerates or pores that can easily exceed sizes of 1 μm and the thickness of the electrode is often in the range of about 10 - 100 μm .

Although most TEMs also offer low magnification modes, these modes are most often of limited use for sample characterization as the field of view in these modes is limited by the electron optics or aperture settings. For weakly scattering samples such as polymers or various carbon materials, which comprise the main part of PEFC electrodes, small contrast forming apertures need to be used to observe sufficient contrast in the final image.

For the Jeol 3010, which was used for most of the sample characterizations, the lowest usable magnifications were limited to 15-25 kx when operated at 300 kV depending on the selected contrast forming aperture. Using photographic slides of 8 x 10 cm in size, which corresponds to about 7.5 x 9 cm of imageable area, a sample area of about 5 x 6 μm can be covered at 15 kx with a single shot. This

demonstrates that even at low TEM magnifications the imageable area is not sufficient to cover statistically representative sample areas.

Another issue for the characterization of MEAs by transmission electron microscopy comes from the sample preparation process of the ultra-thin sections. Due to intrusion of the embedding resin into the pore structure and spatial overlap of the polymer electrolyte phase with the catalyst, identification of the polymer electrolyte is not possible in all situations by classical transmission electron microscopy. In these cases energy filtered transmission electron microscopy (EF-TEM) was used to obtain additional information about the electrode structure and support identification of the polymer electrolyte.

However, the issue of limited imageable sample area becomes even more problematic for the acquisition of energy filtered images using the Gatan Imaging Filter. The energy filter (see Figure 4.1) is attached to the bottom of the microscope column after the projector system. Due to the increased distance of the CCD camera from the projector lens crossover, the image that is formed on the CCD is post-magnified by about 19 times. Furthermore, the size of the CCD-chip is significantly smaller than the size of a photographic slide (about 25x25 mm), causing an additional decrease of the imageable area.

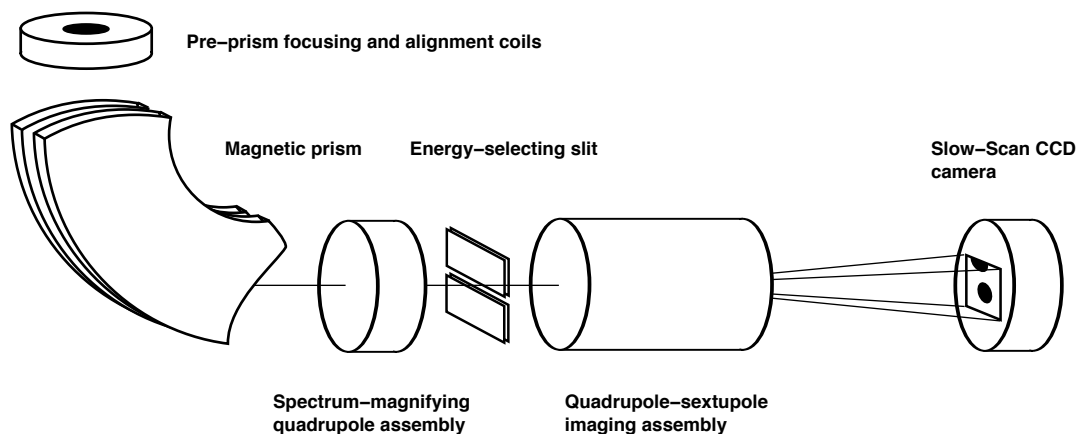


Figure 4.1. Schematic drawing of the Gatan Imaging Filter attached to the Jeol 3010, that was used during this work to acquire energy filtered TEM images.

To extend the imageable areas two different approaches were chosen depending on the TEM imaging mode:

- For acquisition of TEM images on photographic slides the sample was manually shifted to record a sequence of overlapping images, which were then assembled to a single image spanning a larger sample area with the aid of a standard image processing software (Gimp [45]).
- For the acquisition of energy filtered images a different shifting procedure was chosen. Due to the high post-magnification of the energy filter, manual positioning of the sample using the goniometer controls is not precise enough to obtain overlapping images that can be post-processed into a larger image. Instead, image and beam deflector coils of the microscope were used to electronically shift the image formed on the CCD.

While in principle the second approach is almost as simple as the first approach for photographic slides, significant technical problems, mainly associated with the stability of the polymer electrolyte in the electron beam, led to the development of a set of comprehensive software routines written in Digital Micrograph Script to record a set of energy filtered images.

The following chapter describes in more detail the principal considerations that led to the development of the image acquisition routines for energy filtered images, as well as the routines employed for acquisition and post-processing of the images.

4.1. BEAM DAMAGE OF THE SPECIMEN

The information obtained by energy filtered images or electron energy loss spectroscopy (EELS) derives from inelastic scattering processes of the electrons of the primary beam with the electrons of the sample. While inelastic scattering processes provide useful information about the chemical composition of the sample, inelastic scattering also has an undesirable side-effect. The energy transferred to the sample by inelastic scattering events may cause severe damage of the sample. Three different forms of beam damage can occur when a sample is exposed to a high energy electron beam in a TEM or SEM microscope [188].

- Radiolysis. Inelastic scattering often causes ionization of the interacting atom and therefore leads to cleavage of chemical bonds.
- Knock-on damage. The incident electron causes a direct displacement of atoms creating point defects in crystalline samples.
- Thermal heating of the sample by phonons or lattice vibrations generated by electron-electron interactions.

The latter is generally the most dominant degradation process of polymers, as the thermal stability of these materials is rather limited and specimen heating in the electron beam can be significant. Experimental analysis of beam damage in various polymers shows a clear dependence of the beam stability on the thermal stability, i.e. melt temperature of the polymer [84]. However, it is also well known that fluoropolymers such as PTFE exhibit a rather high beam sensitivity despite their otherwise high chemical and thermal stability [142]. In these polymers radiolysis of the C-F bond contributes significantly to the degradation of the polymer chains.

As PFSI polymer electrolytes commonly used in PEFCs belong to the class of fluoropolymers, radiolysis and rapid loss of fluorine can be expected to be a major obstacle for the characterization of the electrode structure and the polymer electrolyte distribution in particular. In fact, a low stability of PFSI polymers in the electron beam [125] or towards ionizing radiation [144,145] has been reported by several authors. In addition to the low stability of the fluorine bond, the sulfonate groups of the side chains in PFSI polymers also rapidly degrade when exposed to ionizing radiation [144].

Common methods to reduce degradation of polymer materials in the TEM are working at low electron doses and the use of high accelerating voltages. The latter reduces the beam damage by decreasing the scattering cross-section of the specimen, which leads to a lower energy deposition in the sample. For polymer materials suffering mostly from thermal heating, cryomicroscopy can significantly increase the stability of the specimen in the electron beam. However, polymers that undergo scission of bonds are mostly unaffected as cooling only reduces damage caused by thermal heating of the specimen [142].

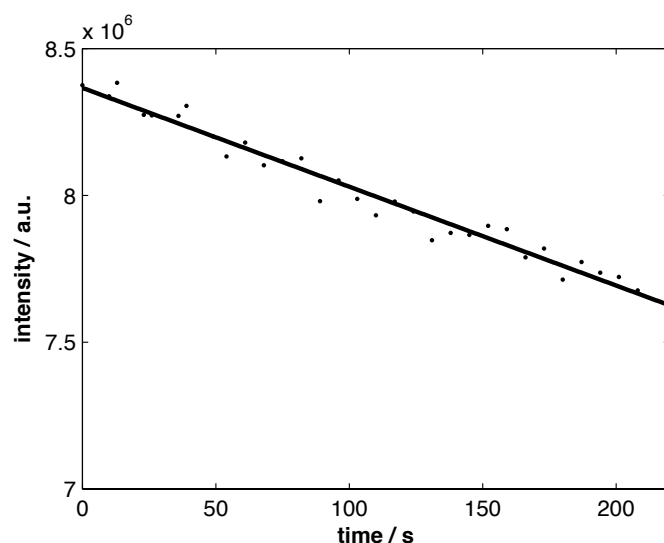


Figure 4.2. *Dependence of the fluorine signal intensity on the acquisition time. Measured data (dots), linear fit (solid line). The signal shows an almost linear decay corresponding to a loss rate of about 2.5 % per minute.*

As scission of bonds (radiolysis) is the main damaging effect for fluoropolymers, the effect of cryomicroscopy on the stability of the PFSI is small. For the acquisition of energy filtered images low-dose microscopy is also not a viable option. The intensity of the electron beam falls rapidly off at higher loss energies, therefore high primary beam intensities and long recording times - up to 1 min or more - are often required in energy filtered imaging mode. Since degradation of the polymer electrolyte during acquisition cannot be avoided, it is necessary to know at which rate the loss of fluorine occurs in the polymer electrolyte. Therefore, a part of a Nafion membrane was irradiated with a beam intensity similar to that used for the acquisition of energy filtered images and several snapshots of the fluorine edge were taken over a period of about 4 minutes. The intensity of the fluorine signal was then determined by integrating the energy interval of the fluorine edge and subtracting the background intensity obtained from a power-law fit to the pre-edge region. Figure 4.2 shows the computed fluorine signal intensities in dependence on the acquisition time.

The fluorine signal showed an almost linear decay corresponding to a loss rate of about 2.5 % per minute. While this loss rate is significant, it is low enough to in

principle allow the acquisition of quantifiable energy filtered images of the fluorine edge, if care is taken not to damage the polymer electrolyte prior to acquisition.

4.2. SPECIMEN DRIFT

Another obstacle for the precise determination of element distributions from energy filtered images is specimen drift. The main intensity contribution in energy filtered images generally arises from non-characteristic inelastic scattering such as phonon scattering or multiple scattering events. Therefore, the characteristic loss feature is superimposed on a background intensity, which needs to be subtracted from the image in order to obtain information about the element distribution. Commonly two different methods are applied for background correction of energy filtered images. The two-window method uses one pre-edge image acquired at electron losses just below the edge-energy of the element for background correction. The pre-edge image is supposed to contain only non-characteristic scattering information and the element map is computed either as the difference of the two images or their ratio, the latter is also referred to as jump-ratio imaging. However, the two-window method only provides quantitative element information for very thin specimens. For thicker specimens, where multiple scattering occurs, only a qualitative indication of the element distribution is obtained [62]. In the case of thicker specimens more reliable information can be obtained by the three-window method. The three window method uses two pre-edge images for background correction (see section 4.7.2 for more information). No matter which method is applied, the use of one or more images for background correction requires that all images are perfectly aligned relative to each other, as the background intensity may deviate strongly within the image and misalignment will cause quantification errors.

Unfortunately the specimen position in the microscope is often not as stable as would be desirable for the acquisition of energy filtered images. Specimen drift is either due to the microscope itself (drift of the holder) or the sample. Sample drift is most often due to charging. However, degradation of the sample or parts of the sample, as it is the case for the polymer electrolyte, can introduce an addi-

tional drift. This drift originates from slight distortions of the sample in the electron beam. While these distortions are generally small enough to be tolerated for conventional TEM micrographs, energy filtered imaging is rather sensitive to these distortions, since even small displacements can cause quantification errors in the element maps. Furthermore, the long exposure times necessary to record the energy filtered images can already cause a smearing of the image intensities during acquisition. It is therefore essential to compensate for specimen drift in the post-processing of the energy filtered images as well as during acquisition.

4.3. REQUIREMENTS FOR THE IMAGE ACQUISITION PROCEDURE

The above considerations concerning the stability of the sample and specimen drift impose the following requirements to the image acquisition procedure:

- a) Experiments should be carried out at the highest possible acceleration voltage (300 kV), as this reduces beam damage and multiple scattering.
- b) The time necessary to record a single image should be minimized as far as possible, as this reduces beam damage as well as specimen drift during acquisition.
- c) Acquisition of the images at different filter energies and the switching between individual sub-images should be as fast as possible to reduce the total electron dose the specimen is exposed to.
- d) The sequence of energy filtered images should be chosen so that the fluorine post-edge image is acquired before recording the pre-edge images since the damage of the polymer electrolyte is lowest at the beginning of the acquisition process.
- e) Measurement of the sample drift as well as active drift compensation during image acquisition should be supported to reduce the mismatch between corresponding images and allow proper alignment for post-processing of the images.

Point a) should not need any further explanation as this just requires setting the microscope to its maximum acceleration voltage. The exposure time b) necessary to record an energy filtered image mainly depends on the intensity of the signal and noise from the detector. While a high beam intensity generally improves the signal quality, it also leads to more rapid degradation of the specimen. However, the more rapid degradation is at least partially compensated by the shorter exposure times. Furthermore, short exposure times significantly reduce problems associated with specimen drift during acquisition. Therefore, a high primary beam intensity was intended for the measurements, despite its negative influence on the specimen degradation.

The acquisition speed c) plays an important role in minimizing sample degradation. The operator is generally the largest bottle neck when referred to acquisition speed. Changing the filter setting and repositioning the sample manually takes significantly more time as if the same process is realized by a software control. Another circumstance, which makes a manual approach rather unrealistic, is the sheer amount of data that needs to be collected for a series of energy filtered images. At least three images are necessary to obtain an element map (2 pre-edge and one post-edge images) of a single subimage. This number can easily increase, if each image is recorded more than once, to compute an averaged sum for the purpose of noise reduction and drift compensation. For instance, acquisition of a 3 x 3 series of energy filtered images for a single element requires a total of 27 images, which scales up to 81 images, if each image is recorded three times to reduce noise in the final image. Adding unfiltered images of the same sample area as well as plasmon or zero-loss filtered images increase the number of acquired images even further.

The sequence d), in which the energy filtered images are acquired, is also essential to obtain a high fluorine signal. As the fluorine loss from the sample proceeds during the whole acquisition period, the images of the fluorine loss feature should be recorded in first place, when fluorine loss is still lowest. However, it should be noted that the sample has undergone minor compositional changes due to the fluorine loss, when the pre-edge images are recorded. This may lead to a slight underestimation of the background signal for sample areas with high fluorine losses. While this circumstance can even improve the sensitivity of the

method for fluorine detection, determination of the fluorine content may no longer be truly quantitative.

Drift control e) is essential to both acquisition and post-processing of the images. Since the underlying procedures for drift measurement and drift correction are slightly more complex, they will be discussed in more detail in the following section.

4.4. IMAGE POSITIONING AND DRIFT CORRECTION

Shifting of the imaged sample area as well as active drift correction requires precise means to translate the sample or its image formed on the camera. Physically shifting of the specimen would be the preferred way to realize this, as this leaves the beam path in the microscope unchanged and hence assures identical imaging conditions for all acquired images. However, as already mentioned in the introductory part, positioning of the sample by the goniometer controls was found to be too slow and not precise enough to assure accurate positioning of the specimen even at the lowest magnification settings available for the GIF.

Another way to shift the imaged sample area in the TEM is to use the microscope's image deflector coils to electronically shift the image formed on the camera or viewing screen. Since the image deflector coils are designed to obtain small shifts even under high resolution conditions, it offers a more precise way to position the imaged sample area. However, the image deflector coils only cause a virtual shift of the sample by changing the beam path of the projector lens system, but leave the specimen area illuminated by the electron beam unchanged (see Figure 4.3 B). Therefore, at large image shifts the illuminated sample area will lie outside the imaged region of the sample. To avoid this, the beam needs either to be strongly defocused to illuminate a much larger sample area, as would be necessary to record a single image, or the beam must track the change of the imaged sample area. The latter can be achieved by combining the image shift with a beam shift as shown in Figure 4.3 D. This solution is far more complex to realize than simply expanding the electron beam, as it requires careful synchronization of both deflector systems. However, this method was preferred, because

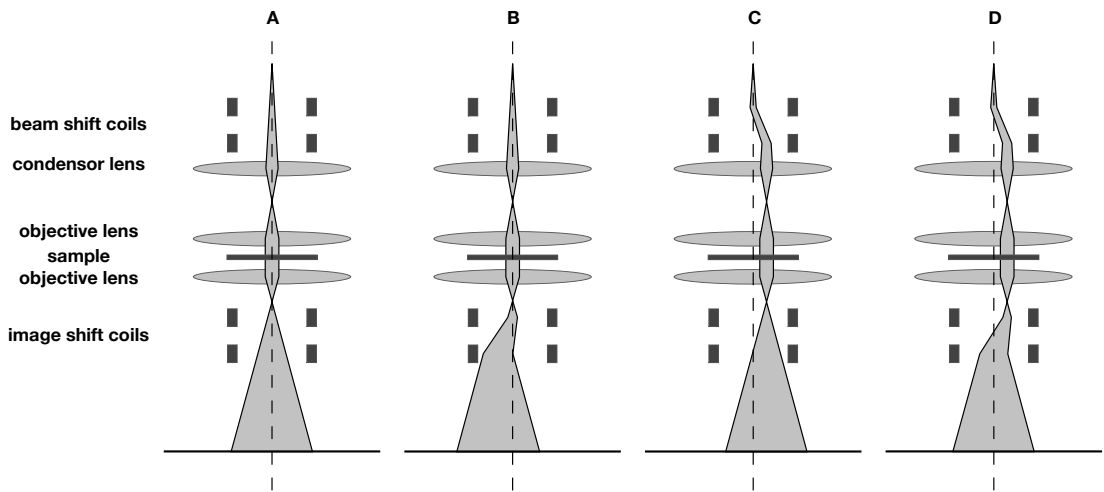


Figure 4.3. Ray diagram illustrating the function of the image and beam deflector coils in the TEM (intermediate and projector lenses have been omitted). A: All deflector coils turned off. Electrons follow a straight path along the optical axis. B: Only the image deflector coils turned on. The image of the sample is shifted relative to the camera or viewing screen. C: Only beam deflector coils turned on. The area of the sample illuminated by the electron beam is shifted to a different position, as well as the image of the beam on the viewing screen. D: Combined image and beam shift. The beam shift compensates the move of the illuminated area on the viewing screen caused by the image shift.

expansion of the electron beam would have resulted in a significantly reduced beam intensity, which is undesirable for energy filtered imaging, as pointed out previously. Furthermore, an expanded beam would have led to augmented degradation of sample areas, since the whole sample area would have been exposed permanently to the electron beam, although only imaged eventually.

While the lateral mismatch between different energy filtered images for a single image due to specimen drift is usually small enough to be compensated by the post-processing routines, the long acquisition time necessary to record a complete series of shifted images generally causes much larger mismatches, which in extreme cases may even lead to images no longer sharing any common overlap. To avoid large mismatches between images of the same sample area the same method, which was also used to shift the imaged sample area, was applied. For

this purpose the specimen drift was determined from an unfiltered image (see next section: Measurement of Image Drifts) and an appropriate beam and image shift was chosen to realign the imaged region on the camera. Measurements of the image displacement directly after the drift correction generally resulted in image drifts of less than 3 pixel at a magnification of about 80 kx corresponding to an accuracy of about 1 nm. This nicely demonstrates the high accuracy that can be obtained by this positioning method, if the deflector values are well calibrated.

4.5. MEASUREMENT OF IMAGE DRIFTS

As previously mentioned, proper drift correction is essential for the evaluation and acquisition of energy filtered images. However, in order to apply a drift correction during acquisition or within the image post-processing routines the image drift needs to be precisely known.

In image analysis cross-correlation is a common method to locate objects in images but it can also easily be used to determine image displacements. Cross-correlation is a statistical technique to determine the similarity of two signals. It is frequently used in signal-processing to determine the phase-shift of two signals. However, the concept of cross-correlation can easily be extended to multi-dimensional data like images.

In general the cross-correlation function determines the similarity (correlation) of two signals in dependence of a shift parameter to determine the shift between two signals or the location of a pattern or mask $w(x,y)$ within an image $f(x,y)$. Computation of the cross-correlation function in real space is numerically intensive unless the mask w is very small. Therefore, the cross-correlation theorem

$$f(x, y) \circ w(x, y) \Leftrightarrow F(u, v) \cdot H^*(u, v) \quad (4.1)$$

is generally used for computation of the cross-correlation function [49]. It states that the spatial correlation $f(x,y) \circ w(x,y)$ can be obtained as the back transform of the product of the Fourier transform $F(u,v)$ of one function times the

conjugate of the transform $H^*(u, v)$ of the other. The cross-correlation function has its maximum where the mismatch between the two functions is minimized.

Therefore, the image drift can be obtained by determining the maximum of the cross-correlation function of the drifted image of the sample with a reference image. For images with sharp image features and high contrasts the cross-correlation function has a sharp maximum and determination of the image drift will be quite accurate. However, for images having only diffuse image details or slowly changing contrast gradients cross-correlation may eventually fail. Hence, it is essential to choose an appropriate reference image with high image contrasts for proper drift correction. Although, in principle, image drifts can also be obtained directly from energy filtered images, these images often do not provide high contrasts and sharp image details. In contrast, unfiltered or zero-loss filtered images generally provide much higher contrasts and sharper image details so that image drifts can be determined more accurately. Therefore, it was chosen to determine the drift information from unfiltered images of the sample, although this requires the acquisition of an additional unfiltered image for each energy filtered image and hence prolongs the total acquisition time. However, since exposure times necessary to acquire an unfiltered image are comparatively short - about 0.2 seconds compared to about 10 - 60 seconds for an energy filtered image - additional beam damage of the sample due to the drift measurement is rather low.

4.6. RECORDING PROCEDURE

The acquisition procedure starts with recording a set of unfiltered images from the region of interest. These unfiltered images are used as references for the drift measurement routine and serve also for the reconstruction of a classical unfiltered TEM image of the sample.

In a second step the energy filtered images are recorded in the sequence defined in the input file of the image acquisition routine. Before each acquisition of an energy filtered image an unfiltered image is recorded to determine the sample drift. If the sample drift exceeds a certain value, which can be defined by a pa-

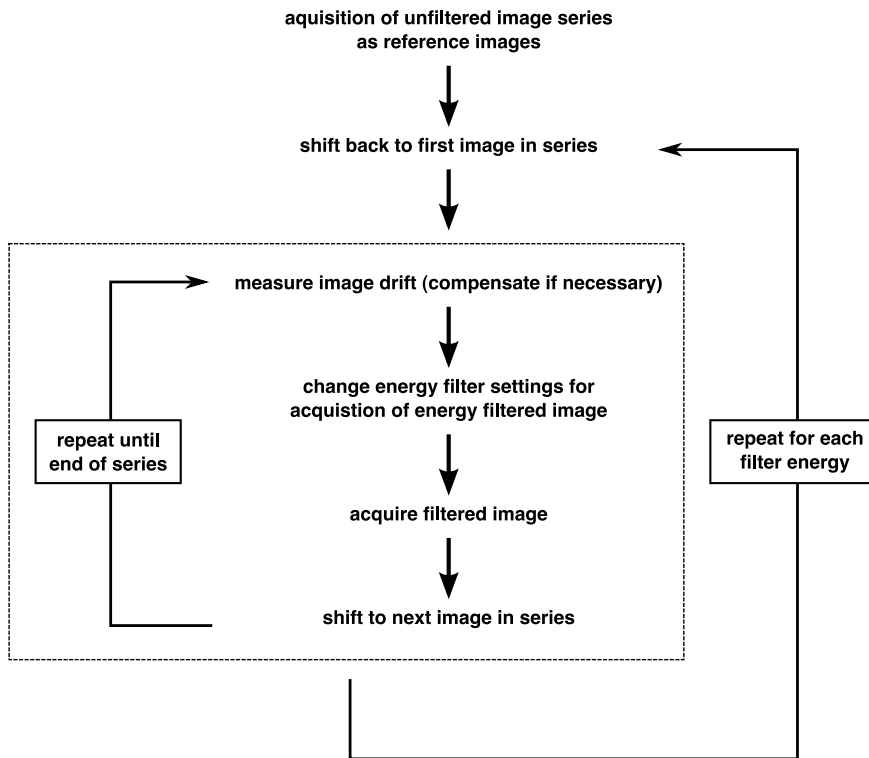


Figure 4.4. Flow-diagram of the image acquisition procedure.

parameter in the input file, a drift compensation is carried out to realign the imaged sample area with the reference image.

The program supports the acquisition of images at an arbitrary number of filter energies. For each of the filtered images the filter energy, slit width, exposure time and hardware binning can be chosen individually. The sequence, in which the energy filtered images are recorded is determined by the order in which they are specified in the input file of the program and therefore is freely configurable by the operator.

4.7. PROCESSING OF ENERGY FILTERED IMAGES

After acquisition, the images need to be post-processed to obtain element distribution images and to align the individual images taken at a certain sample position.

The post-processing procedure consists of the following steps:

- Averaging of the image data acquired at the same filter energy to reduce noise.
- Calculation of the background intensity from the acquired pre-edge images and computation of the final element map.
- Alignment of the images according to their relative positions.

4.7.I. AVERAGING OF IMAGE DATA FOR NOISE REDUCTION

Since the sample drift can only be determined at the beginning of the acquisition process for each energy filtered image, realtime drift correction during image recording is not possible. Hence, the only way to avoid smearing of image intensities due to sample drift is to lower the exposure time for the energy filtered image. However, shorter exposure times increase the signal noise, which will result in a higher detection threshold for the investigated element.

To improve the signal intensity even at low exposure times, multiple exposures were taken at the same filter energy. The images were then averaged using the drift information determined between each exposure. To further increase the signal-to-noise ratio, energy filtered images were generally recorded with a hardware binning of 2. While this reduces the lateral image resolution by a factor of 2 it improves signal intensity by a factor of 4, because 2×2 pixels are treated as a single physical pixel.

Since the drift values are determined from the unfiltered images, which are taken at full camera resolution, the energy filtered images are linearly scaled to full resolution in order to obtain most accurate drift alignment. Figure 4.5 demon-

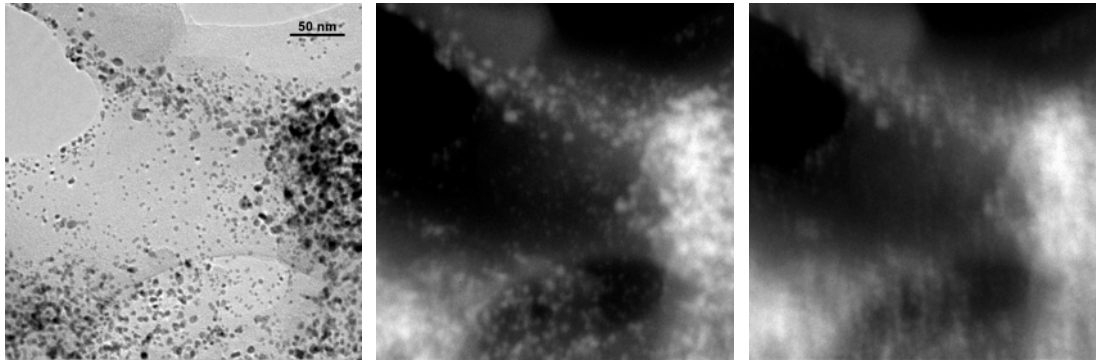


Figure 4.5. Sub-image of a 3×3 image array acquired at different filter energies from an electrode containing 60 vol.% Nafion. Unfiltered image (left), average of three energy filtered images taken at the same filter energy (690 eV, slit width 25 eV) with drift correction (center) and without drift correction (right).

strates this for an image of a PEFC electrode recorded with the image shifting routine. The drift corrected average clearly preserves the image details from the unfiltered image, while the averaged image without drift correction appears significantly blurred due to the sample drift.

4.7.2. BACKGROUND CORRECTION

To obtain elemental information from energy filtered images a background correction needs to be applied to the energy filtered images recorded at the edge energy of the element of interest. The background intensity arises from multiple inelastic scattering of the electrons from the electron beam with electrons of the sample. It varies with sample thickness and the scattering cross-section of the elements in the sample. Therefore, the background intensity is generally not uniform for the whole image and background correction must be carried out individually for each data point of the image.

In general the background intensity can be described well by a power law decay:

$$J(E) = A \cdot E^{-r} \quad (4.2)$$

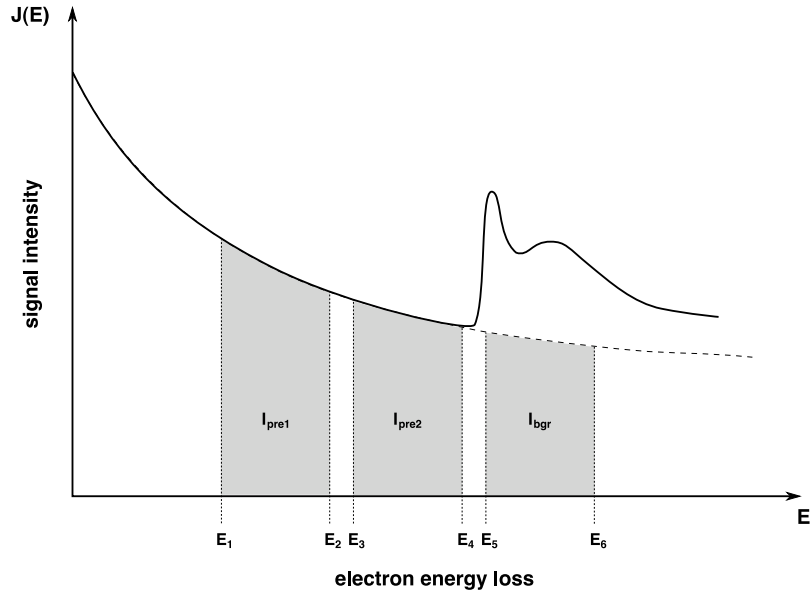


Figure 4.6. Schematic drawing of an EELS spectrum illustrating the placement of filter energies for the background correction of energy filtered images by the three-window method.

To determine the power law coefficients A and r two images are acquired at loss energies just below the edge energy of the element. Since each image is not recorded by a single energy but over an energy range defined by the energy selecting slit and the energy offset of the spectrometer, the image intensity of the two pre-edge images is given as the integral of equation 4.2 over the respective energy range.

$$\int J(E)dE = \frac{A}{1-r} E^{1-r} \quad (4.3)$$

From this equation it follows for the intensity ratio of the two pre-edge images:

$$\frac{I_{pre1}}{I_{pre2}} = \frac{[E_2^{(1-r)} - E_1^{(1-r)}]}{[E_4^{(1-r)} - E_3^{(1-r)}]} \quad (4.4)$$

Since this equation cannot be solved for r in a closed form the pre-edge intensities are usually approximated by their geometric averages

$$I_{pre1} \cong (E_2 - E_1) \cdot [J(E_1) \cdot J(E_2)]^{1/2} \quad (4.5)$$

and likewise for the second pre-edge image.

Their intensity ratio can then be expressed as

$$\frac{I_{pre1}}{I_{pre2}} \approx \frac{E_2 - E_1}{E_4 - E_3} \cdot \left[\frac{E_1 \cdot E_2}{E_3 \cdot E_4} \right]^{-r/2} \quad (4.6)$$

From this equation r can be derived as

$$r \cong -2 \cdot \frac{\ln \left(\frac{I_{pre1} \cdot (E_4 - E_3)}{I_{pre2} \cdot (E_2 - E_1)} \right)}{\ln \left(\frac{E_1 \cdot E_2}{E_3 \cdot E_4} \right)} \quad (4.7)$$

The power law coefficient A may then be obtained by one of the following equations

$$A = \frac{1 - r}{E_4^{(1-r)} - E_1^{(1-r)}} (I_{pre1} + I_{pre2}) \quad (4.8)$$

$$A = \frac{1 - r}{E_4^{(1-r)} - E_3^{(1-r)}} I_{pre2} \quad (4.9)$$

The latter generally results in a more accurate determination of the post-edge background intensity, as it gives more weight to the image intensities of the pre-edge image close to the edge. Once having calculated A and r the post-edge background intensity can be obtained by solving equation 4.3 for the respective energy interval.

Figure 4.7 shows the resulting fluorine map of the same sample area as displayed in Figure 4.5. Again the computed fluorine map is shown with and without the

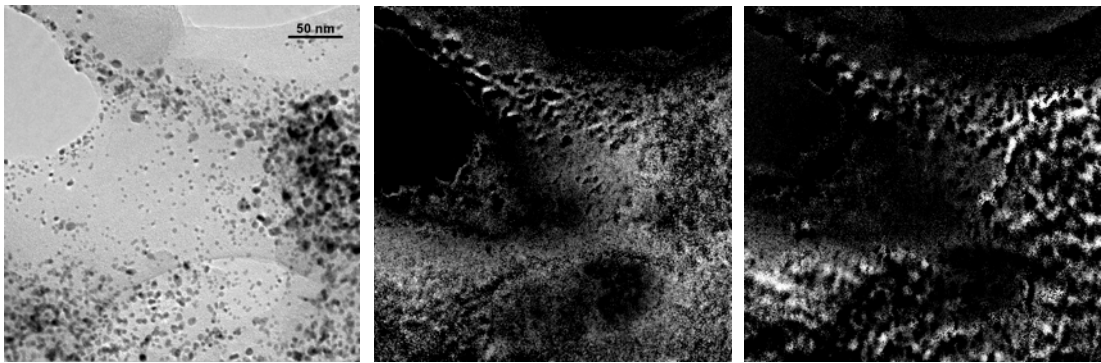


Figure 4.7. Sub-image of a 3×3 image array acquired at different filter energies from an electrode containing 60 vol.% Nafion. Unfiltered image (left), background corrected images for the fluorine edge with drift correction (center) and without drift correction (right).

use of drift correction. In the fluorine map without drift correction clearly artifacts due to a mismatch between the pre- and post-edge images can be seen. The drift corrected image is almost free of artifacts. Only in the upper left part of the image slight artifacts are visible which are most probably due to distortions of the sample during acquisition, which cannot be fully compensated by the drift correction.

4.7.3. AUTOMATIC IMAGE RECONSTRUCTION

In a last step the individual images obtained from one sample region need to be aligned to form a single image with an extended field of view. The image alignment procedure again uses cross-correlation of the overlapping image regions to determine the exact relative positions of the sub-images. The images are then automatically aligned according to their relative positions. Figure 4.8 shows a 3×3 image array acquired with the image shifting routine and the result of the alignment procedure. The final image significantly extends the field of view when compared to a single image, therefore allowing larger features of the electrode structure to be characterized. The program has been tested with image arrays up to 4×4 in size. No severe implications concerning image quality were found even at such large image shifts.

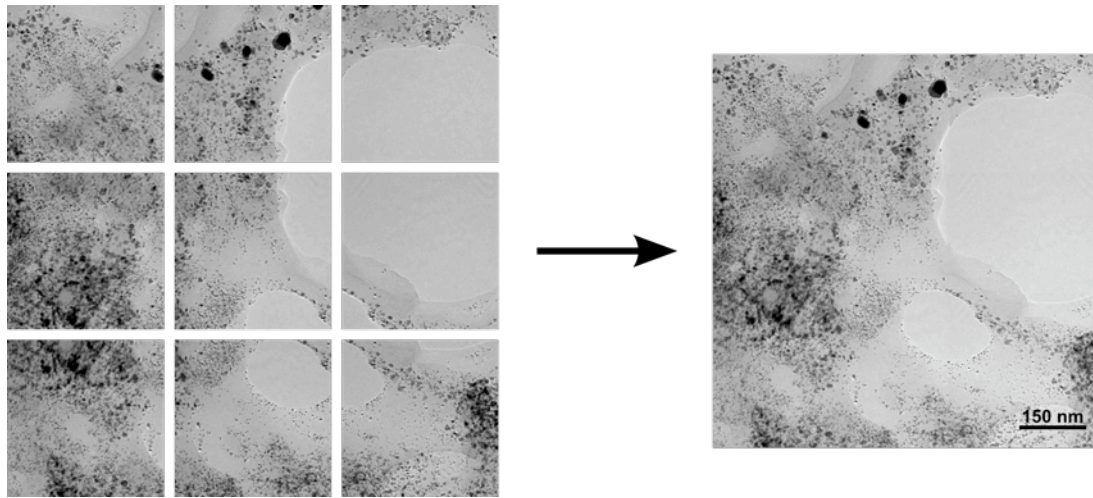


Figure 4.8. 3×3 image array of a PEFC electrode acquired by the image shifting routine. Individual images (left) and reconstructed image after automated alignment (right).

To obtain an aligned image of the element distribution, the alignment information from the reconstruction of the unfiltered image was used instead of direct cross-correlation of the element distribution images themselves. This generally results in a more accurate alignment and assures that there is no mismatch between single sub-images when superimposing the element distribution image over the unfiltered image.

4.8. CONCLUSION

It has been demonstrated that the combination of beam and image shifts is a viable possibility to extend the field of view for sample characterization while at the same time maintaining beam intensities high enough to record energy filtered images.

Furthermore, significant improvements concerning acquisition speed and drift correction were made when compared to the build-in Gatan routines, which are part of the Digital Micrograph suite. The individual optimizations especially improve the characterization of beam sensitive materials as PFSI polymers by energy filtered imaging.

Part 4

Characterization of Standard MEA Structures

5. CATALYST - POLYMER ELECTROLYTE INTERACTIONS IN THE LIQUID

For polymer electrolyte fuel cells a uniform distribution of the polymer electrolyte is generally intended to provide a good ionic contact to the catalytic sites and, thus, attain a high catalyst utilization and low voltage losses. Therefore, most current MEA preparation processes blend the catalyst and the polymer electrolyte in the liquid phase. Hence, liquid phase interactions of the polymer electrolyte with the catalyst and catalyst support particles play a significant role for the formation of the electrode structure.

Although a number of publications have addressed the effect of various electrode and ink preparation parameters on the performance and electrode structure of PEFCs [166,169,150,76], the interaction processes in the ink that lead to the formation of different electrode structures have only been scarcely investigated.

Gode et al. report an influence of the polymer electrolyte content on the catalyst agglomerate diameter, supporting a decrease of the agglomerate size with increasing polymer electrolyte content [48]. However, agglomerate sizes were not determined in the ink but from electrode fragments characterized by SEM. Therefore, the determined agglomerate sizes may not reflect the situation in the ink.

Work by Wang et al. showed a significant decrease of the aggregate size when the Nafion solution was diluted with aqueous NaOH [179]. But particle sizes reported for the ink deviate by more than one order of magnitude from values reported by other authors for dispersed carbon [197] or carbon supported catalyst inks [48] and do not match well with SEM images from the electrode layers presented in the same work.

In a recent publication, Malek et al. analyzed the interaction of Nafion ionomer chains with carbon particles by coarse-grained molecular dynamics simulation [103]. The authors report that for all three investigated solvent environments a phase segregation of the ionomer and agglomerated carbon particles was obtained. The work of Malek et al. is definitely a promising approach to gain information on inter-molecular and inter-particle interactions of dispersed catalyst-

ionomer systems which are currently not accessible by other experimental methods. Nevertheless, coarse-grained molecular dynamics requires significant simplifications to be made to the molecular structure of the ionomer and the carbon particles in order to treat the problem numerically and the result of the simulation will highly depend on the interaction and input parameters. Therefore, it is important to complement the results obtained from simulation with experimental data.

To analyze the ionomer-catalyst interaction in the liquid a rather uncommon approach based on electron microscopy was chosen. Microscopy analysis of dispersed systems in the liquid phase is usually a domain of light microscopy, as the high vacuum necessary for electron microscopy generally impedes characterization of liquid samples. However, many systems that exist in the liquid phase like colloidal solutions of polymers, proteins, viruses or other biologic material have dimensions much smaller than can be resolved by light microscopy. Due to the high importance of liquid systems, especially for biological samples, two different methods have been developed for the characterization of dispersed liquid systems in the transmission electron microscope. The first, cryomicroscopy, truly preserves the structure of the liquid state by freezing the sample in liquid nitrogen. It is therefore especially suited for aqueous systems that undergo conformational changes during evaporation of the solvent. However, sample preparation and handling is rather complicated and requires special equipment to assure a continuous cooling chain. Furthermore, the mass-thickness of the dispersed sample must be significantly different from the surrounding vitreous layer of water to obtain recordable image contrasts. The second, negative staining, uses a slightly different approach. For this method the dispersion is spread on a thin supporting foil. The particles in the dispersion are then surrounded by a heavy metal salt containing solution. Drying of the sample embeds the dispersed particles in a thin amorphous electron-dense layer of heavy metal salt. This method significantly increases the contrast for samples of low atomic mass due to the difference in scattering contrast of the sample and the surrounding heavy metal salt. Therefore, also particles of low scattering contrast and lateral dimensions of only a few nm like single protein molecules can be characterized by this method.

Although it has been demonstrated by Harris et al. that negative staining can also be successfully applied to non-biological samples, transfer of this technique into materials science has been very limited [57,58].

The work presented in this chapter is an attempt to use microscopical methods including negative staining in order to obtain a deeper understanding of the polymer electrolyte morphology in solution and its interaction with the catalyst and catalyst support particles.

5.1. STATE OF THE POLYMER ELECTROLYTE IN SOLUTION

Nafion and other PFSI polymer electrolytes do not form true solutions. Even in highly polar solvents like lower aliphatic alcohols dispersions of Nafion, frequently available as Nafion solutions, the polymer is contained in a well dispersed but nevertheless aggregated form. Based on the analysis of SAXS and SANS spectra of dilute solutions, it has been suggested that these aggregates have a rodlike structure [2, 101] with diameters varying from 3-5 nm depending on the solvent [138]. The consistent picture for these colloids corresponds to elongated particles made of packed and aligned backbone chains with the pendant sulfonated groups located at the periphery [138, 158].

According to Jiang et al. these rod-like particles [73] cannot exist in an isolated stable form even at low Nafion concentrations due to the strong hydrophobic effect of Nafion backbone. They proposed a Nafion micro-gel model in which the Nafion rods are cross-linked through the interaction of dangling solvophobic backbone chains (Figure 5.1).

In less polar solvents larger aggregates of spherical or ellipsoidal shape are formed. Uchida et al., who did an extensive study of PFSI in a large number of different solvents, specify a range of the dielectric constant of the solvent from 3 to 10 for the colloidal state of PFSI in solution [166]. In even less polar solvents precipitation of the PFSI occurred. For fuel cell applications mainly Nafion dispersed in mixtures of alcohol and water are used. However, also the colloidal form of Nafion has attracted some interest for the preparation of PEFC elec-

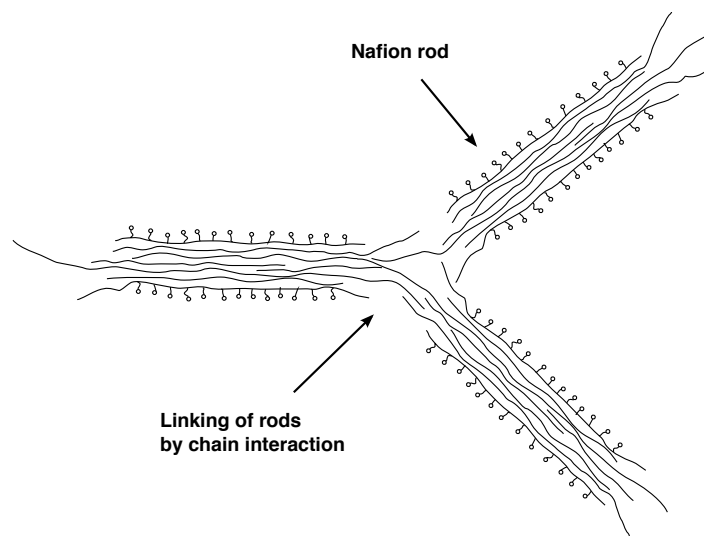


Figure 5.1. Proposed micro-gel model for Nafion in polar solvents according to ref. [73,158]

trodes [2,5,76,99,150,168]. Some authors even reported improved fuel cell performances for electrodes prepared from colloidal solutions when compared to those prepared with more polar solvents, in which Nafion exists in a more dispersed form [76,150,168].

Hence, due to their importance for the PEFC electrode fabrication processes the structure and interaction of the polymer electrolyte with the catalyst particles were examined for both the rod-like and the colloidal form of Nafion. Although it has been mentioned above that Nafion does not form true solutions, the terms Nafion 'solution' and 'colloidal' Nafion will be used further on to distinguish between the well dispersed rod-like form of Nafion and its more aggregated colloidal forms.

Figure 5.2 and 5.3 show TEM micrographs of Nafion aggregates deposited from a mixture of isopropanol and water (Nafion solution, Figure 5.2) and pentyl acetate (colloidal Nafion, Figure 5.3). The images were obtained by depositing a small drop of Nafion dispersed in the respective solvent on a TEM grid coated with a thin carbon film. The sample was then stained with a solution of 2 % uranyl-acetate in water to increase the scattering contrast between the Nafion

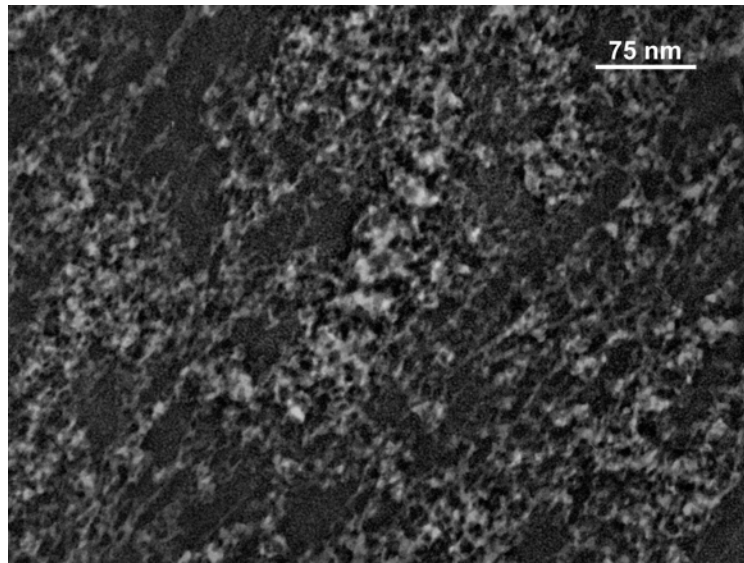


Figure 5.2. TEM image of Nafion deposited from a polar solvent (isopropyl alcohol) onto a carbon film showing a fibrillar structure. The sample was negatively stained with uranyl acetate.

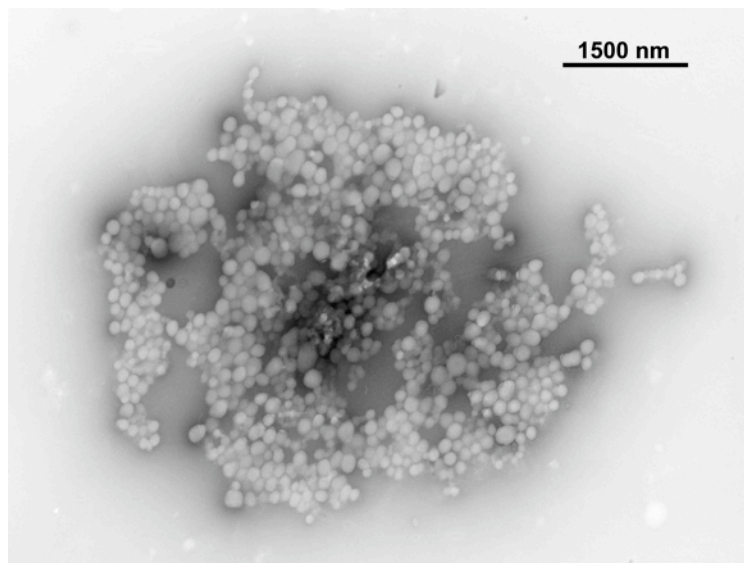


Figure 5.3. TEM image of Nafion deposited from a solvent of intermediate polarity (pentyl acetate) onto a carbon film. The sample was lightly stained with uranyl acetate.

particles and the carbon film.

The image of the sample deposited from an alcoholic solution shows a predominantly fibrillar structure that corresponds well with the micro-gel model of interconnected elongated flexible rods proposed by Jiang et al. [73]. The structure of the Nafion aggregates deposited from the colloidal solution is significantly different from that formed in the alcoholic solvent. The image shows Nafion beads of almost spherical symmetry. The size of the particles ranges from 50 to 300 nm with an average particle diameter of about 150 nm. The colloids themselves exist either as single particles or form aggregates of various sizes. The colloids in these aggregates mainly keep their spherical symmetry and no merging of colloids is observed. Hence, it can be concluded that the colloidal structure of the particles in solution is rather stable and also survives the drying process necessary to obtain the TEM sample.

5.2. CATALYST - ELECTROLYTE INTERACTION IN SOLUTION

In order to study the effect of different aggregate structures of Nafion on the catalyst - polymer electrolyte interactions in the liquid, two inks, one with an alcoholic solvent (isopropanol in water, ratio 1:2) and another with pentyl acetate ($\epsilon = 4.75$), were prepared. The inks consisted of a carbon-supported platinum catalyst (E-TEK, Pt loading 20 wt.%), a 5 % Nafion solution (Sigma-Aldrich, dispersion in lower aliphatic alcohols and water) and the respective solvent. For both inks the catalyst was first mixed with the solvent and stirred for one day before adding the Nafion solution.

Differences between the two inks were already observed before addition of the polymer electrolyte. The dispersion of the catalyst in the alcoholic solvent was rather unstable and rapid sedimentation was observed even after stirring for one day. In contrast the catalyst dispersed in pentyl acetate showed a lower tendency towards agglomeration resulting in a slightly more stable dispersion. These results correspond well with experimental data reported from Xu et al. who studied the dependence of the mean agglomerate size and zeta-potential on the dielectric constant of carbon black in various solvents [197]. The authors report

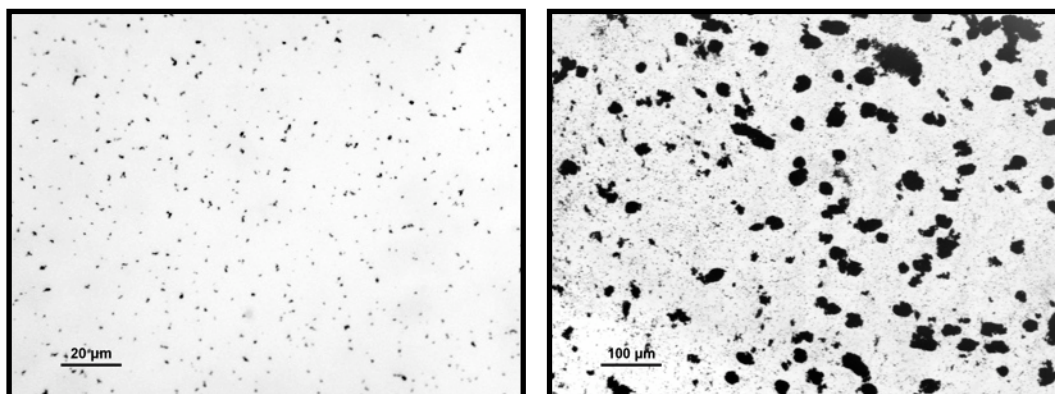


Figure 5.4. Light microscope images of catalyst inks dispersed in a mixture of isopropyl alcohol and water (left) and pentyl acetate (right).

that agglomeration was lowest for solvents of intermediate dielectric constant and strongly increased for solvents of high ($\epsilon > \sim 55$) and low ($\epsilon < \sim 3$) polarity.

Differences between the two inks continued also after addition of the polymer electrolyte solution. A drastic improvement of the dispersion in the alcoholic solvent was observed almost immediately after addition of the polymer electrolyte and a well dispersed ink of rather uniform aggregate sizes was obtained after two more days of stirring (see Figure 5.4 left). Addition of the polymer electrolyte to the dispersion in pentyl acetate had almost no observable effect. Light microscopy analysis of the ink before and after addition of the polymer electrolyte showed no significant differences of the catalyst dispersion. Aggregate sizes observed for the catalyst in pentyl acetate had a bimodal distribution with particles in the micrometer and sub-micrometer range as well as much larger aggregates with particle diameters in the range of 20 to 100 μm (Figure 5.4 right). The smaller aggregate sizes of the catalyst and ionomer in the polar solvent are also in qualitative agreement with dynamic light scattering experiments of Kim et al. [76].

The differences between the two inks upon addition of the polymer electrolyte may be explained by the interactive forces and the morphology of the polymer electrolyte in the different solvents. In solvents of high polarity the zeta potential of dispersed carbon black is low [197]. Therefore, electrostatic repulsion

forces are weak and particle agglomeration is mainly controlled by attractive forces between the particles. These attractive forces can be described by the so called Hamaker constant A . The Hamaker constant increases with the dielectric constant ϵ of the material. For dispersed media the Hamaker constant can be approximated as the squared difference of the roots of the Hamaker constant of the particle A_p and the Hamaker constant of the medium A_m :

$$A = (\sqrt{A_p} - \sqrt{A_m})^2 \quad (5.1)$$

Therefore, the larger the difference of the dielectric constants of the particle and the medium, the larger the attractive forces of the particles. Since the dielectric constant of carbon black is low ($\epsilon \sim 2.5-3$) [197], agglomeration of the catalyst will be strong in polar solvents.

Addition of the polymer electrolyte significantly improves the dispersion and this is most probably due to an adsorption of the polymer electrolyte on the surface of the catalyst agglomerates. The low polarity and surface charge of the carbon and the high hydrophobicity of the polymer backbone should favor an alignment of the polymer chains, so that the charged polymer side chains point into the solvent. Therefore, adsorption of the polymer electrolyte increases the surface charge of the catalyst agglomerates, which, in turn, improves dispersion due to higher electrostatic repulsion forces between the particles.

In solvents where Nafion forms colloidal solutions the difference between the dielectric constant of the solvent and the carbon supported catalyst is low. Thus, the driving force for adsorption of the polymer electrolyte will be low, too. Furthermore, the polymer electrolyte is agglomerated in colloidal structures bearing only a low surface charge due to the low polarity of the solvent. Therefore, agglomeration is governed by the surface charge of the carbon particles and addition of the polymer electrolyte has no significant effect on the dispersion.

5.2.1. TEM CHARACTERIZATION OF CATALYST DISPERSIONS

To study the interaction of the electrolyte with the catalyst more closely, TEM analysis was conducted also on catalyst inks. Since the use of a staining salt may

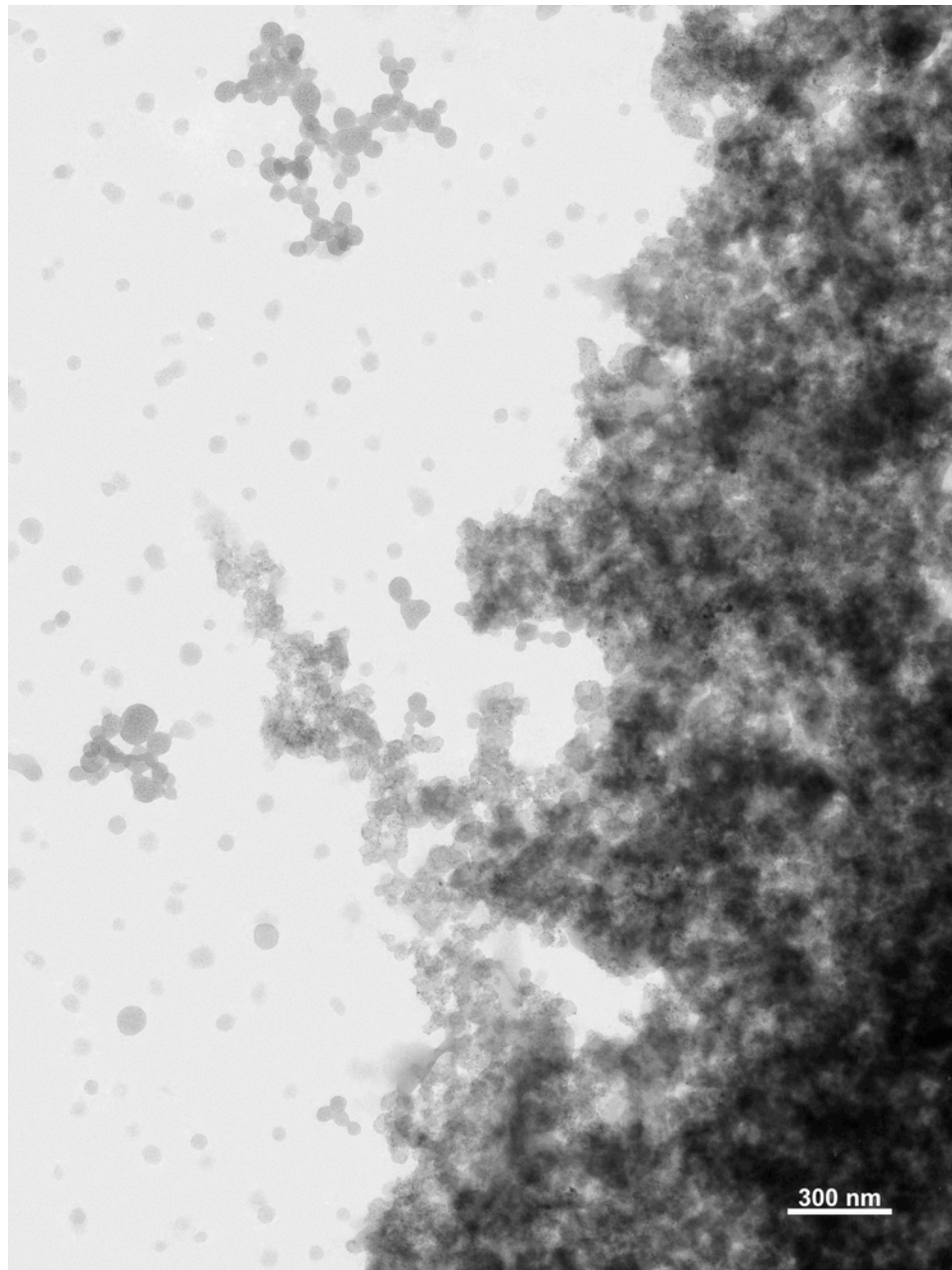


Figure 5.5. TEM micrograph of a colloidal catalyst ink. Single and aggregated Nafion colloids are visible in the left half of the image and a part of a large catalyst agglomerate on the right.

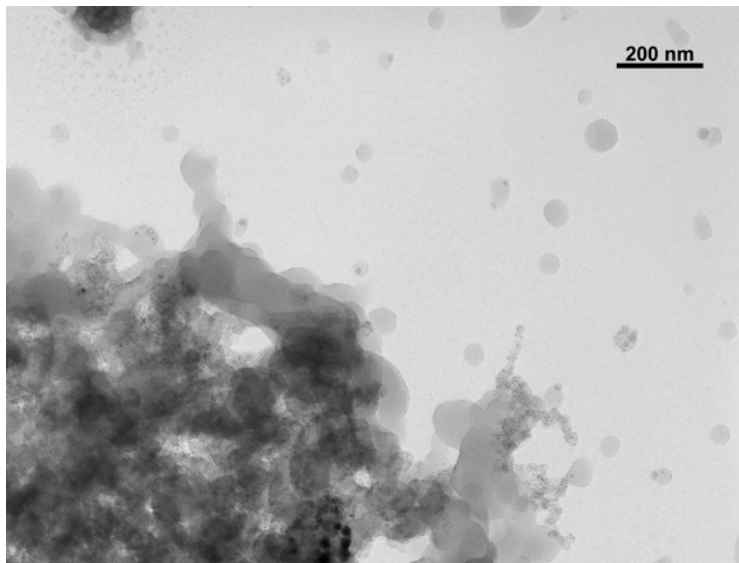


Figure 5.6. TEM image of Nafion colloids in contact with the catalyst surface.

influence the interaction of the polymer electrolyte with the catalyst, no staining was applied to catalyst inks for TEM characterization.

As for the pure Nafion dispersions a small drop of the catalyst ink was placed on a TEM copper grid coated with a continuous carbon film. Since the catalyst and electrolyte concentration increases considerably in the droplet during evaporation of the solvent, a highly diluted ink was used to avoid overlap of catalyst or polymer electrolyte particles on the dried sample. Figure 5.5 shows a TEM image obtained from a colloidal ink dispersed in pentyl acetate and deposited on a TEM grid coated with a continuous carbon film. On the right side of the image a large catalyst agglomerate can be seen. On the left Nafion colloids, which were formerly suspended in the ink, are deposited on the carbon film. While most of the colloids are not aggregated, some form fractal-like aggregates. In these aggregates the colloids largely preserve their spherical shape. However, Figure 5.6 shows, that, if the colloids get in contact with the catalyst surface, the colloidal structure is partially destroyed and the polymer electrolyte starts to wet the surface of the catalyst agglomerates. This indicates that also in low polar solvents

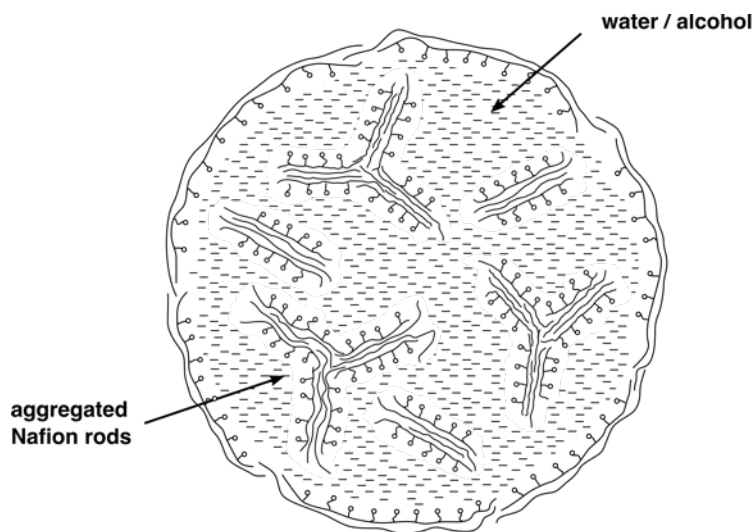


Figure 5.7. Model of the micellar structure of Nafion colloids in solvents of low polarity.

weak attractive forces exist between the catalyst and the polymer electrolyte. Furthermore, Figure 5.6 demonstrates, that the Nafion colloids, despite their high shape stability, are not rigid particles. Since the Nafion colloids are obtained by dropping Nafion 'solution' into a solvent of lower polarity, it is most likely, that they possess a micellar structure, which contains smaller rod-like colloids dispersed in an alcohol water solution. Therefore, a micellar structure of the Nafion colloids is proposed as depicted in Figure 5.7. The Nafion 'solution' enclosed in the micelles may account for their ability to wet the catalyst surface once the micellar structure is broken by the contact with the catalyst surface.

For the characterization of the ink dispersed in a polar solvent a different approach as for the colloidal ink was chosen. Since the fibrillar Nafion colloids in alcoholic solution would be hardly visible on a continuous carbon film without staining, the ink was cast on a TEM grid coated with a holey carbon film. Figure 5.8 shows a TEM image of the sample dispersed on the holey carbon film. Sev-

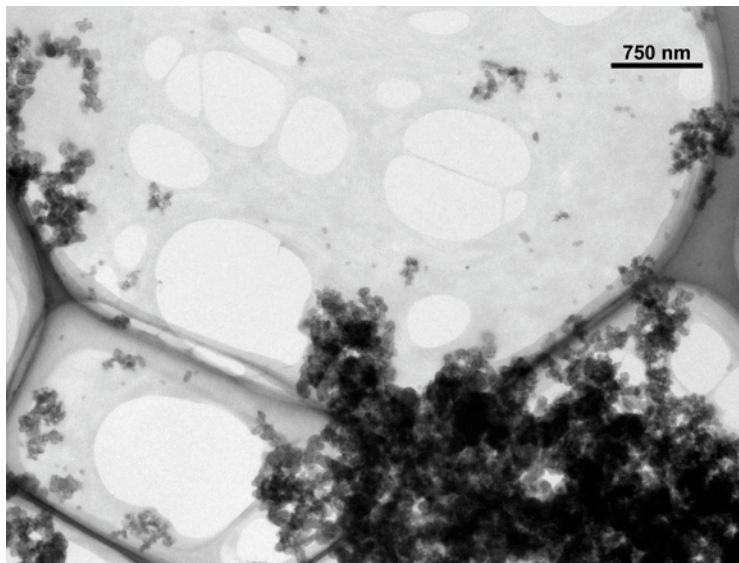


Figure 5.8. TEM image of a catalyst ink deposited on a holey carbon film from a mixture of isopropyl alcohol and water. In the image the holey carbon film can be seen as branches of mid to dark grey, while the Nafion film is seen in a lighter grey filling the holes of the carbon film.

eral catalyst agglomerate particles can be seen in the image. The catalyst particles are either surrounded by or embedded in a thin Nafion film, indicating a good contact between the polymer electrolyte phase and the catalyst. The Nafion film spans the holes of the supporting carbon film, visible as dark grey branches. In the Nafion film holes, some of them separated only by thin ligaments can be seen. Similar ligament-like Nafion structures have also been reported for PEFC electrodes containing Nafion [23] and may therefore be typical feature of recast Nafion. The exact origin for the ligament and hole formation in the Nafion film is unclear. Yet, it seems likely that tensile forces that grow in the shrinking polymer film when the solvent evaporates cause the film to break up and hence are mainly responsible for the hole and ligament formation. In addition inhomogeneous segregation of the polymer electrolyte due to non uniform solvent evaporation rates may also contribute to the hole formation process.

For the catalyst agglomerates a wide distribution of sizes was observed by TEM. At the lower end of the size range even single catalyst support particles embed-

ded in the polymer electrolyte film were detected. An upper end of the size distribution could not be determined by TEM, since further aggregation of agglomerate particles enclosed in a droplet can occur during the drying of the sample, which significantly alters the size distribution. The shape of the agglomerate particles also spans a wide range of different morphologies. Compact and dense particles as well as slightly fractal geometries were observed in the same sample.

5.3. CONCLUSION

Catalyst inks and pure Nafion dispersed in two different solvents were analyzed using light and transmission electron microscopy. A mixture of isopropanol and water was chosen as a model system for a well dispersed Nafion ,solution‘, while pentyl acetate was used to obtain Nafion in a colloidal form.

To visualize the colloidal structure of Nafion in the respective solvents by TEM negative staining with uranyl acetate was applied. A fibrillar or rod-like structure reported for Nafion ,solution‘ could be confirmed by the TEM measurements. In pentyl acetate spherical Nafion colloids, which most probably possess a micellar structure were observed. The interaction of the Nafion colloids among each other or with the catalyst was also studied by TEM. While in the colloidal form interaction among each other did largely preserve the spherical shape of the colloids, a partial collapse of the colloidal shape occurred when they interacted with the catalyst agglomerates. For the ,solution‘ state of Nafion a more complete wetting of the catalyst agglomerates was observed, indicating a stronger interaction of the polymer electrolyte with the catalyst in polar solvents.

6. PORE STRUCTURE & ELECTROLYTE DISTRIBUTION

The pore structure and electrolyte distribution in the electrode layer plays an important role for the transport processes and the electrocatalytic activity of a fuel cell.

For the characterization of the pore structure in PEFCs mercury intrusion porosimetry has been frequently used [76,23,154,168,194], but the application of gas adsorption [48,66,165] and thermal adsorption and desorption of higher boiling point solvents [36] has also been reported. These studies have shown that the range of pore sizes present in an MEA covers several orders of magnitude. The largest pores are found in the backing and gas diffusion layer, but also the catalyst layer can contain imperfections such as cracks and holes, with characteristic sizes of 5-200 μm [165]. However, the main part of pores in the catalyst layer is due to pores smaller than about 1 μm [168,165]. As outlined in section 2.2.3, the pores in this range can be classified into pores inside the catalyst agglomerate particles, i.e. pores between the individual agglomerated carbon support particles, and pores between the larger agglomerates. The lower end of the pore range is due to pores in the primary particles of the carbon black support with pore sizes below 3-5 nm. These pores are generally not considered for reactant transport, since they do not form an interconnected pore network. However, catalyst particles deposited in these pores may be lost for the electrochemical reaction, since they are difficult to access by the reactants or the polymer electrolyte [167,93].

Due to its importance for the transport of reactants and water, the pore structure has attained much interest. Various influences on the pore structure have been investigated including the MEA preparation technique [23,150, 165,194], the type of solvent to disperse the ink [76,99], different polymer electrolyte [23,48,168,194] and PTFE concentrations [114,149], the kind of carbon support [167,169] and the addition of pore formers [38,165].

The most comprehensive study on the influence of various carbon supports was presented by Uchida et al. [169,167]. By using different types of carbon blacks the authors were able to prepare MEAs with distinct pore distributions using the

colloidal method. Analysis of the pore volume based on the classification in primary and secondary pores exposed an almost linear trend of the cell current at 850 mV on the secondary pore volume. However, for carbon supports yielding very high secondary pore volumes, the polymer electrolyte content needed to be increased for the MEAs to follow the linear trend. Therefore, Uchida et al. concluded that only the external agglomerate surface, which is exposed to the secondary pores, is electrochemically active in PEFCs prepared by the colloidal method.

For the polymer electrolyte concentration it is generally observed, that the pore size and volume decreases with increasing polymer electrolyte concentration [168,48,23,121]. While this has been interpreted by some authors as a simple pore filling process [168,121], Gode et al. reported that an increase of polymer electrolyte goes along with a decrease of the electrode thickness [48], suggesting also a more compact arrangement of catalyst agglomerates in the electrode layer.

The solvents used to disperse the catalyst and the polymer electrolyte are generally classified by the type of aggregate structure the polymer electrolyte forms in the respective solvent. For polar solvents usually rod-like and well dispersed Nafion aggregates are obtained (see also chapter 5), while for less polar solvents with a dielectric constant smaller 10 colloidal Nafion particles have been reported [166]. For electrodes prepared from colloidal polymer electrolyte solutions it is generally considered that the polymer electrolyte does not block the primary pores inside the catalyst agglomerates, i.e. does not penetrate into the catalyst agglomerates [168, 150], while for polar solvents most authors report a decrease of porosity also in the pore range attributed to the primary inter-agglomerate pores [48,150,66]. This may either be due to a blocking of these pores by the polymer electrolyte or a penetration of polymer electrolyte into the catalyst agglomerates. Whether penetration of the polymer electrolyte into the primary pores occurs, is still controversial. Gas adsorption as well as electrochemical measurements of Gode et al. suggest that at least at higher polymer electrolyte concentrations a complete penetration of polymer electrolyte into the catalyst agglomerates occurs [48]. However, in a recent publication Song et al. claim that under normal conditions infiltration of the agglomerates with polymer electrolyte does not occur, but that infiltration can be forced by an autoclave treatment of the catalyst ink [154].

Apart from the type of solvent also the preparation process (e.g. the choice of substrate for the electrode deposition) can influence the polymer electrolyte distribution. For the decal process, which uses a separate substrate on which the electrode is coated and later transferred to the membrane or GDL by hot-pressing [189], Xie et al. reported, that an approximately 0.7 μm thick Nafion layer builds on the substrate side, if PTFE is used as a substrate material [193]. In contrast, no Nafion segregation at the substrate interface was observed when the electrodes were prepared on a less hydrophobic Kapton substrate.

While the pore structure of PEFCs can be characterized by mercury intrusion porosimetry or gas adsorption, there are currently no characterization methods by which the polymer electrolyte distribution or the catalyst agglomerate network can be analyzed directly. Some researchers tried to derive information on the polymer electrolyte distribution in the electrode by comparative studies of electrode porosities and pore size distributions [168,150]. However, changes of the pore size distribution can only be correlated with the polymer electrolyte distribution, if the structure of the catalyst network is unaffected by the change of the electrode processing parameters. Since this is frequently not the case, as has been shown in the previous chapter for the variation of the ink solvent, the validity of conclusions about the polymer electrolyte distribution derived from the interpretation of pore size distribution data may be questioned.

In this chapter a different approach for the characterization of the electrode structure based on analysis of MEA thin-sections by TEM and SEM is presented and the extraction of structural data from electrode images obtained by TEM or SEM is demonstrated for an electrode prepared of a standard carbon black supported platinum catalyst.

However, interpretation of SEM and TEM images obtained from electrode thin-sections is not straight forward and requires some pre-knowledge about the section morphology. Therefore, first some initial considerations on the morphology of electrode sections obtained by ultra-microtomy and consequences that result thereof for the interpretation of the SEM and TEM image data, will be discussed. Thereafter, the structure of a standard electrode made of a 40 wt. % platinum, carbon black supported catalyst (E-TEK) and a Nafion content of 28 wt. % is examined in more detail by SEM and TEM. Finally, the influence of

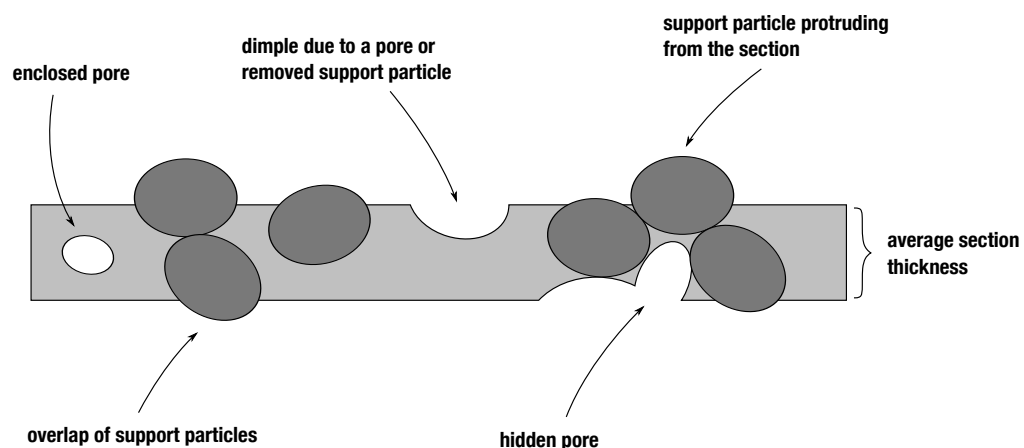


Figure 6.1. Schematic representation of specimen morphologies that can be obtained for thin-sectioned MEA samples.

different polymer electrolyte volume fractions and the ink solvent on the electrode structure, including the polymer electrolyte distribution, will be studied.

6.1. SECTION MORPHOLOGY

When interpreting TEM images it is essential to bear in mind that these images are 2D projections of 3D specimens viewed in transmission. For very thin specimens with features significantly larger than the specimen thickness, the 3D nature of the sample may be neglected. However, for thicker specimens and specimens with sample features close to the specimen thickness or even smaller, the 3D nature of the specimen must be taken into account and can significantly complicate their interpretation.

Ultra-microtomed sections of fuel cell electrodes are about 50-100 nm thick. This is a rather large thickness when compared to the smallest structural features of the electrode layer such as the catalyst particles or micro- and mesopores inside the catalyst agglomerates. But also the support particles themselves and large parts of the inter agglomerate pores have sizes smaller than or similar

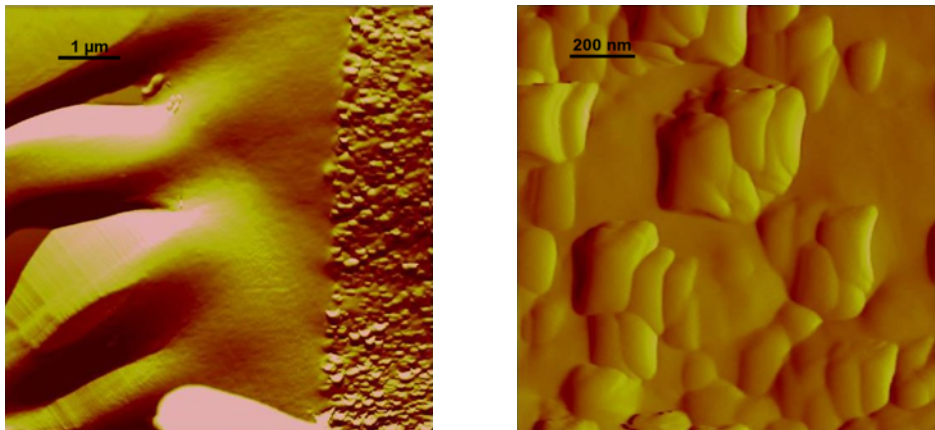


Figure 6.2. *AFM images of an electrode cross-section deposited on a silicon wafer. The left image shows the interface region of the membrane (left) and the electrode layer (right). The image on the right displays a part of the electrode layer at a higher magnification. [Contribution of these AFM images by Rongrong Chen, (Department of Mechanical Engineering, Indiana University-Purdue University Indianapolis) is kindly acknowledged].*

to the specimen thickness. Hence, a significant overlap of different electrode features exists along the z -axis of the specimen.

For a standard electrode made of a carbon black supported catalyst the ultra-thin section of the electrode layer consists of carbon particles embedded in a polymer matrix, pores and catalyst particles decorated on the carbon support. The polymer matrix may be composed either of the polymer electrolyte phase itself or the embedding resin. The carbon support particles typically have sizes ranging from 10 - 40 nm, depending on the type of carbon black used as catalyst support. Since the hardness of the carbon particles is significantly higher than the surrounding polymer matrix, it is highly unlikely, that the cut surface will run through a carbon particle. The particle will be rather torn out or pressed into the polymer matrix. Similar considerations must be applied to the sectioning of agglomerate particles. The hardness of the primary carbon particles and the high porosity inside the agglomerates create preferential fracture paths along the particle boundaries and inter particle pores. The sectioning of an agglomerate particle will therefore lead to a cleavage along structural flaws, which will also result in local thickness variations, i.e. higher surface roughness of the specimen. The

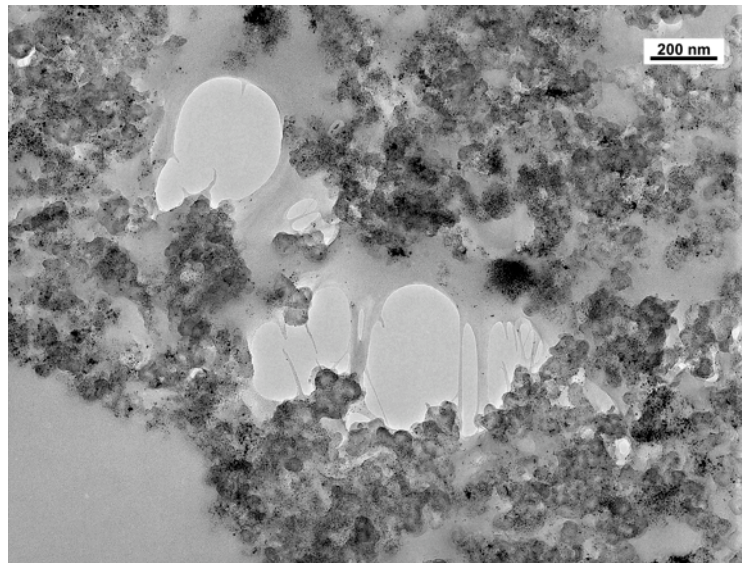


Figure 6.3. TEM micrograph of an electrode layer stained with phospho-tungstic acid. A part of the membrane is visible in the lower left corner of the image.

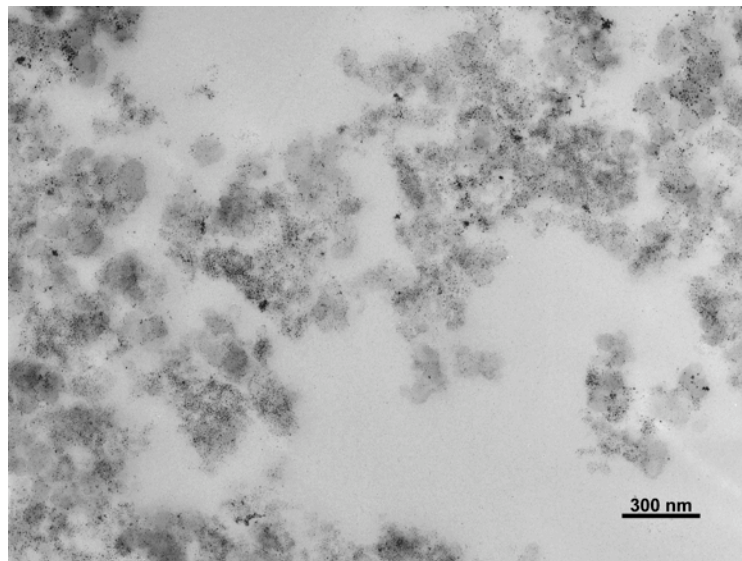


Figure 6.4. TEM micrograph of an ultra-thin section through a fuel cell electrode. Neither pores nor polymer electrolyte can be distinguished due to infiltration of the electrode by the embedding resin.

morphology of the specimen may therefore be represented schematically as shown in Figure 6.1.

The presence of local thickness variations described above could be confirmed by AFM measurements of an MEA section deposited on a piece of silicon wafer. Figure 6.2 shows an image of the interface region between the electrode layer and the membrane (left) and a magnified part of the electrode layer (right). In the image of the interface region the electrode layer is located on the right and the membrane is visible in the left and center. The electrode layer is easily visible due to its higher roughness. The features of the membrane seen in the very left part of the image are due to holes induced by the sectioning process, which lead to a bending and folding, when the membrane dries and shrinks after the sectioning. The holes in the membrane are most probably caused by the compression and swelling of the membrane when in contact with the wetted diamond blade.

In the TEM these thickness variations are not directly visible but manifest only as contrast variations of the catalyst agglomerates or polymer electrolyte film (Figure 6.3). The figure displays a TEM image taken of a PEFC electrode at the membrane-electrode interface. The electrode has been prepared from an alcoholic ink (isopropanol:water 1:2) containing a carbon black supported platinum catalyst (E-TEK, 20 wt.% Pt) and a Nafion fraction of 50 wt.%. The ink was exposed to a mild ultrasonic treatment for 20 min in an ultrasonic bath and then sprayed on a Nafion membrane heated to 100°C using an airbrush.

Due to the large Nafion fraction in the electrode layer, the polymer electrolyte is clearly visible as embedding phase, surrounding the catalyst particles. Lighter parts inside the catalyst agglomerate regions indicate that polymer electrolyte did not penetrate completely into the agglomerates. Apart from these small pores, two significantly larger, almost micrometer sized, pores are visible in the image.

In one of these pores, Nafion fibers, which have a strongly preferential orientation, can be seen. They originate from a larger Nafion part and span to the opposite side of the pore. The structure resembles that of glue, when detached from a surface before it has completely hardened. The pores and the Nafion fibers may

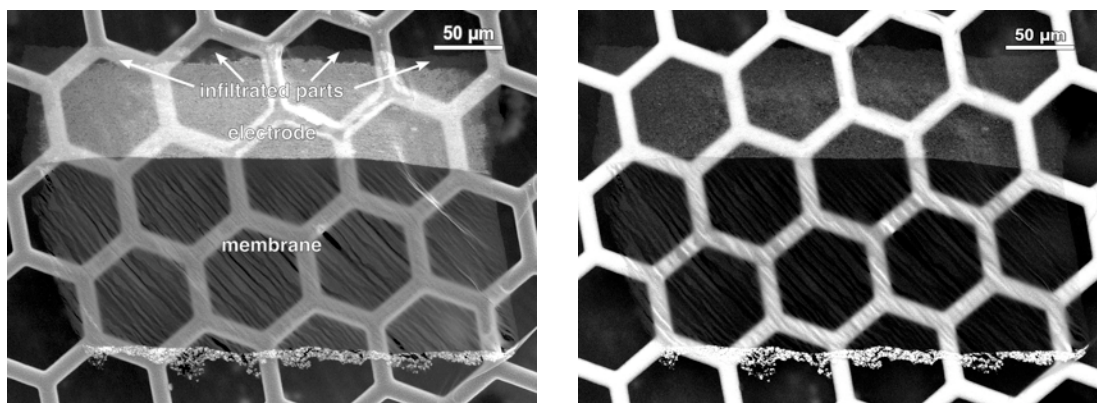


Figure 6.5. SE (left) and BSE (right) image of a thin-section through a MEA. In the SE image the darker outer parts of the upper electrode indicate regions where the embedding resin has penetrated into the electrode. (The bright hexagonal structure is due to the supporting copper grid.)

thus be due to an expansion of the electrode during the drying process. This expansion may be caused by evaporating solvent enclosed in the drying ink film.

Another problem, that complicates the interpretation of TEM images of the electrode layer, is caused by the embedding resin. It at least partially infiltrates the pores of the electrode layer. While this is a desired effect to stabilize the porous and therefore fragile structure of the electrode for the sectioning process, it is a major drawback for the interpretation of electrode images.

The polymer electrolyte and the embedding resin have very similar electron densities. As a consequence their scattering contrast in the microscope is almost identical. Therefore it is generally not possible to distinguish them in the microscope. This has significant implications for the structural analysis, since pores filled with resin cannot be distinguished from those filled with polymer electrolyte nor can the polymer electrolyte be identified directly.

An example of a completely infiltrated electrode part is given in Figure 6.4. Only the catalyst and catalyst support particles can be identified in the image. Pores or contrast variations that would aid identification of the polymer electrolyte and the embedding resin cannot be observed. Therefore, completely infiltrated samples provide only little structural information.

Infiltration of the electrode by the embedding resin is favored by large pores and thin electrode layers. For thick electrodes complete infiltration of the electrode can be prevented by increasing the viscosity of the embedding resin. This can be achieved by pre-polymerization of the resin before embedding the sample. In this case the embedding resin penetrates only partially into the electrode layer, as can be seen in Figure 6.5. In the SE image (left) the infiltrated part of the electrode layer is darker, letting the electrode appear thinner than in the BSE image (right). The lower intensity of the upper part of the electrode is due to a decreased surface roughness caused by the infiltration of pores by the embedding resin.

However, partial infiltration by pre-polymerization of the embedding resin can only be applied to electrode layers with well interconnected agglomerate particles, i.e. electrodes with modestly high or high polymer electrolyte content or other binders, since the stabilizing function of the embedding resin for the porous structure of the electrode layer is lost. A polymer electrolyte content of about 30 wt. % was found to be sufficiently stable to endure the sectioning process without further stabilization by the embedding resin, whereas electrodes with lower polymer electrolyte content showed significant signs of specimen damage.

6.2. ANALYSIS OF A STANDARD ELECTRODE

The MEA sample characterized in this section was obtained from the ZAE Bayern. It was prepared by an airbrush technique, spraying the catalyst inks on a heated Nafion membrane. The inks consisted of the catalyst, Nafion solution, water and isopropanol. On the cathode side a carbon supported platinum catalyst (E-TEK, Pt loading 40 wt. %) and 28 wt. % Nafion was used and a platinum-ruthenium black catalyst (Johnson Matthey, Pt:Ru 1:1) with 10 wt. % Nafion served as anode.

The characterization of the electrode structure in this part focuses on the cathode layer, since carbon black supported catalysts have mostly replaced unsupported catalysts and are predominantly applied in current state-of-the art electrode layers. For this type of catalysts the optimum polymer electrolyte concen-

tration is generally found close to about 30 wt. % [121], which corresponds well with the 28 wt. % of the characterized electrode layer.

6.2.1. SEM INVESTIGATION

Figure 6.6 (left) displays an SE image of a complete MEA thin-section. In the upper part of the image the electrode layer made of the carbon supported catalyst is visible. The anode layer made of unsupported platinum-ruthenium black displays as bright stripe in the lower part of the image.

To determine the total electrode porosity the electrode thickness was measured at different positions of the sample. A rather uniform electrode thickness of $107.7 \pm 1.6 \mu\text{m}$ was obtained for the cathode, indicating a homogeneous deposition of the electrode layer. The total electrode porosity was then calculated from the loading and the measured electrode thickness, using densities for Nafion of 2.08 g/cm^3 , carbon black 1.8 g/cm^3 and platinum 21.09 g/cm^3 . An electrode porosity of 75 % was obtained for the electrode investigated, indicating a highly porous structure. Although the value may appear rather high, it is in agreement with electrode porosities reported by other researchers [48,31,18,38].

Figure 6.6 (right), which displays a magnified part of the upper electrode layer, exposes that the distribution of pores, visible as black spots in the electrode layer, is not homogeneous. Fewer and smaller pores are contained in the right part of the electrode layer. Also in the left part the pore distribution is not completely homogeneous. Areas of about 3-5 μm with larger amounts of pores alternate with less porous parts of about the same size. This shows that inhomogeneities on rather large length scales exist in the electrode layer. While this inhomogeneity of the pore distribution is certainly due to the electrode preparation process, it demonstrates the difficulty to control the processing parameters of the preparation process to obtain homogeneous and reproducible electrode structures.

Large platinum agglomerates, visible as bright spots, can also be seen in the magnified image of the electrode (Figure 6.6 right). It cannot be ruled out that these agglomerates are partially due to electrochemical degradation of the catalyst, since electrochemical measurements had been carried out on the MEA prior

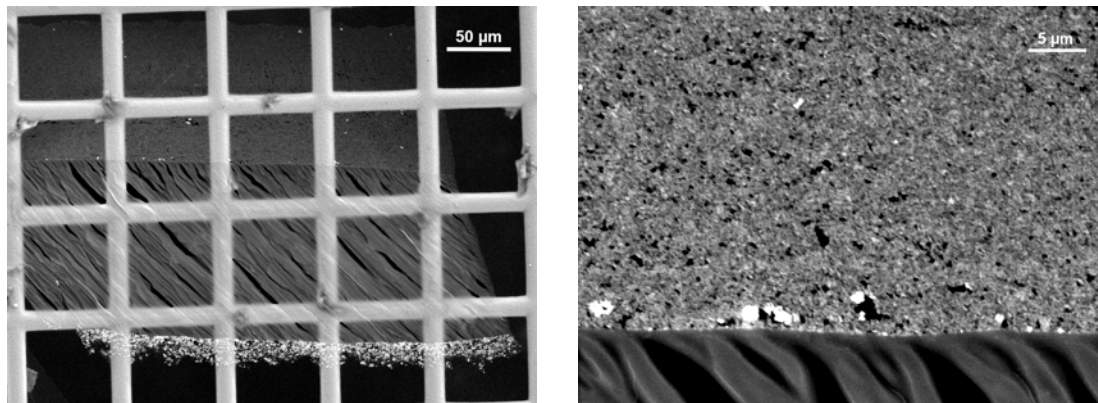


Figure 6.6. SEM images of an MEA showing inhomogeneous distribution of secondary pores and platinum agglomeration near the interface. Low magnification SE image of the complete MEA section (left). Upper electrode: platinum on carbon black, 40 vol. % Nafion. Lower electrode: PtRu black. Magnified part of the upper electrode layer (right).

to its structural analysis. However, electrochemical degradation of the catalyst is generally only observed for prolonged aging for several hundreds or even thousands of operating hours [20,81,195]. Therefore, catalyst degradation appears unlikely as a source for the observed platinum agglomeration. A more probable explanation of the observed platinum agglomerates is an inhomogeneous deposition of the catalyst particles on the support by the catalyst preparation method. This shows that even commercial fuel cell catalyst still have a significant potential to improve the platinum utilization by optimizing the catalyst distribution on the support.

SEM Image Analysis

A drawback of microscopy compared to other analytical techniques is that it is generally rather time consuming or not possible at all to obtain quantifiable information from images.

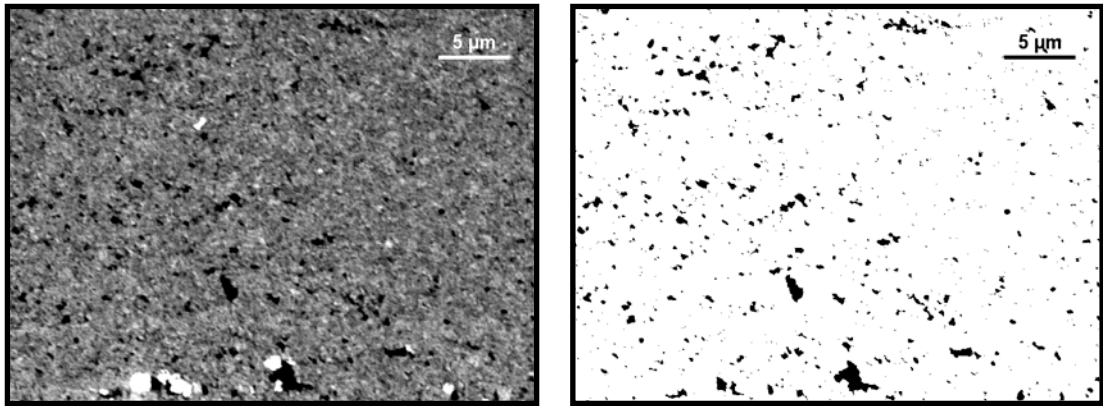


Figure 6.7. SEM image of an electrode made of Pt/C catalyst and 40 vol. % Nafion (left). Thresholded version of the image highlighting the pores in the structure (right).

However, the contrast between pores and other parts of the electrode is rather well defined in SE images, making the pores accessible for image analysis. A quantifiable image of the electrode (Figure 6.7 left) can be obtained by thresholding. If the threshold value is chosen correctly, a binary map of the pores in the image is obtained as shown in Figure 6.7 right.

The thresholded image can be processed to yield the relative pore volume by computing the ratio of pore pixels to the total number of pixels in the image. Image analysis software provides even more advanced analysis options. Particle detection algorithms [118,111] can be used to identify single pores. After particle detection, the pore area, perimeter, length, width and other geometrical information can be evaluated separately for each pore. Therefore, it is possible to generate pore size distribution curves, as shown in Figure 6.8.

The availability of geometric pore information, such as the pore aspect ratio or perimeter, is a clear benefit when compared to other pore characterization techniques, such as mercury porosimetry or gas adsorption.

However, also the image based approach has limitations. The pore size distribution shown in Figure 6.8 rapidly falls off for pores smaller than 200 nm. How-

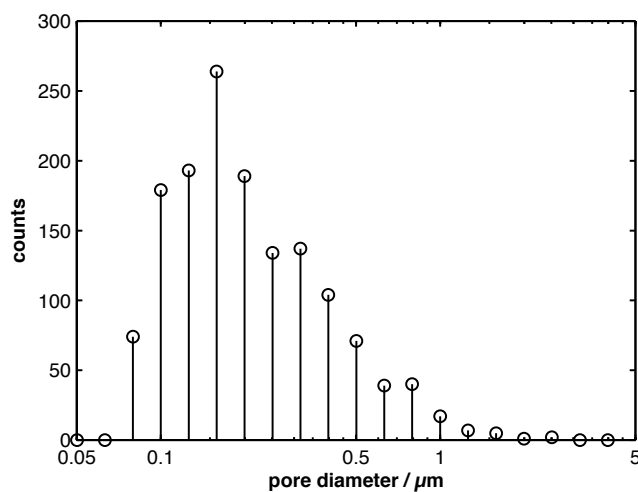


Figure 6.8. Pore size distribution obtained by analysis of the thresholded image data from Figure 6.7.

ever, the lower count rate for pores smaller than 200 nm does not reflect a true decrease of pores in the sample, but is a finite size effect of the specimen thickness as discussed in the introduction to this chapter. Only pores larger than the section thickness cause holes in the section, which provide sufficient contrast to be detected by the thresholding procedure. Also pores with diameters close to the section thickness will be under-evaluated as they may not be sectioned through the pore center.

The presence of a large number of pores smaller than 100 nm can also be rationalized by comparison of the total electrode porosity (75 %) with that determined by the thresholding (8 %). The huge discrepancy between the two porosity values shows that large inter agglomerate pores, which can be easily observed by SEM or TEM imaging of thin-sections, make only a minor contribution to the total electrode porosity.

Geometrical analysis of the pores showed a strong anisotropy of the pore shape. The roundness factor evaluated for pores of 200 nm was about 0.75 and reached a value of 0.63 for pores larger than 1 μm. The roundness factor of pores smaller than 200 nm could not be determined precisely, since the pore shape of these pores could no longer be clearly resolved.

6.2.2. TEM INVESTIGATION

Figure 6.9 shows a TEM micrograph of the PEFC electrode. The image was obtained by assembling 18 TEM images taken on photographic slides. To aid the visibility, the polymer electrolyte outside the catalyst agglomerates was colored in blue, based on the image intensity information.

The image shows a rather dense agglomerate network. Smaller voids between the catalyst agglomerates appear to be filled by the polymer electrolyte, whereas pores up to 1 μm exist in larger voids. The pores are not distributed equally in the image, but accumulate mainly in the upper left part of the image. This observation is consistent with the SEM analysis of the sample presented in section 6.2.1.

Quantification of the image area attributed to the polymer electrolyte yielded a relative image area of about 15 %. This value is significantly lower than the nominal polymer electrolyte volume calculated from the polymer electrolyte and catalyst loading and may therefore indicate that the polymer electrolyte infiltrates the catalyst agglomerates. However, translation of relative image areas into volume fractions is not possible for the polymer electrolyte, since it is not known how the remaining electrode porosity is distributed between the catalyst agglomerates and the polymer electrolyte.

However, closer examination of the TEM image shows that the electrode porosity is not only limited to pores inside and between the catalyst agglomerates. Figure 6.10 shows a single TEM micrograph of Figure 6.9, as obtained after digitalization of the photographic slide and slight contrast adjustments. The unprocessed image has rather smooth gradients of grey, which makes identification of particle boundaries or the exact location of catalyst agglomerates, the polymer electrolyte or even pores almost impossible. Application of color maps to grey level images can greatly improve the visibility of weak contrast changes. Figure 6.11 displays the same image as shown in Fig. 6.10, but with the grey-level intensities remapped to a color palette. The intensity ranges for remapping the grey level information to colors were chosen so that holes in the specimen were reproduced in white and the core of the agglomerate particles in black. The intermediate intensity range was distributed on colors from red to magenta following the scheme of a rainbow.

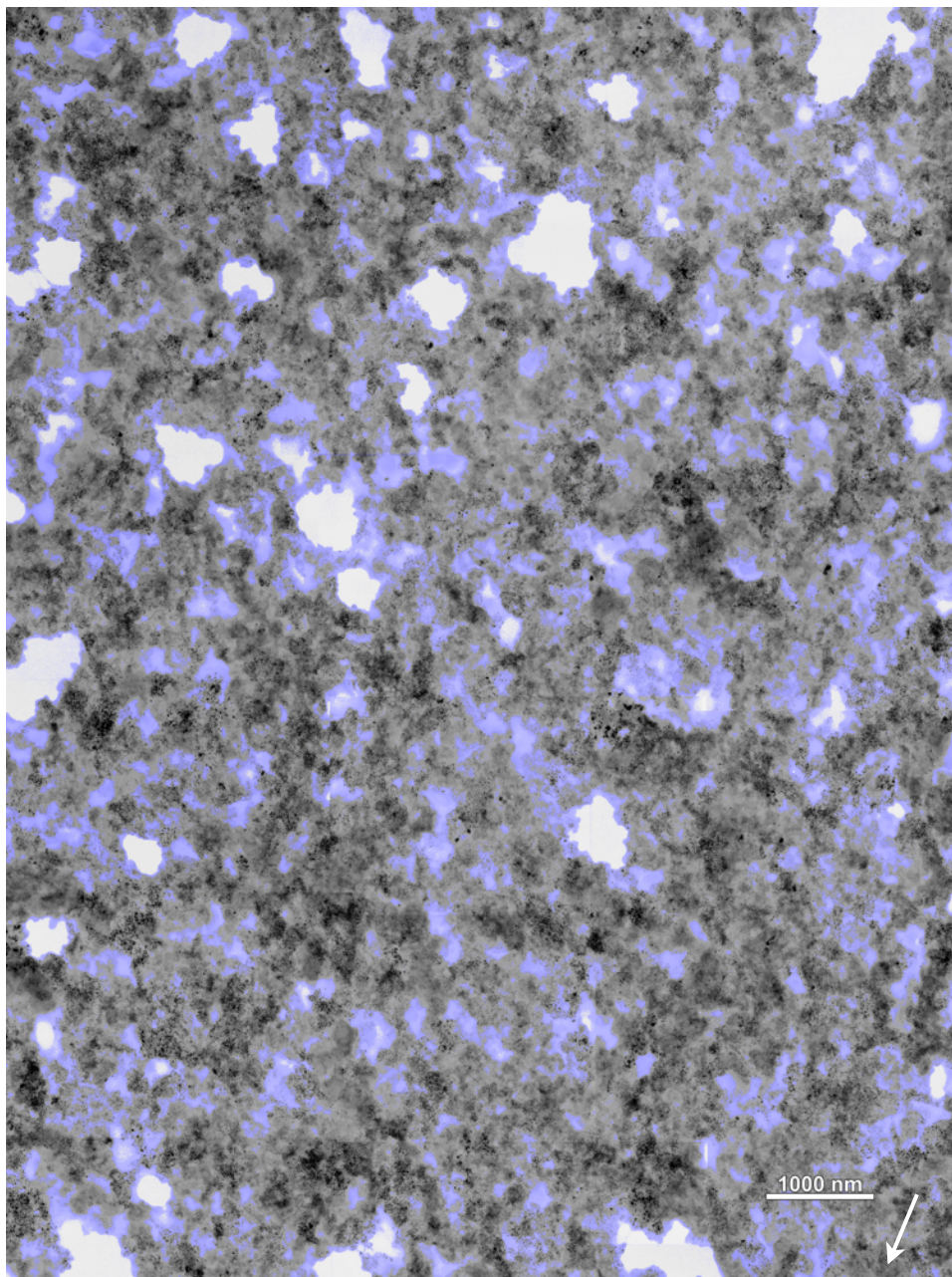


Figure 6.9. TEM micrograph of an ultra-thin section through a fuel cell electrode containing 40 vol. % Nafion. The image consists of 18 individual TEM micrographs, which have been assembled to span a larger sample area. Nafion in the pores of the electrode has been highlighted in blue based on the image intensity information to increase its visibility. The white arrow in the lower right corner indicates the direction towards the membrane.

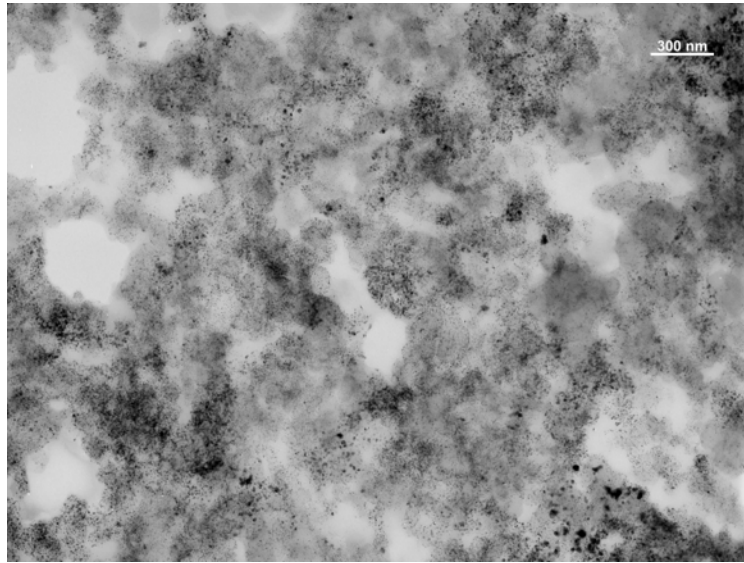


Figure 6.10. Original grey-level TEM image of a part of the electrode shown in Fig 6.9.

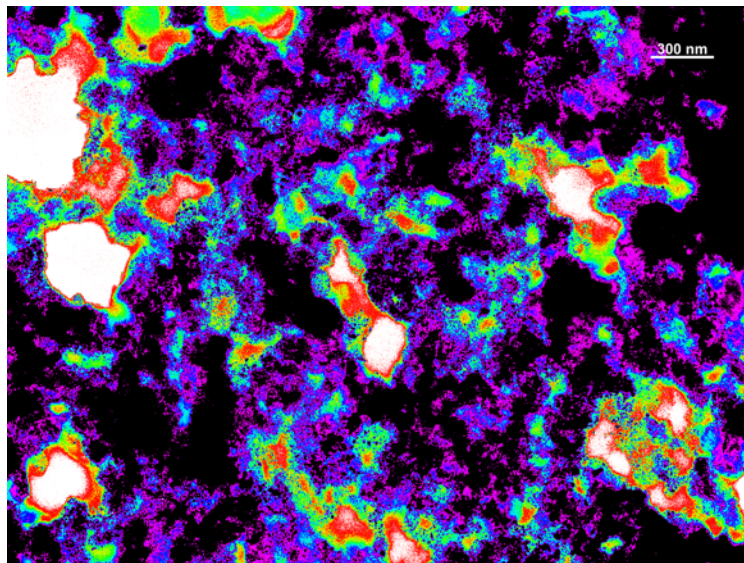


Figure 6.11. Same image as in Fig. 6.10 but with the grey-level information remapped to a color palette to improve the visibility of faint contrast changes.

Although a clear separation of agglomerates and the polymer electrolyte is not possible due to slightly overlapping contrast ranges, however, comparison with the original image shows that the colors red, yellow and green can be attributed to image parts which contain mainly polymer electrolyte, while image parts rendered in blue and magenta correspond to less electron dense parts of the catalyst agglomerates.

The assignment of different colors to the intensity range of the polymer electrolyte reveals that it is not uniformly filling or coating the pores in the electrode layer. The thickness variations in the polymer electrolyte may be due to pores in the electrolyte, however, the decreasing thickness of the polymer electrolyte found around pore walls rather suggests that the polymer electrolyte forms thin polymer films spanning across pores instead of coating layers on the catalyst.

Apart from aiding the structural analysis of the polymer electrolyte, the coloring also helps to identify individual agglomerate particles. Since the core of the catalyst agglomerates has a slightly higher density than the boundary region between two aggregated agglomerates, the magenta and blue coloring may be interpreted as agglomerate boundaries. The coloring reveals that catalyst agglomerates have rather different sizes and shapes. The observable agglomerate sizes range from large and electron dense particles of about 1 μm (upper right corner) to small ones with diameters even less than 100 nm.

6.2.3. STATISTICAL ANALYSIS BY AUTO-CORRELATION

Due to the high structural disorder of PEFC electrodes statistical methods must be used to obtain a more general description of the structure. Image auto-correlation is a statistical method to determine the self-similarity of a structure. It can be used to detect local ordering or anisotropies in images and has been applied in different fields like texture analysis [8], characterization of powder mixtures [112,11] and biology [190]. Mathematically auto-correlation is similar to cross-correlation, described in section 4.5. The only difference between the auto- and cross-correlation function of an image is that the auto-correlation function is calculated by correlating the image with itself instead of a different image, which serves as a mask. The auto-correlation function of an image is

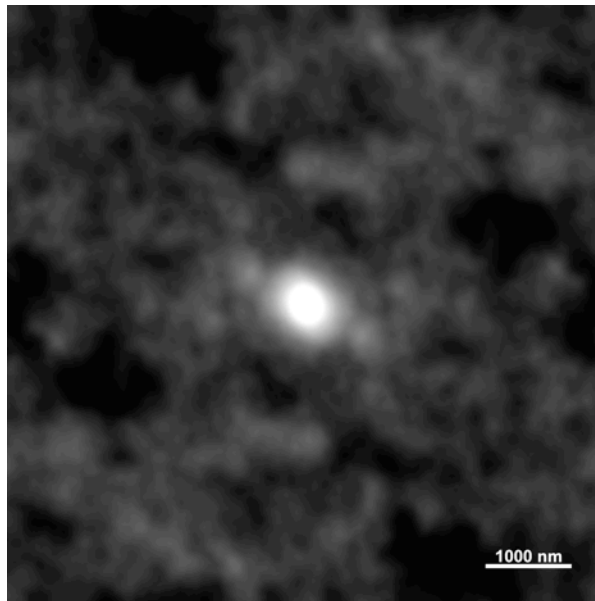


Figure 6.12. *Auto-correlation image of the electrode image displayed in Fig. 6.9. The auto-correlation reveals to preferential directions almost perpendicular to each other.*

centro-symmetric and describes its self-similarity in dependence of a shift vector in the image plane. The intensity of the auto-correlation function reflects the level of correlation between the original image and a displaced copy of it. A high value of the auto-correlation function therefore corresponds to good correlation between the shifted image and itself, while a low value reflects poor correlation.

Figure 6.12 displays the 2D auto-correlation function obtained from Figure 6.9. The auto-correlation image has an anisotropy with preferential directions almost perpendicular to each other. This indicates that the electrode structure shown in Figure 6.9, although random, is not perfectly isotropic. Since the directions of anisotropy are not parallel to the image axis, it can be excluded that the anisotropy is an artifact of the image assembly process. A possible source of the structural anisotropy may be the MEA preparation process. The hot spraying process, which was used for this MEA, builds the electrode in several layers. This layered growth may cause an anisotropy of the electrode in the x - y plane. The influence of the deposition technique on the structural anisotropy of the electrode be-

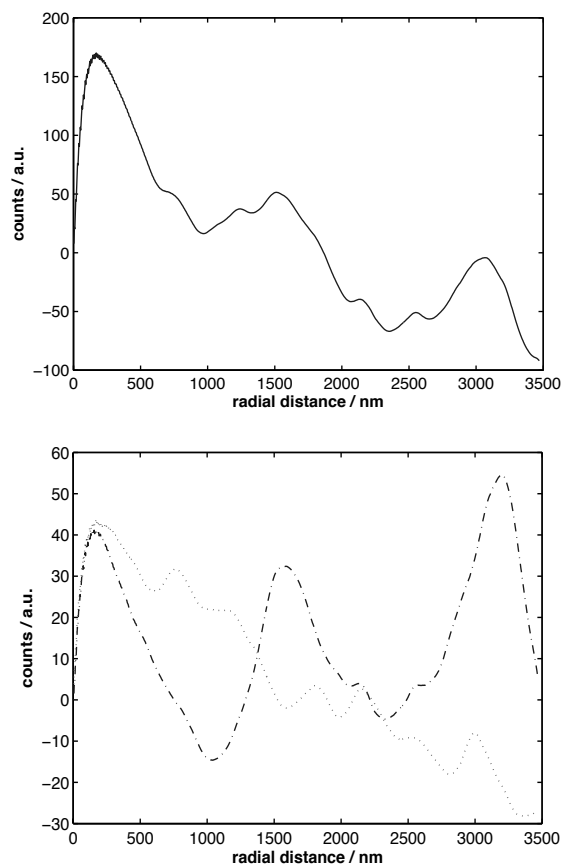


Figure 6.13. Radial correlation functions obtained by integration of the autocorrelation image shown in Figure 6.12. To amplify contributions at higher radial distances the radial correlation functions were weighed by r^1 . The top graph shows the radial distributions function for a complete 360° integration of Figure 6.12, while for the bottom graph only sectors of 45° corresponding to the prominent directions in Figure 6.12, were considered in the integration. The dashed-dotted line (---) is the integral intensity for the sector from 45° – 90° and the dotted line (···) for the sector from 135° – 180° .

comes even more evident for other types of catalyst supports like carbon nanotubes, as will be shown in chapter 11.

To verify whether the image auto-correlation function contains characteristic frequencies that correspond to characteristic distances in the electrode struc-

ture, the 2D auto-correlation function was integrated radially from the center. The resulting 1D auto-correlation function may be interpreted similar to a radial distribution function obtained from scattering experiments. Figure 6.13 shows 1D correlation functions obtained by radial integration of the 2D auto-correlation image. The 1D correlation functions were linearly weighed by r^l to amplify contributions at higher radial distances. Since the weighing function decreases faster towards zero than the correlation function increases towards infinity for small radial distances (< 200 nm), the weighed correlation functions contain an additional maximum at about 200 nm not present in the normalized correlation function. The graph at the top of Figure 6.13 displays the weighed 1D correlation function in dependence of the radial distance obtained by a complete 360° integration. Several maxima with similar distances can be observed in the 1D auto-correlation function, indicating the existence of characteristic distances in the image. Two main frequency components could be identified. A low frequency component with a peak-to-peak distance of about 1400-1600 nm corresponding to the main maxima of the curve and a second component of higher frequency but lower amplitude with a mean distance of about 400-500 nm. To verify whether these frequencies correspond to certain directions in the image, the 2D autocorrelation function was integrated separately for sectors of 45° . Figure 6.13 (bottom) shows the result of the partial integration for sectors from 45° - 90° and 135° - 180° , corresponding to the prominent directions of the auto-correlation function. It can be clearly seen that the low frequency component is most dominant in the sector from 45° - 90° (direction rotated about 25° clockwise out from the image normal), while the higher frequency component prevails in the perpendicular direction. Comparison with Fig. 6.9 shows that the low frequency component is most probably due to large pores, which have a preferential alignment especially in the upper left part of the image. The origin of the higher frequency component is more difficult to identify, but comparison with structural features of the electrode shows that it is most probably due to an average catalyst agglomerate or aggregate size.

To determine whether further frequency components, which are not directly visible in the graphs of Figure 6.13, are present in the auto-correlation function, the radially integrated auto-correlation functions were analyzed by Fourier transformation. The Fourier transform revealed further frequency components corre-

sponding to distances of about 600-650 nm and 800-900 nm. These distances most probably also belong to agglomerate or aggregate sizes. The almost uniform spacing of about 200 nm between the observed characteristic distances attributed to agglomerate or aggregate sizes, may reflect that catalyst domains in the electrode are aggregates of catalyst agglomerates having an average size of about 200 nm. This size also fits well with the average size of the larger agglomerate particles revealed in Figure 6.11 by color remapping.

6.3. INFLUENCE OF THE POLYMER ELECTROLYTE CONTENT AND SOLVENT

Optimization of the polymer electrolyte concentration and distribution in the electrode layer is crucial for the MEA performance. Low amounts of polymer electrolyte will result in poor catalyst usage and low proton conductivity causing high voltage losses over the whole current range, while an excess of polymer electrolyte will cause mass transport limitations lowering the MEA performance at higher current densities [168]. Since the polymer electrolyte concentration and the solvent have been reported to be key factors affecting the electrode structure, the influence of these two preparation parameters on the electrode structure will be examined in more detail in this section using the electron microscopy based analysis techniques described previously.

6.3.1. POLYMER ELECTROLYTE CONTENT

MEA Samples

Samples with varying polymer electrolyte content were obtained from the ZAE Bayern. All MEAs were produced by the same procedure and using the same catalyst materials as in the previous section. Only the amount of polymer electrolyte in the cathode layer was adjusted to have 40, 50 and 60 vol. % referred to the polymer electrolyte volume in the humidified state (Nafion density of 1.7 g/

Table 6.1. Nominal Nafion loadings and calculated volume fractions for the electrodes analyzed in this section as well as electrode porosities and thickness data determined by image analysis of SEM and TEM micrographs.

	MEA 40 vol. %	MEA 50 vol. %	MEA 60 vol. %
<i>Cathode catalyst loading (mg/cm²)</i>	2.0	2.0	2.0
<i>Nafion weight fraction</i>	0.28	0.37	0.47
<i>Nafion loading (mg/cm²)</i>	1.94	2.94	4.43
<i>Nafion volume fraction without pores (wet)</i>	0.40	0.50	0.60
<i>Nafion volume fraction without pores (dry)</i>	0.35	0.45	0.55
<i>Nafion volume fraction (TEM; with/without pores)</i>	0.15 / 0.16	0.26 / 0.30	0.29 / 0.31
<i>electrode thickness (μm)</i>	107.7 ± 1.6	93.6 ± 2.1	79.6 ± 1.6
<i>electrode porosity (calculated from the electrode thickness)</i>	0.75	0.66	0.51
<i>electrode porosity (SEM image analysis)</i>	0.08	0.12	0.10

cm³ instead of 2.08 g/cm³ in the dry). For a more detailed listing of the electrode compositions see Table 6.1.

In electrochemical measurements carried out at the ZAE Bayern, the highest cell performance was obtained for the MEA with 40 vol. % Nafion in the cathode layer. Both electrodes with higher Nafion loadings showed significant voltage losses at higher current densities indicating mass transport limitations due to the polymer electrolyte loading.

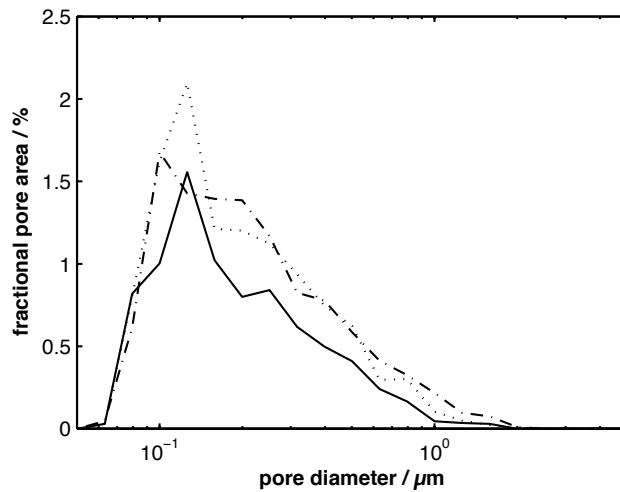


Figure 6.14. Pore size distribution curve expressed in terms of the fractional pore area determined by analysis of SEM images.

Sample characterization.

Electrode thicknesses were obtained from SEM micrographs of MEA thin-sections by measuring the electrode height at least at 20 different positions (Table 6.1). The rather low standard deviations of the electrode thickness indicate a rather homogeneous deposition of the electrode layers. With increasing polymer electrolyte fraction both the electrode thickness and the total porosity decrease. This is in agreement with the work of Gode et al. [48] and indicates, that the higher polymer electrolyte content in the electrode does not only cause a subsequent filling of pores but also influences the arrangement or size of catalyst agglomerates leading to a more compact electrode structure.

In order to determine the volume fraction of large inter-agglomerate pores the image based thresholding technique as described in section 6.2.1 was applied to SEM image data of the electrode layers. In contrast to the total electrode porosity (Table 6.1) the volume of the inter-agglomerate pores was found to increase slightly with the polymer electrolyte content. This means that the amount and pore volume of larger inter agglomerate pores is mainly unaffected or even

slightly increases with the polymer electrolyte content. The decrease of porosity must therefore be due to pores smaller than about 100 nm.

Pore size distribution analysis of SEM image data (Fig. 6.14) shows, that the increase of porosity for the 50 and 60 vol. % sample is mostly uniformly distributed over the whole pore range accessible by image analysis.

TEM micrographs (Figure 6.15 to 6.17), taken of the electrodes with different polymer electrolyte content, reveal significant structural changes of the electrode layer, when the polymer electrolyte content is increased from 40 to 60 vol. %. The image of the 40 vol. % sample shows a rather dense interconnecting network of catalyst agglomerates. The polymer electrolyte appears to fill some smaller pores in the electrode or coats the boundary of some larger pores. But the polymer electrolyte regions are not interconnecting in the image plane. This situation is almost inverted for the 50 and 60 vol. % samples. In these samples the polymer electrolyte found outside the agglomerates takes up a much larger

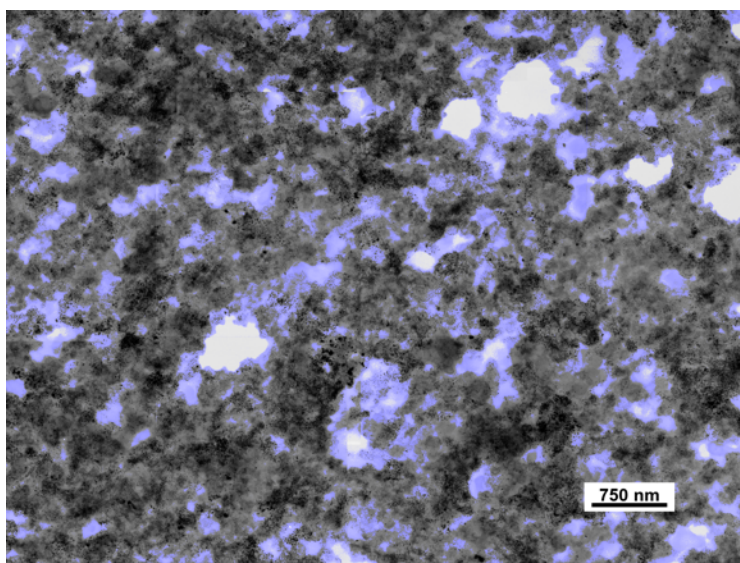


Figure 6.15. *Photomontage of several TEM images. Polymer electrolyte colored in blue.
MEA 40 vol. % Nafion.*

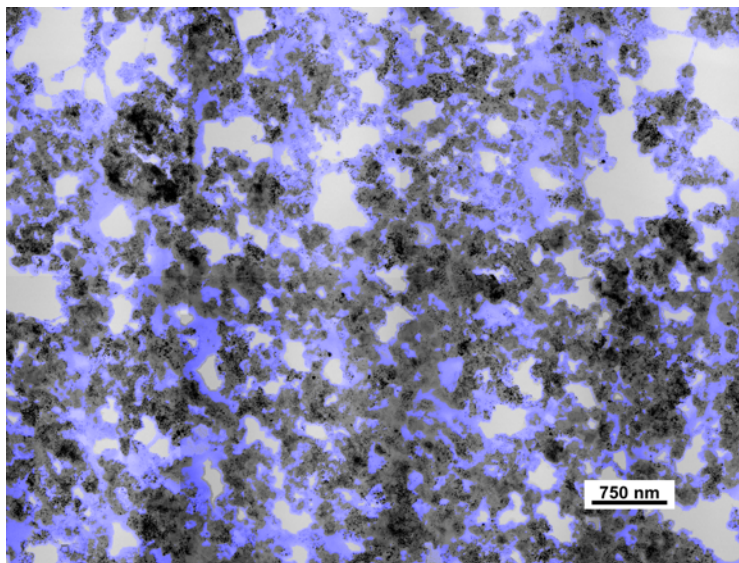


Figure 6.16. *Photomontage of several TEM images. Polymer electrolyte colored in blue.
MEA 50 vol. % Nafion.*

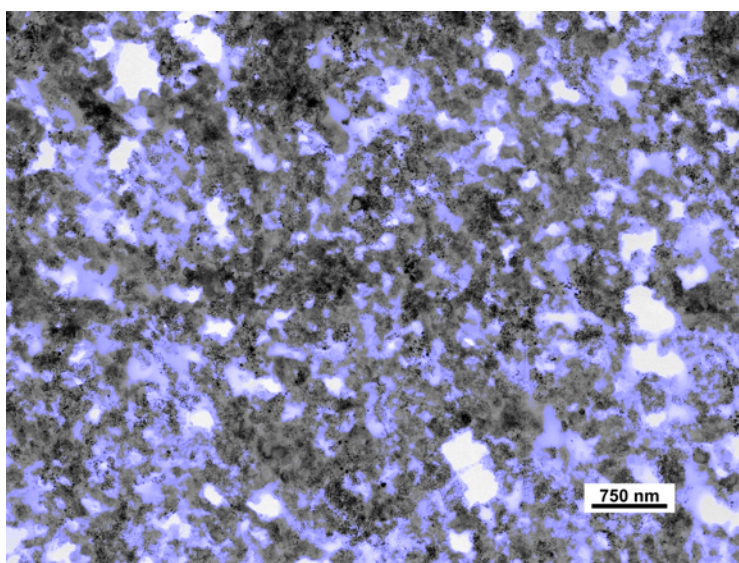


Figure 6.17. *Photomontage of several TEM images. Polymer electrolyte colored in blue.
MEA 60 vol. % Nafion.*

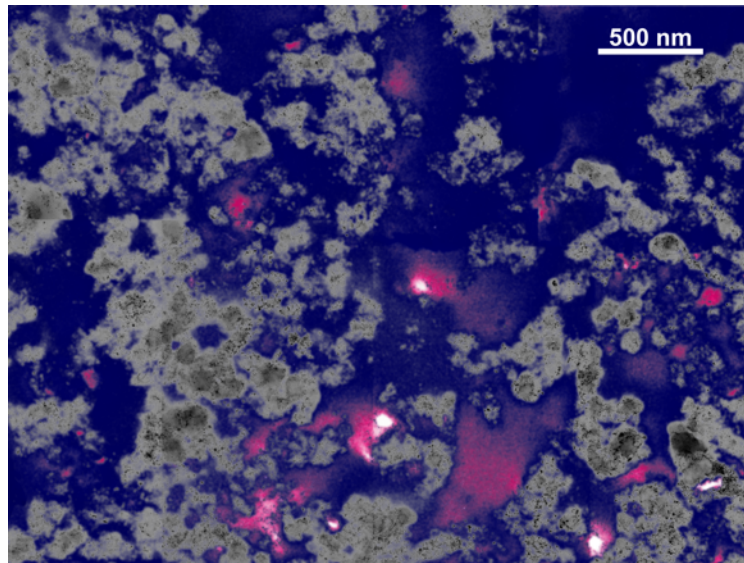


Figure 6.19. TEM micrograph of an electrode cast from a colloidal Nafion ink. The polymer electrolyte is colored in blue and magenta. Magenta parts correspond to areas of low scattering contrast. Pores are displayed in white.

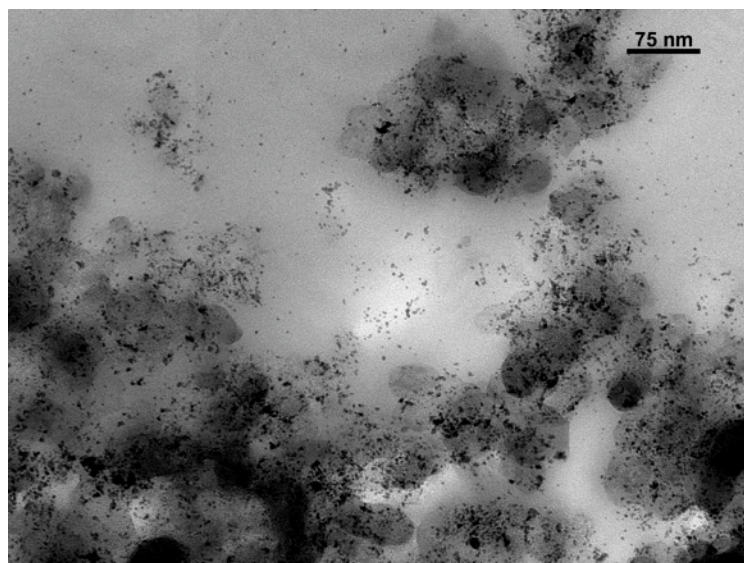


Figure 6.20. Zero-loss filtered TEM image of a fuel cell electrode prepared from a colloidal Nafion ink. The image was obtained by aligning 6 images zero-loss filtered CCD images.

volume and builds a mostly interconnecting network. Further, the size of the catalyst agglomerates is reduced when compared to the 40 vol. % sample and the network of catalyst particles appears less dense than in Figure 6.15. In Figure 6.16 and 6.17 an even larger number of very small agglomerates, consisting of only a few support particles, can be seen embedded in the polymer electrolyte matrix. This indicates that at least at higher polymer electrolyte concentrations parts of the catalyst may be isolated from electron conductive catalyst network by the polymer electrolyte.

By image analysis it was possible to quantify the image area attributed to the polymer electrolyte (Table 6.1). The data clearly reflects the increase of polymer electrolyte outside the catalyst agglomerates with increasing polymer electrolyte content. This may indicate that for polymer electrolyte loadings exceeding 30 wt. % the electrolyte is deposited mainly in the secondary pore space between the catalyst agglomerates, which would be consistent with the porosity data reported by Gode et al. [48]. However, conclusion from TEM image areas on volume fractions in the sample is difficult. This is also reflected by the almost identical values determined for the 50 and 60 vol. % samples. Quantification errors may result from variations of the specimen thickness, overlapping intensity ranges of the polymer electrolyte with the catalyst and pores, as well as the neglect of small pores, which cannot be resolved by TEM.

6.3.2. INFLUENCE OF THE SOLVENT

Figure 6.19 shows a TEM micrograph of an electrode cast from a colloidal ink containing a Pt/C catalyst (E-TEK, 20 wt. % Pt) and 30 wt. % Nafion. The polymer electrolyte phase is highlighted in blue and magenta. Pores in the structure are rendered white. Magenta parts indicate regions of lower scattering intensity in the polymer electrolyte film, i.e. indicate hidden pores. Even without quantification it is easily seen that the image area attributed to the polymer electrolyte is much larger than that of the sample shown in Fig. 6.9, although both samples were prepared with almost identical polymer electrolyte concentrations. The image area attributed to the polymer electrolyte even exceeds the value of the calculated catalyst to polymer electrolyte volume ratio (about 7:3) significantly. However, it should be noted, that the calculated volume ratio is based

only on the nominal densities of the catalyst and polymer electrolyte, not considering pores in the catalyst or polymer electrolyte. However, attributing pores only to the catalyst agglomerates would shift the catalyst to polymer electrolyte volume ratio even further towards the catalyst. Two reasons may be given to explain the huge discrepancy between the observed polymer electrolyte area in Fig. 6.19 and the calculated volume of the polymer phase:

- the embedding resin penetrated into the electrode structure and was erroneously mapped as polymer electrolyte
- the density of the polymer electrolyte in the electrode is significantly lowered when compared to the bulk density of Nafion, e.g. due to pores.

Unfortunately, due to the limited sample area accessible by energy filtering, it was not possible to obtain a map of the fluorine distribution to verify, if the image area assigned to polymer electrolyte in Figure 6.19, is indeed only occupied by the polymer electrolyte. However, identification of the polymer electrolyte was possible due to catalyst particles sheared off from their support during the preparation process of the ink. The catalyst particles were found in all parts of the polymer phase surrounding the catalyst agglomerates (Figure 6.20)

Therefore, confusion of the polymer electrolyte with the embedding resin as an explanation for the large polymer electrolyte volume observed in Figure 6.19 can be ruled out.

Hence, the large polymer electrolyte volume can only be explained by a significantly decreased polymer electrolyte density. Although Zook et al. reported slightly lower densities for recast Nafion when compared to its extruded form [205], the reported densities for recast Nafion cannot account for the large Nafion volume fraction alone. Therefore, a significant number of pores, smaller than the section thickness, must be present in the polymer electrolyte to explain the large polymer electrolyte volume.

Considering the observations made for the colloidal ink, the large volume of the polymer electrolyte may be explained by the shape stability of the Nafion colloids. It has been shown in the previous chapter, that the Nafion colloids do not collapse when they aggregate and the solvent evaporates. Therefore, pores will be enclosed by the aggregated colloids. These pores should be mostly smaller

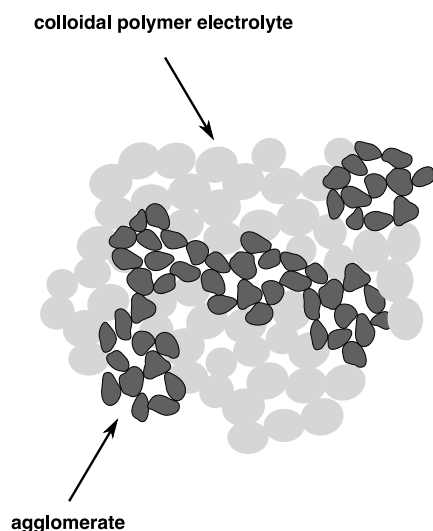


Figure 6.21. *Electrode model for an electrode prepared from a colloidal ink.*

than the section thickness due to the average size of the colloids of about 150 nm and can thus not be observed. Figure 6.21 shows a schematic drawing of an electrode prepared from a colloidal polymer electrolyte solution, as derived from the TEM observation of the electrode and ink.

Further, the large polymer electrolyte fraction found outside the catalyst agglomerates means, that penetration of polymer electrolyte into the agglomerates is extremely low if present at all. This view is in agreement with the original electrode model proposed by Uchida et al. [168]. A further support for the inability of the polymer electrolyte in its colloidal form to penetrate into the agglomerates is given by the studies of the catalyst ink presented in the previous chapter, where it was shown (Figure 5.7) that the colloidal Nafion particles wet the agglomerate surface, but show no signs of penetration into the agglomerates. However, in contrast to the work of Uchida et al., who considered only intra- and inter-agglomerate pores, the TEM analysis shows that pores in the polymer electrolyte must also be considered. It further shows that a clear separation into primary and secondary pores as defined by Watanabe et al. [183] is not possible, since the pores in the electrolyte have sizes rather similar to the primary pores in the agglomerates.

6.4. CONCLUSION

It has been shown that TEM and SEM imaging of thin and ultra-thin sections in combination with advanced image analysis techniques are powerful tools for the characterization of complex low ordered composite structures such as PEFC electrodes. Using statistical image analysis techniques it was also possible to extract quantitative or semi-quantitative information from the SEM and TEM image data which can be directly compared to the structural information provided by the images.

Studies on electrodes prepared with different polymer electrolyte concentrations clearly demonstrated that the influence of the polymer electrolyte does not only consist in a subsequent filling of pores, but also significantly affects the size and aggregate structure of the catalyst agglomerates. Further, an increase in pores larger than 100 nm was observed with increasing polymer electrolyte content, although the total porosity of the electrode decreased. This was attributed to retained evaporating solvent during the MEA fabrication process leading to an expansion of the electrode.

The structure of the electrode prepared from colloidal Nafion solution was found to differ significantly from electrodes prepared from non-colloidal solutions. The polymer electrolyte in the electrode prepared from colloidal Nafion solution was observed to take up a much larger volume fraction, indicating that i) the colloidal Nafion does not penetrate into the catalyst agglomerates, and that ii) the colloidal form of the Nafion particles causes a significant number of pores in the polymer electrolyte itself.

In addition, the structures formed by the polymer electrolyte cast from non-colloidal solutions differed strongly from a simple coating on catalyst agglomerates. However, in contrast to the colloidal solution, the observed structures resembled more those of thin films or fibrils. The simple pore model, differentiating only between primary and secondary pores, as introduced by Watanabe for PAFCs [183], therefore, cannot be justified for PEFCs, although it has been repetitively used by several authors in the field of PEFC research to interpret electrode porosity data [168,150,23,154,194].